Doctoral Dissertation

博士論文

Development of methods for estimating surface composition from observing surface-bounded exospheres

（表面境界外気圏の観測による
天体表面組成の推定手法の開発）

A Dissertation Submitted for the Degree of Doctor of Science
December 2022
令和 **4** 年 **12** 月博士（理学）申請

Department of Earth and Planetary Science,
Graduate School of Science, The University of Tokyo
東京大学大学院理学系研究科地球惑星科学専攻

Yudai Suzuki
鈴木　雄大

Abstract

Most part of atmospheres from just above the surfaces of Mercury and comets are primarily regarded as collisionless atmospheres, or exospheres. Exospheres connected to surfaces are called surface bounded exospheres (SBEs). SBEs are important in understanding the conditions required for celestial bodies to maintain atmospheres as regions where direct interaction between the space environments and the bodies themselves can be observed. SBEs are believed to directly reflect the surface environments; therefore, surface compositions and thermal histories of celestial bodies far from the Earth, whose surfaces are hard to be directly observed, can be assumed from observation of their expanded SBEs. Observation of the relationship between the surface composition and the distribution of SBEs has been largely limited to the use of the MESSENGER spacecraft in the case of Mercury and the Rosetta spacecraft in the case of Comet 67P/Churyumov-Gerasimenko, implying that further discussions using different particle species and observational data from other instruments are necessary to achieve a more general understanding.

In this study, I aim to establish methods for estimating nucleus surface composition from coma observations in the near-future exploration of comets, which have very extensive hydrogen comae. As a preliminary step, Mercury, whose surfaces and SBEs were well observed and where interaction with space environments derived from the Sun can be easily seen, is focused on in Chapter 2. I describe a correlation analysis of the exosphere and surface distributions of Mg, Ca, and Na atoms on Mercury using the observational data obtained via MESSENGER. It was found in the previous study that Mg was concentrated in the lava plain, with increasing abundance in the exosphere above that region. In this study, the distributions of Ca and Na were also analyzed by

applying physicochemical parameters. Consistent with previous studies, exosphere and surface Mg distributions were strongly correlated. A weak correlation was observed for Ca, presumably owing to the fact that the solar radiation acceleration of Ca is greater than that of Mg, and Ca ejected into the exosphere is soon swept away in the anti-sunward direction. Although there is no surface abundance data with high longitude resolution, the exospheric distribution shows that only high-temperature regions exhibit non-seasonal variation. This can be explained by the existence of two forms of Na binding to the surface, as has been assumed by conventional models. From these results, it appears that conditions for species that reflect exosphere-surface correlations on Mercury are, at minimum, low solar radiation acceleration and moderate volatility.

In Chapter 3, I evaluate the fraction of active areas on the surfaces of comets using coma observation data from the EUV spectrometer onboard the Hisaki satellite. Water production rate is an important indicator of a comet activity when inside a heliocentric distance of approximately 3 au, and most data have been provided by SOHO/SWAN observations. In this chapter, the sensitivity calibration of Hisaki was conducted by utilizing data usually treated as noise. Water production rates of four long-period comets were studied. The obtained values were found to be lower than those estimated from ultraviolet observations performed by the Solar Wind Anisotropies (SWAN) camera onboard the Solar and Heliospheric Observatory (SOHO), as well as infrared observations via the iSHELL spectrograph installed at the NASA Infrared Telescope Facility (IRTF). Constraints imposed by parameters such as velocities and photodissociation lifetimes of particles noted by observation and models were required. Furthermore, the fraction of active regions on the nucleus surfaces was estimated.

In Chapter 4, I discuss the radiative transfer process in cometary comae using

numerical simulation for the purpose of understanding the cause of the Ly-α radiance distribution identified by Hisaki. From the analysis in Chapter 3, it was found that the slope of the Ly-α radiance radial profile becomes flatter below the distance of approximately 5×10^4 km. This was attributed to variation in inclination of multiple scattering; therefore, a radiative transfer model was constructed. Using this, the Ly-α radiance profile obtained by Hisaki observations was well reproduced. Applying this model, conditions under which multiple scattering becomes effective in comae can be considered. The sunward/anti-sunward radiance asymmetry and the apparent increase of D/H ratio around the nuclei were found to be caused by the multiple scattering.

In Chapter 5, in order to obtain new observational data of a comet, I conduct a design and performance evaluation of the Hydrogen Imager (HI) onboard the Comet Interceptor (CI) spacecraft, which is still under development. CI is the first attempt to fly-by long-period comets or interplanetary objects. In this chapter, past observations of Ly-α radiance in the cometary comae were summarized to determine the required performance of HI, such as the field of view and the effective area. Subsequently, the optical system was optimized using an optical design software, and the field of view, spatial distribution, and tolerance were investigated. Finally, the performance of the band-pass filter, mirrors, and gas filters used for HI were experimentally evaluated, and effective area and wavelength resolution were calculated. From this, it is found that the design satisfies the required performance.

Finally, in Chapter 6, I examine the feasibility of measuring the D/H ratio of comets using HI. The expected Ly-α radiance observed via HI was calculated using the radiative transfer model constructed in Chapter 4. Simulated observational data were created using the effective area of HI and the absorption rate of gas filters estimated in

Chapter 5. Using these results, the feasibility of detecting deuterium and evaluating the D/H ratio by HI is discussed. It was found that deuterium could be detected with a sufficient S/N ratio unless the target comet was extremely faint and that the D/H ratio could be evaluated with relative error less than 50% by using the model from Chapter 4.

Table of Contents

1. Introduction

1.1. Surface Bounded Exosphere

In celestial bodies with thick atmospheres such as the Earth, interatomic collisions are not felt above the altitude of several hundred kilometers. Such regions are called exospheres. Contrarily, most part of atmospheres of Mercury and comets is considered collisionless atmospheres, or exospheres. These kinds of exospheres connected to the surfaces are called surface bounded exospheres (SBEs). Mercury is the only planet with an SBE, although most small bodies such as comets, asteroids, and moons also have SBEs. Exoplanets with SBEs have also been found (e.g., Kepler-37b: Barclay et al., 2013); thus, SBEs are ubiquitous in planetary systems and are important systems to understand general celestial environments.

Gaseous atoms and molecules that consist of SBEs are supplied by desorption or sublimation from the surfaces, and are lost in a short time either by escaping into the space or re-impacting on the surfaces (Fig. 1.1). Therefore, SBEs are important targets for understanding the conditions for general celestial bodies to maintain atmospheres as regions where direct interaction between the space environments and the celestial bodies can be observed. Besides, SBEs are expected to directly reflect the surface environments since their distributions reflect the production rate distributions from surfaces. This is especially useful in studying the surface compositions and thermal histories of celestial bodies far from the Earth, such as satellites of outer planets and exoplanets, assumed from observing their expanded SBEs.

In the following sections, the exospheres of celestial bodies with SBEs will be introduced, especially focusing on their connection to the surfaces.

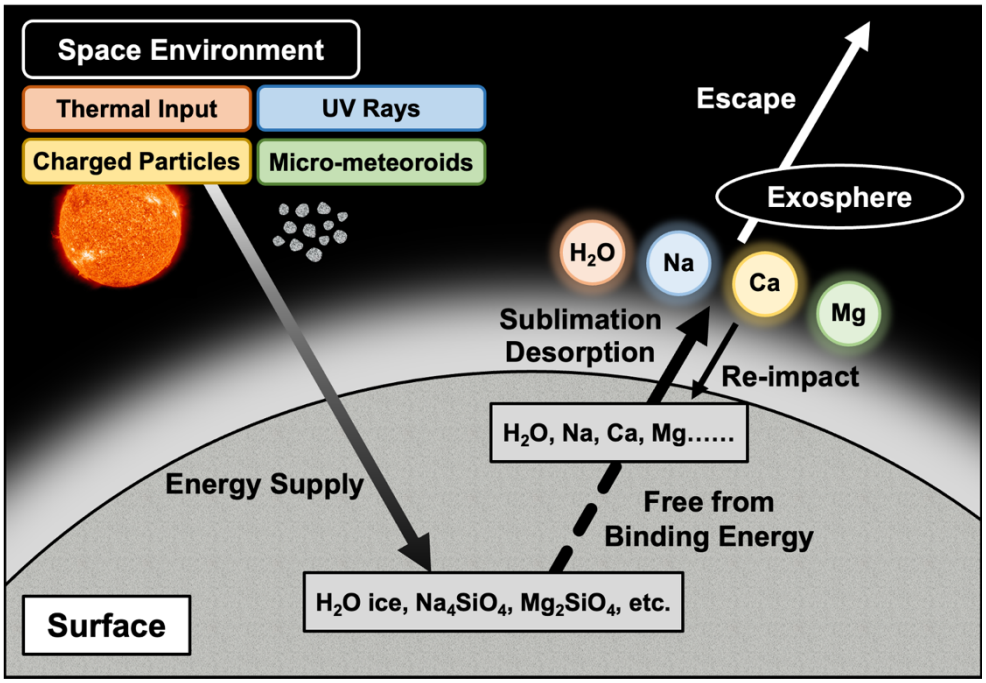

Fig. 1.1. Schematic representation of surface bounded exosphere system.

1.2. **Exosphere of Mercury**

1.2.1. Basic Information

Mercury is the closest to the Sun among the solar system bodies with SBEs, and is exposed to severe environments such as ultraviolet rays and the solar wind. Therefore, their interaction with planetary bodies can be vividly observed. Basic information on Mercury is shown in Table 1.1Table 1.1. Since Mercury has a large eccentricity and its aphelion distance is 1.5 times the perihelion distance, the exospheric distribution has large seasonal variability. As a parameter that expresses the seasons of Mercury, the orbital phase angle measured from the perihelion, i.e., the true anomaly angle (TAA) is used (Fig. 1.2).

According to the NASA factsheet (https://nssdc.gsfc.nasa.gov/planetary/factsheet/mercuryfact.html), the major exospheric component of Mercury is as shown in Table

1.2. Since the exosphere drastically fluctuates depending on the TAA and local time, the listed values are only for reference. H and He are supplied by the solar wind (Goldstein et al., 1981), and most of the other species are supplied to the exosphere through desorption from the surface (e.g., Hunten et al., 1988). The details of desorption mechanism and behavior in the exosphere are described in the following section.

Equatorial Radius	2.44×10^3 km
Mass	3.30×10^{23} kg
Heliocentric Distance	$0.308 - 0.467$ au
Eccentricity	0.206
Inclination	7.0°
Axial Tilt	$< 0.027°$
Rotation Period	58.6 days
Orbital Period	88.0 days

Table 1.1. Basic information on Mercury.

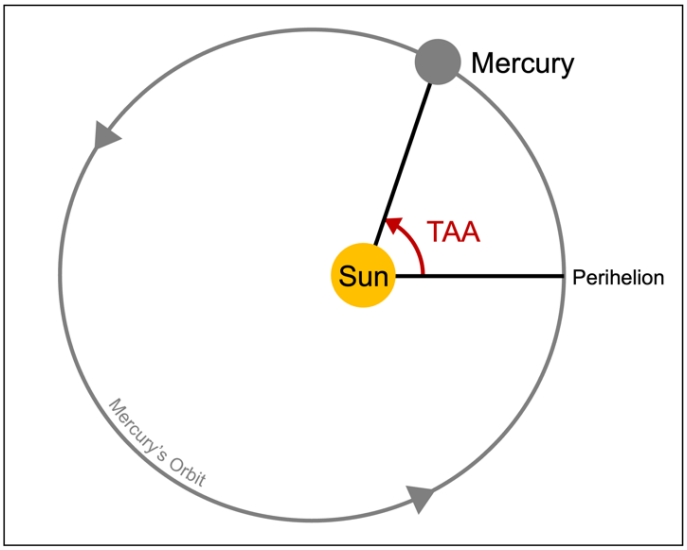

Fig. 1.2. Diagram depicting the definition of true anomaly angle (TAA).

Species	Column Density (/cm^2)
Na	$(1.2–2.0) \times 10^{11}$
Mg	1×10^{11}
O	4×10^{10}
H	5×10^{9}
K	$(0.8 – 1.3) \times 10^{9}$
Ca	$(0.3 – 1.0) \times 10^{9}$
Fe	$< 3 \times 10^{8}$
Al	1.5×10^{7}

Table 1.2. Major components of Hermean exosphere.

The following atoms are also present: Ar, CO_2, H_2O, N_2, Xe, Kr, Ne, and He.

1.2.2. Generation, Transportation, and Loss Processes

1.2.2.1. Generation Processes

Hermean exosphere is generated mainly by the desorption of atoms and molecules from the surface minerals through the following four processes: thermal desorption (TD), photo-stimulated desorption (PSD), charged particle sputtering (CPS), and micro-meteoroid impact vaporization (MIV).

TD is a phenomenon in which particles in minerals acquire thermal energy and are ejected into the exosphere. Ejection rate sharply increases above the temperature of 500–700 K, which varies depending on the binding energy and the vibration frequency of particles in minerals. The velocity distribution of ejected particles follows Maxwell distribution corresponding to the surface temperature. Ejected particles have very low energy and soon re-impact on the surface within a short time, approximately 10 min. Therefore, TD hardly contributes to the exospheric structure. However, repeated ejection and re-impact causes volatiles to migrate to low-temperature regions, which has

a large impact on exospheric ejection rates by other ejection processes (e.g., Hunten and Sprague, 1997).

PSD is a phenomenon in which neutral atoms are ejected into the exosphere through the combination of electrons on the surface excited by the solar energy and positive ions bound to the surface. Ejection rate is proportional to UV flux. A similar phenomenon also occurs when electrons incident on the surface, which is called electron-stimulated desorption (ESD). The energy distribution of ejected particles is often approximated by Maxwell distribution of approximately 1,500 K, referring to the experiment of Yakshinskiy and Madey (1999). Weibull distribution is also sometimes used, as in Burger et al. (2010), which refers to the experiment of Johnson et al. (2002).

In CPS, neutral atoms are ejected from the surface due to the momentum transfer due to the collision of ions. The ejection rate is proportional to the ion flux. As the temperature rises, the kinetic energy of electrons is also used for other processes such as ESD, resulting in the reduction of sputtering efficiency (Leblanc and Johnson, 2010). The energy distribution is often approximated by the Sigmund Thomson distribution, referring to the experiment of Wiens et al. (1997). It has also been highlighted that sputtering causes weakly bonded Na atoms to diffuse on the surface and to increase efficiency of TD and PSD (Mura et al., 2009).

Impact of micro-meteoroid also eject surface materials including refractory ones into exospheres. This process is called MIV. Energy distribution of ejected particles are often expressed by the Maxwell distribution of 3,000–5,000 K based on the experiment of Eichhorn (1978). When celestial bodies cross the ecliptic plane, an increased amount of collided dusts augments the number of ejected particles. Besides, intense impact of comet dust trail sometimes causes enhancement of exosphere over small areas and over

short periods.

1.2.2.2. Transportation Processes

Since even the number density of Na, the most abundant exospheric species, is less than 2×10^{-4} cm^{-3} and the mean free path is larger than 10^5 km, interparticle interactions can be ignored. Therefore, only three forces should be considered: gravity of Mercury, gravity of the Sun, and solar radiation acceleration. Solar radiation acceleration is the acceleration process in the anti-solar direction due to the absorption and re-emission of solar emission. This process contributes greatly to the trajectory of particles with relatively high emission efficiency (g-factor), such as Na and Ca.

1.2.2.3. Loss Processes

Exospheric neutral Na atoms are lost due to several processes such as outflow from the sphere of influence of Mercury, photo-ionization, and charge exchange. Although the escape velocity on Mercury is 4.2 km/s, solar radiation pressure and inertial force makes it much lower especially towards the evening. The lifetime of Na against photo-ionization at the heliocentric distance of 1 au was estimated to be 6.2×10^4 s, 1.7×10^5 s, and 1.9×10^5 s by experiments, theoretical calculation (Huebner et al., 1992) and observations of comets (Fulle et al., 2007), respectively. As it is proportional to the square of the heliocentric distance, it is expected to become ~ 10^4 s (~ 3 hr) on Mercury. Contrarily, the lifetime of Na against charge exchange is thought to be 23–64 hr (Smyth and Marconi, 1995), which is longer than photoionization.

1.2.3. Observations

1.2.3.1. Marinar 10

Mariner 10 was the first spacecraft to fly by Mercury. Although it approached Mercury only three times from 1974 to 1975, it achieved valuable results. First, the magnetometer revealed that Mercury has an intrinsic magnetic field despite its small size (Ness et al., 1974). Additionally, the UV spectroscopy detected H, He (Broadfoot et al., 1974), and O (Shemansky and Broadfoot, 1977) in the exosphere for the first time.

1.2.3.2. Ground Observations

As the maximum elongation of Mercury from the Sun seen from the Earth is 28°, it can only be observed for a short period of time just before sunrise or just after sunset. Nonetheless, after the exploration by Mariner 10, observations by ground telescopes detected the existence of atoms such as Na (Potter and Morgan, 1985), K (Potter and Morgan, 1986), and Ca (Bida et al., 2000) in the exosphere. Especially for Na with a large g-factor, ground observations revealed that there are diurnal changes (Potter et al., 1999), dawn-dusk asymmetry (Sprague et al., 1997), and weak north-south asymmetry (Schleicher et al., 2004) in the amount of exospheric Na. Additionally, it has been observed that the Na tail extends in the anti-Sunward direction to 1,400 Mercury radius due to solar radiation acceleration (Baumgardner et al., 2008). Mangano et al. (2015) classified the radiance distribution of Na into eight patterns, and they confirmed that mid-latitudes of the northern and southern hemispheres tend to become brighter. Massetti et al. (2017) observed the fluctuations of 15-minute and 1-hour periods, which attributed them to ion precipitation and variations of photoionization lifetimes due to variations in solar flux, respectively.

1.2.3.3. MESSENGER

The Mercury Surface, Space Environment, Geochemistry, and Ranging (MESSENGER) spacecraft is a spacecraft led by National Aeronautics and Space Administration (NASA) and orbited Mercury from 2011 to 2015. It is the first and the only orbiter of Mercury currently. The exosphere was observed mainly by the Mercury Atmospheric and Surface Composition Spectrometer (MASCS). It detected exospheric Mg for the first time (McClintock and Lankton, 2007). Additionally, long term observations of Na, Ca, and Mg in the exosphere revealed that Na is primarily ejected through PSD (Cassidy et al., 2015), and Ca and Mg are mainly ejected by MIV (Burger et al., 2014; Merkel et al., 2017). It has also been considered that intense collisions of dust streams derived from 2P/Encke comet contribute to ejection of Na and Ca (Suzuki et al., 2020; Killen and Hahn, 2015). Furthermore, it is pointed out that Na D1 and D2 lines are so bright that their radiance is no longer proportional to Na column density in the lower altitude due to multiple scattering of photons (Cassidy et al., 2015).

1.2.3.4. BepiColombo

BepiColombo is an ongoing mission led by European Space Agency (ESA) and Japan Aerospace Exploration Agency (JAXA) (Millilo et al., 2020; Murakami et al., 2020). It was successfully launched in October, 2018, and will start orbiting Mercury in December, 2025. It consists of two probes, Mio and MPO. Mio flies at higher altitudes mainly to observe the exosphere and plasma environments, while MPO flies at lower altitudes mainly to observe the surface layer. The Mercury's Sodium Atmosphere Spectral Imager (MSASI: Yoshikawa et al., 2010) onboard Mio will capture the D2 emission line of Na atoms in the exosphere with a very high wavelength resolution.

Besides, the Probing of Hermean exosphere by ultraviolet spectroscopy (PHEBUS: Quémerais et al., 2020) onboard MPO will observe distributions of exospheric atoms such as Na, Ca, Mg, and H, and attempt to detect undiscovered species such as Si, Fe, and C. BepiColombo already performed swing-bys twice, and initial data analysis is underway (e.g., Harada et al., 2022).

1.2.4. Model

1.2.4.1. Chamberlain Model

The Chamberlain model (Chamberlain, 1963) is an analytical model that calculates the particle distribution in exospheres assuming the number density and temperature at the exobase. Based on Liouville's theorem, the spread of phase-space density of particles in the exosphere is calculated for each of three orbital types: ballistic, satellite, and escape. The number density $n_{tot}(r)$ is calculated by the following equations:

$$n_{tot}(r) = \zeta_{tot} n_0 e^{-(\lambda - \lambda_0)} \tag{1.1}$$

where n_0 is number density at the exobase. λ and λ_0 are escape parameters at the altitude of r and at the exobase, respectively, calculated by:

$$\lambda(r) \equiv \frac{GMm}{k_B T(r + R_{Me})} \tag{1.2}$$

$$\lambda_0 \equiv \frac{GMm}{k_B T R_{Me}} \tag{1.3}$$

where G and k_B are gravitational constant and Boltzmann constant, respectively, M and m are mass of Mercury and particles, respectively, T is the temperature of particles, and r and R_{Me} are the altitude from the surface and radius of Mercury, respectively. ζ_{tot} is a partition function, which is the sum of the partition function of particles in the ballistic, satellite, and escaping orbits:

$$\zeta_{tot} = \zeta_{bal}\left(\lambda(r)\right) + \zeta_{sat}\left(\lambda(r)\right) + \zeta_{esc}\left(\lambda(r)\right) \tag{1.4}$$

$$\zeta_{bal}(\lambda) = \frac{2}{\pi^{\frac{1}{2}}}\left\{\gamma\left(\frac{3}{2},\lambda\right) - \frac{(\lambda_0^2-\lambda^2)^{\frac{1}{2}}}{\lambda_0}e^{-\psi_1}\gamma\left(\frac{3}{2},\lambda-\psi_1\right)\right\} \tag{1.5}$$

$$\zeta_{sat}(\lambda) = \frac{2}{\pi^{\frac{1}{2}}}\frac{(\lambda_0^2-\lambda^2)^{\frac{1}{2}}}{\lambda_0}e^{-\psi_1}\gamma\left(\frac{3}{2},\lambda-\psi_1\right) \tag{1.6}$$

$$\zeta_{esc}(\lambda) = \frac{1}{\pi^{\frac{1}{2}}}\left[\Gamma\left(\frac{3}{2}\right) - \gamma\left(\frac{3}{2},\lambda\right) - \frac{(\lambda_0^2-\lambda^2)^{\frac{1}{2}}}{\lambda_0}e^{-\psi_1}\left\{\Gamma\left(\frac{3}{2}\right) - \gamma\left(\frac{3}{2},\lambda-\psi_1\right)\right\}\right] \tag{1.7}$$

$$\psi_1(\lambda) \equiv \frac{\lambda^2}{\lambda+\lambda_0} \tag{1.8}$$

where Γ and γ are the gamma function and the incomplete gamma function, respectively. Detailed derivation means are described in Appendix 1.A1.

As this model deals only with a single particle species and does not consider loss processes, chemical reactions such as photodissociation and photoionization cannot be dealt with. This model is used to analyze exospheric data obtained by MESSENGER/ MASCS (e.g., Cassidy et al., 2015), as not the lifetime against photodissociation and photoionization but the velocity distribution derived from temperature mainly makes the number density distribution within the field of view of MASCS. Derived models include a two- and three-dimensional model (Vidal-Madjar and Bertaux, 1972), and a model which specializes in geocorona (Bishop, 1991).

1.2.4.2. Numerical Simulations

For Mercury, which is hard to be observed by both ground telescopes and spacecrafts, studies with numerical simulations play a particularly important roles. Since chemical reactions are relatively non-dominant in the Hermean exosphere, the

Monte Carlo method is often used to calculate exospheric distributions. Several theoretical models were constructed to explain the results of ground observations (e.g., Leblanc and Johnson, 2003, 2010; Mura et al., 2009) and the observations of MESSENGER (Gamborino et al., 2019; Suzuki et al., 2020). For example, seasonal variability of Na ejection rate through each ejection process was estimated by Leblanc and Johnson (2010).

1.2.5. Direct Link between Exosphere and Surface

Observational data of the surface obtained by X-ray Spectrometer (XRS) onboard MESSENGER revealed that Mg was concentrated on the lava plain from 240°E to 300°E (Weider et al., 2015; Nittler et al., 2020). Contrarily, observational data of the exosphere by MASCS revealed that Mg emissions in the exosphere are also enhanced above that region when seasonal variation component and local-time dependent component are removed (Merkel et al., 2018). This result is noted as the first and only example of the direct link between the SBE and the surface abundance distribution on Mercury.

1.3. **Comae of Comets**

1.3.1. Basic Information

1.3.1.1. Construction of Comets

Comets consist of three structures: nuclei, comae, and tails.

Nuclei are made up of ice and dust composed of volatile and refractory substances, respectively. Table 1.3 shows compositions of cometary ice (based on Bockelée-Morvan

Molecules	Abundance Ratio ($H_2O \equiv 100$)	Sublimation Temperature (K)
H_2O	100	152
CO	0.4–20	25
CO_2	2–10	72
CH_4	0.3–2	31
CH_3OH	1–6	99
H_2CO	0.1–1	64
NH_3	0.5–2	78
H_2S	0.1–2	57

Table 1.3. Compositions of ice of comets and their sublimation temperature.

Abundance of other components is less than 1/100 of H_2O.

et al., 2004 and Cochran et al., 2015) and their sublimation temperatures (based on Yamamoto, 1985). The typical size of nuclei is several kilometers. C/2014 UN_{271} (Bernardinelli-Bernstein) is the comet with the largest nucleus, whose diameter is 137 km (Lellouch et al., 2022).

Comae are envelope of gas and dust ejected from nuclei. When comets are observed, they look vague because of the comae. A spatial scale of comae is typically 10^6–10^7 km, which is comparable to the diameter of Sun. Highly volatile CO_2 and CO begin to sublimate at the heliocentric distance of approximately 30 au, while H_2O do not sublimate until comets reach inside 3 au. Around the heliocentric distance of 1 au, sublimation of CO_2 and CO is almost complete and H_2O is dominant in comae. As their extended comae can be easier to be observed while their nuclei cannot, methods for assuming nucleus surface compositions and activities from coma observations are very useful.

Tails are composed of three types. The first is a dust tail, which appears curved due

to the inertial forces and solar radiation acceleration. The second is an ion tail, extending in a straight line opposite the Sun as ions move along the magnetic field. The third is a Na tail (e.g., Cremonese et al., 1997). As Na has a large g-factor and a large solar radiation acceleration, it also forms a tail-like structure. These tails sometimes reach up to 1 au in length (e.g., Jones et al. 2000).

1.3.1.2. Classification of Comets According to Their Orbits

Comets are characterized by large eccentricities, and are frequently classified into several types according to their orbits (Table 1.4). Among comets originating in the solar system, those with an orbital period shorter than 200 years are called short-period comets (SPCs), and others are called long-period comets (LPCs). Non-periodic comets with an eccentricity larger than 1 (hyperbolic orbits) are also customarily called "long-period" comets. Among SPCs, comets with an orbital period shorter than 20 years are

<table>
<tr><th>Eccen-tricity</th><th>Classification 1</th><th>Classification 2</th><th>Classification 3</th><th>Orbital Period</th><th>Possible Origins</th></tr>
<tr><td rowspan="3">$e < 1$</td><td rowspan="3">Periodic comets</td><td rowspan="2">Short period comets</td><td>Jupiter family comets</td><td>$P < 20$ yr</td><td>Edgeworth-Kuiper belt</td></tr>
<tr><td>Halley type comets</td><td>20 yr $< P <$ 200 yr</td><td>Oort Cloud</td></tr>
<tr><td rowspan="2">Long period comets</td><td rowspan="2">Oort cloud comets</td><td>$P >$ 200 yr</td><td rowspan="2">Oort Cloud</td></tr>
<tr><td>$e > 1$</td><td>Non-periodic comets</td><td>–</td></tr>
<tr><td>$e \gg 1$</td><td colspan="3">Interplanetary objects</td><td>–</td><td>Outside of the Solar system</td></tr>
</table>

Table 1.4. Classification of comets according to their orbits.

sometimes called Jupiter family comets (JFCs) and the others are called Halley type comets (HTCs). JFCs and HTCs are thought to originate mainly in the Edgeworth-Kuiper belt and Oort Cloud, respectively, and their orbits have been significantly changed by the gravity of outer planets such as Jupiter. LPCs are thought to come from the Oort Cloud and they are also called Oort cloud comets (OCCs). According to Small-Body Database Query (https://ssd.jpl.nasa.gov/tools/ sbdb_query.html) provided by NASA/JPL, the number of JFCs, HTCs, and OCCs currently is approximately 600, 200, 2900, respectively. Finally, objects which have an extremely large eccentricities and are thought to be born outside our solar system are called interplanetary objects (IOs). Only two IOs have been found thus far: 1I/'Oumuamua (e.g., Meech et al., 2017) and 2I/Borisov (e.g., Guzik et al., 2020). Their eccentricities are 1.2 and 3.4.

1.3.2. Generation, Transportation, Emission, and Loss Processes

1.3.2.1. Generation and Loss Processes

Since comets are rich in volatiles, their atmospheres are primarily composed of sublimated volatiles. Three main sublimation sources are present: the surface of nuclei, the interior of porous nuclei, and the extended source.

First, sublimation from the nucleus surface is described. The saturated water vapor pressure from the surface is expressed by the following Clausius-Clapeyron equation as a function of the surface temperature:

$$p(T_s) = p_{ref}\, exp\left\{\frac{L}{k_B N_A}\left(\frac{1}{T_{ref}} - \frac{1}{T_s}\right)\right\} \tag{1.9}$$

where p_{ref} and T_{ref} are reference values of saturated vapor pressure and surface temperature (e.g., Hadraoui et al. 2015). Based on this equation, vapor pressure is

empirically approximated by the following equation (Washburn, 1928):

$$log_{10}\{p(T_s)\ [mmHg]\} = -\frac{2445.5646}{T} + 8.2312\, log_{10}\, T - 0.01677006T \quad (1.10)$$

The surface temperature of comets is calculated by the following energy balance equation taking into account the latent heat of sublimation (e.g., Squires and Beard, 1961):

$$F_0 r_H^{-2}(1 - A_V)\,\overline{cos\,\theta} = (1 - A_{IR})\sigma T^4 + L(T)Z(T) \quad (1.11)$$

The left hand side expresses the amount of received heat. F_0, r_H, A_V and $\overline{\cos\theta}$ are solar constant, heliocentric distance (in au), visible albedo, and effective projection factor for the surface, respectively. The first term of the right hand side represents the infrared radiation. $(1 - A_{IR})$ and σ are emissivity and Stefan Boltzmann constant, respectively. T is radiation equilibrium temperature of the surface. The second term expresses cooling by sublimation of ice. $L(T)$ is latent heat of sublimation of ice. CO and CO_2 are dominant in comae with the heliocentric distance larger than 2.5–3 au, and H_2O becomes dominant inside it.

For molecules with higher volatility than H_2O such as CO and CO_2, sublimation also occurs from the interior ice of pore-rich nuclei. Temperature gradient inside nuclei can be described by the one-dimensional heat conduction equation:

$$\rho C \frac{\partial T(r,t)}{\partial t} - \frac{1}{r^2}\frac{\partial}{\partial r}\left(r^2 \kappa \frac{\partial T(r,t)}{\partial r}\right) = Q_{in} \quad (1.12)$$

where ρ, C, κ, and r are density of the nucleus, specific heat, thermal conductivity, and depth from the nucleus surface, respectively. Q_{in} is internal energy source, such as decay of radioactive isotopes (Whipple and Stefanik 1966) and transition of ice from amorphous to crystals (Patashnick et al. 1974). As comets have small thermal inertia and the temperature gradient in the horizontal direction is much smaller than that in the

radial direction, one-dimensional equation is sufficient. Due to this radial temperature gradient, more volatile materials exist deeper in the nucleus. In Belton, (2010), jet-like ejection of CO and CO_2 exuded from the interior was reproduced by numerical calculation.

Caught in the sublimation of ice, dusts are also ejected. Extended dust comae can also be the source of volatile matter, since lifted-up dust contains icy grains. In C/1996 B_2 (Hyakutake), icy grain halo surrounding the nucleus was observed (Davis et al., 1997). Additionally, observations of 103P/Hartley 2 by the EPOXI mission demonstrated for the first time that some of CN molecules are supplied by an extended source (A'Hearn et al., 2011).

Molecules in comae dissociate into daughter molecules or atoms through photodissociation reactions caused by UV rays. Then, the generated daughter particles are lost by photodissociation or photoionization. Tables 1.5 and 1.6 show the lists of photodissociation reaction of H_2O and one of its daughter molecules, OH, and their destruction rate under the quiet Sun condition, based on Combi et al. (2004). Although solar wind also destroys H_2O, the destruction rate is one order lower than photodissociation reaction (Combi et al., 2004). According to the database of Photo Ionization/Dissociation RATES (https://phidrates.space.swri.edu/), lifetime of hydrogen atoms against photoionization is 1.4×10^7 s.

Solar UV Wave-length (nm)	Reaction		Velocities of Products (km/s)		Destruction Rate (10^{-6} /s)
135.7 – 186.0	$H_2O + h\nu$	$\rightarrow H + OH(X^2\Pi)$	18.5 (H)	1.09 (OH)	4.84
		$\rightarrow H_2 + O(^1D)$	< 13.7 (H_2)	< 1.71 (O)	0.05
121.6	$H_2O + h\nu$	$\rightarrow H_2 + OH(X^2\Pi)$	17.2 (H)	1.01 (OH)	3.02
		$\rightarrow H + OH(A^2\Sigma^+)$	5 (H)	0.3 (OH)	0.35
		$\rightarrow H_2 + O(^1D)$	< 15 (H_2)	< 1.8 (O)	0.43
		$\rightarrow H + O + H$	< 7.4 (2H)	< 0.87 (O)	0.52
98.4 – 135.7	$H_2O + h\nu$	$\rightarrow H + OH(X^2\Pi)$	< 37 – 27 (H)	< 2.2–1.6 (OH)	0.30
		$\rightarrow H + OH(A^2\Sigma^+)$	< 25 – 0 (H)	< 1.5 – 0 (OH)	0.03
		$\rightarrow H_2 + O(1D)$	< 22 – 14 (H_2)	< 2.7 – 1.7 (O)	0.04
		$\rightarrow H + O + H$	< 17 – 0 (2H)	< 2.0 – 0 (O)	0.05

Table 1.5. Photochemical reactions of H_2O vapor.

Solar UV Wave-length (nm)	Reaction		Velocities of Products (km/s)		Destruction Rate (10^{-6} /s)
216.0	$OH + h\nu$	$\rightarrow H + O(^3P)$	8 (H)	0.5 (O)	3.0–6.1
245.0	$OH + h\nu$	$\rightarrow H + O(^3P)$	11 (H)	0.7 (O)	0.5
140.0 – 180.0	$OH + h\nu$	$\rightarrow H + O(^3P)$	22–26 (H)	1.4–1.6 (O)	1.4
121.6	$OH + h\nu$	$\rightarrow H + O(^1D)$	26.3 (H)	1.6 (O)	0.3
		$\rightarrow H + O(^1S)$	17.1 (H)	1.1 (O)	0.05
		$\rightarrow H + O(^1D)$	26.3 (H)	1.6 (O)	0.10
< 120.0	$OH + h\nu$	$\rightarrow H + O(^3P)$	22 (H)	1.4 (O)	< 0.01

Table 1.6. Photochemical reactions of OH vapor.

1.3.2.2. Transportation Processes

Unlike the case of Mercury, which was introduced in Subsection 1.2.2.2, the gravity of comets is too small gravity to affect the trajectory of gas molecules. Instead, as comae tend to have a higher number density near the nuclei than in the Hermean exosphere, interatomic collisions play an important role. Motion of gas is characterized by the Knudsen number Kn expressed by the following equation:

$$Kn \equiv \frac{\lambda}{L} \tag{1.13}$$

λ and L are the mean free path and the typical spatial scale of the system, respectively. The region just above the nucleus within 10 – 100 mean free paths (Davidsson, 2008) forms a Knudsen layer, and particles behave fluidly above it ($Kn < 10^{-2}$) as described by the Euler or Boltzmann equations. Thereafter that, the system transitions to the collisionless system via the region where inter-particle collisions are moderately effective ($10^{-2} < Kn < 10^{2}$) described by Boltzmann equation (e.g., Marschall et al., 2020). According to the numerical calculation by Tenishev et al. (2008) assuming the case of 67P/Churyumov-Gerasimenko (67P/CG), the region where collisions occur sufficiently and motion of hydrogen atoms couple with that of other molecules is up to the altitude of 20 km when the heliocentric distance is 1.29 au and the water production rate is 5×10^{27} /s.

1.3.2.3. Emission Processes

For optical observations, it is important to understand light emission processes and their efficiency. Particles in comae emit light mainly through the two processes: solar resonant scattering and electron collision excitation. Solar resonant scattering is a

phenomenon in which particles selectively absorb sunlight at specific wavelengths and the excited particles isotropically re-emit light soon. The g-factor is calculated by the following equation under the optically thin condition:

$$g = \frac{\pi e^2}{m_e V_c} \pi F f_{ij} \quad (1.14)$$

where $e, m_e, V_c, F,$ and f_{ij} are elementary charge, electronic mass, speed of light, and oscillator strength, respectively. Under the optically thick condition, the radiance is not proportional to the column density of particles due to multiple scattering. Richter et al. (2000) reproduced the spectra of C/1996 B_2 (Hyakutake) obtained by Hubble Space Telescope (HST) using a radiation transfer model. However, a few examples of UV observations with high spatial resolution exist, and therefore, few studies compute the spatial distribution of radiance of comae considering multiple scattering using radiation transfer models.

Electron collision excitation is a phenomenon in which high-energy electrons generated by solar UV rays hitting molecules in comae collide with other molecules (e.g., H_2O molecules), resulting in the UV emission by dissociated atoms (e.g., H and O atoms). In the case of this process, forbidden lines such as the OI1356 emission line is also detected. For comets, the OI1356 emission line was detected in the inner coma at the altitude of 10–80 km of 67P/CG by the Rosetta spacecraft (Feldman et al., 2015). Besides, enhancement of OI1356 as well as Ly-β, OI1304, and CI1657 was observed when the coronal mass ejection occurred in October, 2015 (Noonan et al., 2018).

1.3.3. Observations

1.3.3.1. Explorations

Table 1.7 summarizes the exploration missions of comets. Each mission is also summarized in great detail by Snodgrass et al. (2022). Particularly, the Rosetta mission is important for the study of physics in comae and the relationship between comae and surface materials.

Rosetta observed 67P/CG for two years from August, 2014 to September, 2016. Fig. 1.3 shows the orbit of 67P/CG during the observation period. In addition to the detailed observations of the nucleus (e.g., Jorda et al., 2016), observations of the coma provided us important insights on the formation environment and surface active regions. Bieler et al. (2015a) and Gulkis et al. (2015) detected periodicity in the production rate of the coma due to rotation and nucleus shape. Bieler et al. (2015b) detected abundant oxygen molecules and Rubin et al. (2015) detected nitrogen molecules for the first time on comets, suggesting that 67P/CG was formed in a very cold environment. Fougere et al. (2016) followed by Combi et al. (2020) estimated distributions of active regions through the construction of a 3D coma model comparing with that of the data obtained by

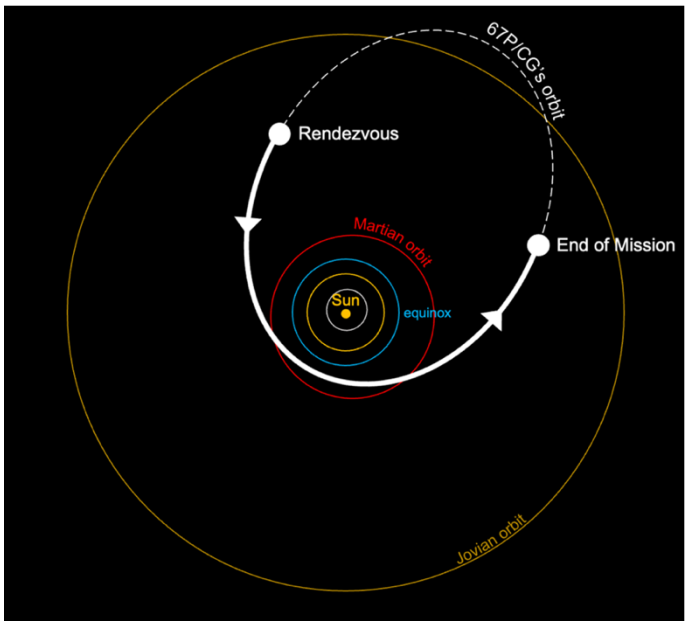

Fig. 1.3. Schematic representation of the orbit of 67P/CG and the Rosetta spacecraft.

Double Focusing Mass Spectrometer (DFMS) of Rosetta Orbiter Spectrometer for Ion and Neutral Analysis (ROSINA) onboard Rosetta. As a result, it was found that H_2O was mainly ejected from the Hapi region in the constricted part of the nucleus, while CO_2 was ejected from the southern hemisphere. Additionally, H_2O, O_2, and NH_3 molecules in the coma decreased rapidly after the passage of the vernal equinox, while CO_2, CO, H_2S, CH_4, and HCN decreased more moderately and their production rates have north-south asymmetry, which indicates that there may be two types of ice, H_2O ice and CO_2 ice (Gasc et al., 2017). Water production areas are found to fluctuate according to the changes in sunlight conditions and subsurface temperature by Hansen et al. (2016), Hassig et al. (2015), and Hoang et al. (2017). Contrarily, Luspay-Kuti et al. (2015) pointed out that variability of most minor species in the southern hemisphere coma correlated with that of either H_2O or CO_2, while only CH_4 showed different diurnal variation from that of the other species. Then, it was suggested that further discussion of nuclear properties and thermal processes is necessary.

Additionally, many isotopes such as $HD^{16}O$, $H_2{}^{18}O$ (Schroeder I et al. 2018), $^{13}C^{16}O_2$, and $^{12}C^{18}O^{16}O$ (Hassig et al., 2017) were also measured by Rosetta. Particularly, the D/H ratio (Altwegg et al., 2015) and the Ar/H_2O ratio (Balsiger et al., 2015) are far from those of the ocean and the atmosphere of the Earth, which may indicate that 67P/CG is not a source of water and volatiles on the Earth.

Now, ESA and JAXA are planning a long-period comet fly-by mission called Comet Interceptor (CI). This mission will be covered in more detail again in Chapter 5.

Comets	Missions	Period	Major Achievement
21P /Giacobini –Zinner	ICE (extended mission of ISEE–3)	1985	First comet fly-by Passing through the magnetotail[1]
1P/ Halley	ICE, Vega 1, Vega 2, Giotto, Suisei, Sakigake	1986	Detailed imaging of the nucleus[2]
26P /Grigg –Skjellerup	Giotto	1992	Detection of jet activity possibly ejected from the fragment of the nucleus[3]
19P /Borrelly	Deep Space 1	2001	Imaging surface morphological structures[4]
81P /Wild 2	Stardust	2004	Sample return of the comet and interstellar media[5]
9P /Tempel 1	Deep Impact	2005	First impactor on comets exploring interior structures of the nucleus[6]
103P /Hartley 2	EPOXI (extend mission of Deep Impact)	2010	Detection of hyperactivity and anisotropic coma[7]
9P /Tempel 1	Stardust-NExT (extended mission of Stardust)	2011	Imaging the crater artificially made by Deep Impact[8]
67P /Churyumov –Gerasimenko	Rosetta	2014 – 2016	First rendezvous[9]
LPCs or IOs (TBD.)	Comet Interceptor	Launched in 2029	First flyby of LPCs[10]

Table 1.7. List of comet exploration missions.
[1] Slavin et al., 1986. [2] Keller et al., 1986. [3] McBride et al., 1997. [4] Britt et al., 2004.
[5] Sandford et al., 2021. [6] Sunshine et al., 2007. [7] A'Hearn et al., 2011.
[8] Veverka et al., 2013. [9] Rubin et al., 2020. [10] Snodgrass and Jones, 2019.

1.3.3.2. Observations from the Earth

For ground observations, visible light, infrared rays, and radio waves are mainly used to avoid absorption by the atmosphere. In these observations, the physical properties of dust particles can be estimated from absorption bands, and the amount of gas molecules can be quantified from the observations of emission lines associated with rotational and vibrational transitions. For example, Kadono et al. (2007) observed 9P/Tempel 1 using Subaru Telescope during the Deep Impact mission and found that the surface of the nucleus was covered with a layer of several tens of centimeter thick containing many carbonaceous particles. This indicates that short-period comets retain unmetamorphosed materials on their surfaces even after experiencing repeated perihelion passages. In Shinnaka et al. (2020), CO_2/H_2O ratio of 21P/Giacobini-Zinner was calculated through the observations of the oxygen emission lines using Subaru Telescope. As a result, it was found to be depleted in CO_2 and to be formed in a warm environment. In Ootsubo et al. (2012), the H_2O, CO, and CO_2 ratios of 18 comets were calculated using the Akari satellite and estimated the temperature and redox environments where comets were formed.

Observations using UV rays enable us to investigate the distribution of daughter atoms such as H that have dissociated from parent molecules and spread further than parents. Therefore, it promotes understanding of the kinetic theory of gaseous atoms in comae. Additionally, chemical properties can be discussed as well as the observations using other wavelength range, since production rate of parent molecules can be estimated from the distribution of daughter species. Since it is hard to perform UV observations from the ground, instruments are limited. The IUE satellite, the FUSE satellite, Space Telescope Imaging Spectrograph (STIS) onboard HST, Solar Wind

Anisotropies (SWAN) camera onboard the Solar and Heliospheric Observatory (SOHO), and Alice onboard the Rosetta spacecraft were used for UV observations of comets. Particularly, Ly-α observations were conducted mainly by SOHO/SWAN (e.g., Combi et al., 2019) and HST/STIS (Weaver et al., 2008). SOHO/SWAN has a very wide field of view, although it has a low spatial resolution of 1°. It has observed so many comets and calculated their water production rates. Particularly, the dependence of water production rates on the heliocentric distance for 17 short-period comets and 44 long-period comets in Combi et al. (2019). However, there was little clear trend in differences in the dependence between comets. HST/STIS has a very high wavelength resolution, 2.2 pm, by which hydrogen Ly-α (wavelength of 121.567 nm) and deuterium Ly-α (121.534 nm) can be distinguished and hydrogen temperature can be estimated from the line width. Observations of C/2001 Q_4 (NEAT) by Weaver et al. (2008) show that the temperature widths of hydrogen and deuterium Ly-α are 2.1 pm and 0.9 pm, corresponding to the temperature of 7×10^3 K and 3×10^3 K, respectively.

1.3.4. Model

1.3.4.1. Eddington's Fountain Model

Eddington's fountain model (Eddington, 1910) assumes only diffusion of comae due to free expansion and uniform anti-solar acceleration due to solar radiation pressure. The boundary of the particle expansion on the sunward side is given by the following parabolic equation along a line parallel to the uniform acceleration:

$$x^2 + y^2 = 2z\frac{v^2}{a} + \frac{v^4}{a^2} \tag{1.15}$$

Derivation is shown in Appendix 1.A2. A Point source is assumed, and the z-axis is a

straight line passing through the source point and parallel to the acceleration vector. v and a are the initial uniform outflow velocity and uniform acceleration of emitted particles. Particle losses such as photodissociation and photoionization are not considered.

1.3.4.2. Haser Model

The Haser model (Haser, 1957) expresses the distribution of parent and daughter molecules in the steady state. The model makes three assumptions: (1) parent molecules can produce a single type of daughter molecules, (2) daughter molecules are produced from a single type of parent molecules, and (3) parent and daughter molecules move in the radial direction with respect to the nucleus at a single velocity. The specific formula is as follows:

$$n_d(r) = \frac{Q}{4\pi r^2 v_d} \frac{v_d \tau_d}{v_d \tau_d - v_p \tau_p} \left\{ exp\left(-\frac{r}{v_d \tau_d}\right) - exp\left(\frac{r}{v_p \tau_p}\right) \right\} \quad (1.16)$$

where Q is the production rate of parent molecules, r is the altitude, v_p and v_d are velocities of parent and daughter molecules, and τ_p and τ_d are lifetimes of parent and daughter molecules. Derivation is shown in Appendix 1.A3. This model has been widely used when production rates of parent molecules (e.g., HCN) are calculated from observations of daughter molecules (e.g., CN). Additionally, derived models such as the vectorial model (Festou, 1981) that can calculate the velocity, and a three-stage model (O'Dell et al., 1988) also exist.

1.3.4.3. Kaneda Model

The Kaneda model (Kaneda et al., 1986) is an analytical model specialized for

calculating the number density of H atoms. It considers three generations of parent–daughter–granddaughter (H_2O–OH–H), and the time development of the number density distribution of H atoms as a function of time elapsed from the moment the ejection of H_2O molecules begins. H atoms have two components: one is directly dissociated from H_2O molecules by $H_2O \rightarrow OH + H$ (named "component 1"), and the other is generated via OH by $H_2O \rightarrow OH + H$ and $OH \rightarrow O + H$ (named "component 2"). This model calculates the number density of H separately for these two components. The expression is as follows:

$$n_g(t,r) = \frac{Q_{g_1}\left(t - \frac{r}{v_{g_1}}\right)}{4\pi r^2 v_{g_1}} e^{-\frac{r}{\tau_g v_{g_1}}} + \frac{Q_{g_2}\left(t - \frac{r}{v_{g_2}}\right)}{4\pi r^2 v_{g_2}} e^{-\frac{r}{\tau_g v_{g_2}}} \quad (1.17)$$

$$Q_{g_1}(t) = Q_p\left\{1 - exp\left(-\frac{t}{\tau_p}\right)\right\} \quad (1.18)$$

$$Q_{g_2}(t) = \frac{Q_p}{\tau_p - \tau_d}\left\{(\tau_p - \tau_d) + \tau_d\, exp\left(-\frac{t}{\tau_d}\right) - \tau_p\, exp\left(-\frac{t}{\tau_p}\right)\right\} \quad (1.19)$$

where Q_p is the production rate of parent molecules from the nucleus, Q_{g_1} and Q_{g_2} are hydrogen generation rates of component 1 and 2, t and r are elapsed time and altitude, v_{g_1} and v_{g_2} are velocities of component 1 and 2, and τ_p, τ_d, and τ_g are lifetimes of H_2O, OH, and H, respectively. Derivation is shown in Appendix 1.A4.

As this model ignores the motion of H_2O and OH, the distribution of hydrogen atoms cannot be reproduced within 10^4 km, which corresponds to the scale length (product of the velocity and the lifetime) of these molecules. When the time t is sufficiently large, Kaneda model is consistent with the three-stage Haser model (O'Dell et al., 1988) above the altitude of the scale length of H_2O and OH molecules as shown in Appendix 1.A4. The advantage of this model is that the hydrogen density can be expressed as a function of elapsed time. Additionally, as there are few parameters, if the

focus in only on the region above the altitude of 10^4 km, then it is easier to fitting to the observational data.

1.3.4.4. Numerical Simulations

Unlike in the case of Mercury, the generation and annihilation of particles due to photodissociation reactions are important for comets. Therefore, the calculation of time development of the phase space density of the particles is better than the calculation of the trajectory of each particle using the monte Carlo method. As described in Subsection 1.3.2.2, it is necessary to properly select the system of equations to be used according to the mean free path. For example, in Bieler et al. (2015a), three numerical calculations of illumination, hydrodynamics, and kinetic models were performed and their results were compared to reproduce the observational data of 67P/CG obtained by the cometary pressure sensor (COPS) of ROSINA onboard Rosetta.

The illumination model assumes that production rates from all the surface elements of the nuclear are expressed as a function of only the insolation, and calculates production rates from the solar zenith angle of each surface element. The number density distribution of ejected particles is scaled assuming it is proportional to $1/r^2$. As much less physics is included, the consistency with observed data is lower than that of the two other models. However the advantage is that it is computationally very cheap. The hydrodynamic model (e.g., Powell et al., 1999) solves the Euler equation involving the conservation of mass, momentum, and energy. The kinetic model (e.g., Combi, 1996) is based on the Boltzmann equation. Inter-particle collisions are considered close to the nucleus using the Monte Carlo method, while in the outer comae it assumes the collisionless system. Despite the fact that this is the most realistic among the three types

of models, the computational cost tends to be the highest. Tenishev et al. (2008) calculated the number density, velocity, and temperature distributions of H2O, OH, and H in the coma of 67P/CG using the kinetic model.

1.3.5. Origin of Water of the Earth and D/H Ratio

Comets have been noted as one of the candidates for the origin of water on the Earth (e.g., Chyba, 1987). Tables 1.8 and 1.9 summarize the previous measurements of D/H ratios of comets. The D/H ratio in ocean water of the Earth, i.e., the Vienna Standard Mean Ocean Water (VSMOW) is $(1.5576 \pm 0.0001) \times 10^{-4}$. Some comets such as 46P/Wirtanen and 103P/Hartley have similar D/H values, and other comets such as 67P/CG and C/2001 Q4 (NEAT) have approximately three times higher values. Generally, comets that were formed in cold regions tend to have higher D/H ratios (Ceccarelli et al., 2014), but no correlation can be seen between D/H ratios and current orbital elements. Lis et al. (2019) pointed out that there is an anti-correlation between the fraction of active regions on the nucleus surfaces of the comets and D/H ratios. Although this may be due to the difference in comet formation environments, it is also possibly due to fractionation effects or space weathering. Further understanding of the impact of long term evolution of comets and activity on the variation of D/H ratios is required. Furthermore, in the CI mission, the D/H ratio will be measured by the Mass Analyzer for Neutrals in a Coma (MANiaC) and the Hydrogen Imager (HI) camera.

Comets	Orbital Period (yr)	Instrument	Observed Species	D/H Ratio
45P/Honda–Mrkos –Pajdušáková	5.3	HSO	HDO/H_2O	$< 2.0 \times 10^{-4}$ [1]
46P/Wirtanen	5.4	SOFIA	HDO/H_2O	$(1.6\pm0.7) \times 10^{-4}$ [2]
67P/Churyumov –Gerasimenko	6.4	Rosetta /ROSINA –DFMS	HDO/H_2O	$(5.3\pm0.7) \times 10^{-4}$ [3]
103P/ Hartley 2	6.5	HSO	HDO/H_2O	$(1.6\pm0.2) \times 10^{-4}$ [4]
8P/ Tuttle	13.6	VLT /CRIRES	HDO/H_2O	$(4.1\pm1.5) \times 10^{-4}$ [5]
1P/ Halley	75	Giotto /IMS–HIS	H_2DO+/H_3O+	$(3.1^{+0.4}_{-0.5}) \times 10^{-4}$ [6]
		Giotto /NMS	H_2DO+/H_3O+	$(3.1\pm0.3) \times 10^{-4}$ [7]
153P/ Ikeya Zhang	366	IRAM 30-m Telescope	HDO/H_2O	$< 2.5 \times 10^{-4}$ [8]

Table 1.8. List of the measured D/H ratios of short period comets.

[1] Lis et al., 2013. [2] Lis et al., 2019. [3] Altwegg et al., 2015. [4] Hartogh et al., 2011. [5] Villanueva et al., 2009. [6] Balsiger et al., 1995. [7] Eberhardt et al., 1995. [8] Biver et al., 2006.

Comets	Orbital Period (yr)	Instrument	Observed Species	D/H Ratio
C/1995 O_1 (Hale Bopp)	2.5×10^3	JCMT	HDO/H_2O	$(3.3\pm0.8) \times 10^{-4}$ [1]
C/1996 B_2 (Hyakutake)	1.0×10^5	CSO	HDO/H_2O	$(2.9\pm1.0) \times 10^{-4}$ [2]
C/2001 Q_4 (NEAT)	–	HST /STIS	D/H	$(4.6\pm1.4) \times 10^{-4}$ [3]
C/2002 T_7 (LINEAR)	–	VLT /UVES	OD/OH	$(2.5\pm0.7) \times 10^{-4}$ [4]
C/2009 P_1 (Garradd)	–	HSO	HDO/H_2O	$(2.1\pm0.2) \times 10^{-4}$ [5]

Table 1.9. List of the measured D/H ratios of long period comets.
[1] Meier et al., 1998. [2] Bockelée-Morvan et al., 1998. [3] Weaver et al., 2008.
[4] Hutsemekers et al., 2008. [5] Bockelée-Morvan et al., 2012.

1.4. **Direct Link between Exospheres and Surfaces on Other Celestial Bodies**

As mentioned in Section 1.1, SBEs are ubiquitous in planetary systems. Studies on the relationship between exospheres and surfaces were conducted also on celestial bodies other than Mercury and comets.

In the case of the Moon, comparison between the exospheric observations by the LADEE spacecraft and surface observations by the Lunar Prospector spacecraft revealed that the Na column density in the exosphere was enhanced over high albedo regions rich in Na, and that there is a positive correlation between surface K abundance and exospheric column density of K (Colaprete et al., 2016). Ground observations have also confirmed an increase in K column density over the Potassium, Rare-Earth Elements, and Phosphorous (KREEP) regions (Rosborough et al., 2019).

For Io, one of the Galilean moons, the internal magma temperature was estimated from the NaCl/KCl ratio in its SBE and the difference in their evaporation temperatures (Redwing et al., 2022). In the case of Europa, measurement of the Na/K ratio in the exosphere was suggested to be useful for constraint of the material fractionation in the inner ocean and surface ice (Johnson et al., 2002; Cipriani et al., 2009). Teolis et al. (2017) investigated the relationship of exosphere with plume activity and chemically enriched geologic terrains on Europa using numerical simulation. In Saur et al. (2015), the method to search for subsurface ocean of Ganymede through observations of its aurora oval was established. Besides, Teolis & Waite (2016) evaluated the amount of winter frost cap loss due to diffusion into the surface regolith and sputtering on Dione and Rhea, both of which are satellites of Saturn, through the comparison of exospheric observational data obtained by Cassini and numerical model.

Although there are limited observational data of SBEs of satellites of outer planets currently, new spacecrafts launched in 2030s will provide us a large amount of suggestive data which would greatly improve our understanding.

1.5. **Summary and Purpose of the Study**

Surface bounded exospheres (SBEs) are very important regions, where direct interaction between the surface of celestial bodies and surrounding space environment can be observed. Besides, as particles ejected from the surface escape into the space in short timescales of a few days or less before sufficiently mixed, production rate distributions of exospheric species are expected to be directly reflected on exosphere structures. In this chapter, dynamics of SBEs and the relationship with surface composition, focusing on Mercury and comets were summarized. On Mercury, detailed

observations of exospheric distribution and surface composition were conducted by the MESSENGER spacecraft. Particularly, the distribution of Mg in the exosphere was found to be directly linked to the surface abundance map. However, since other species were not studied, general understanding of the exosphere-surface relationship has not been achieved yet. For comets, studies on the comae and surface active regions were conducted mainly using observational data taken by the Rosetta spacecraft and numerical calculations. However, due to limited observation opportunities and strong individualities of comets, universal understanding of comets has not been acquired.

To reach my ultimate goal of developing methods for assuming nucleus composition from coma observations for comet exploration missions in the near future, I will study the physical processes of SBEs, which possibly disturb the direct links between SBEs and surfaces in this study (Fig. 1.4). In Chapter 2, I conduct a correlation analysis of exosphere and surface distributions on Mercury, for which observational data both on the exosphere and the surface are available, for atoms other than Mg using the observational data obtained by MESSENGER. From Chapter 3, comets are focused on as targets for applying the knowledge obtained through studies on Mercury. In particular, hydrogen atoms in comet comae, which can be observed even with small telescopes onboard spacecrafts, are investigated. In Chapter 3, I evaluate the fraction of active areas on the surface of the comets using observational data of the Hisaki satellite. In Chapter 4, I discuss the radiative transfer process in comae of the comets through the numerical simulation for the purpose of understanding the cause of Ly-α radiance distribution clarified by Hisaki. In chapter 5, to obtain new observational data of a comet, I conduct the design and performance evaluation of Hydrogen Imager onboard the CI spacecraft, whose plan is in progress. Finally, I examine the feasibility of

measuring the D/H ratio of comets using Hydrogen Imager in Chapter 6.

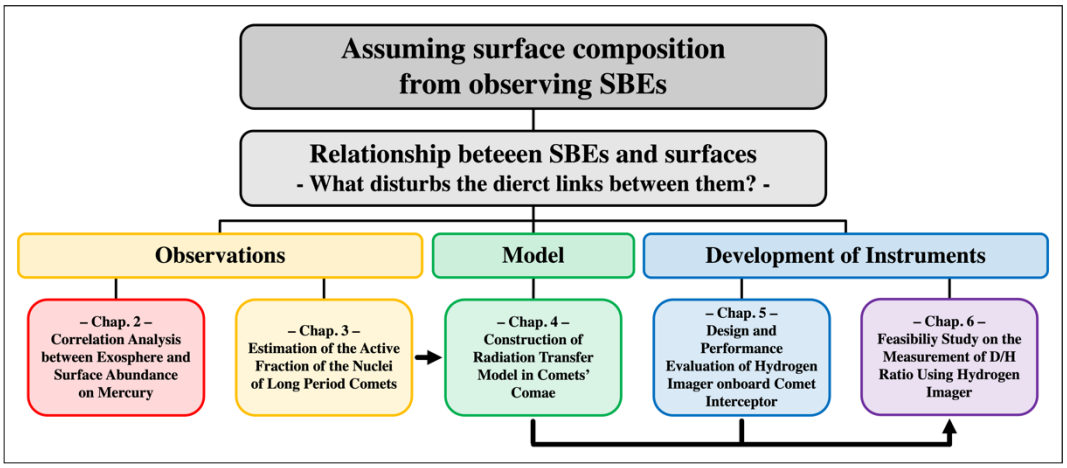

Fig. 1.4. Schematic depicting the outline of this dissertation.

2. Study on the Exosphere-surface Correlation on Mercury

As introduced in Subsection 1.2.5, observational data taken by XRS and MASCS onboard MESSENGER revealed that Mg distribution in the exosphere is correlated with the distribution of Mg surface abundance (Merkel et al., 2018). This is noteworthy as the first detection of direct link between the exosphere and the surface on Mercury. However, little discussion has been made for other atomic species. Because ejection processes and behavior in exospheres differ depending on atomic species, species adequate for assuming surface environments from SBE observations possibly also differs depending on targets. Therefore, it is necessary to investigate existence of direct links between SBEs and surfaces for various species.

In this chapter, the analysis of the correlation between the exosphere and the surface for Ca and Na on Mercury in addition to Mg, which were observed in detail by MESSENGER/MASCS, is conducted following Merkel et al. (2018). In Section 2.1, MASCS/UVVS and XRS onboard MESSENGER, whose data are used in this chapter, are introduced. The analysis methods are described in Section 2.2. In Section 2.3, the results and their interpretation are shown. At last, the expected conditions under which the exosphere-surface correlation occurs in other atomic species and other celestial bodies are discussed in Section 2.4, based on the insight obtained from the analysis of Mg, Ca, and Na on Mercury.

2.1. **Observations by MASCS/UVVS and XRS onboard MESSENGER**

The MESSENGER spacecraft, launched in 2004, orbited Mercury from 2011 to 2015 for approximately 17 Mercury years. In this study, I used the Ultraviolet and Visible Spectrometer (UVVS) channel of the MASCS to estimate the production rate of

exospheric atoms, as well as the XRS for the calculation of surface abundance.

2.1.1. UVVS Channel of MASCS

MASCS consists of two channels: UVVS and Visible and InfraRed Spectrometer (VIRS). UVVS, a grating monochromator, scans a narrow wavelength range around the resonance-scattering emission lines of several atoms. Mg, Ca, and Na spectral scans cover 283.4–287.2 nm, 421.1–424.4 nm, and 587.7–591.1 nm with 0.2 nm step size, which include MgI (285.2 nm), CaI (422.7 nm), and NaI D1 (589.8 nm) and D2 (589.1 nm), respectively. Owing to the northward line-of-sight integration (see Fig. 2 of Cassidy et al., 2015), dayside limbscans provide an altitude profile at low latitudes. Instead, they are sensitive to the dependence of the emissions on longitude (local time) and altitude. MASCS detected Mg for the first time (McClintock et al., 2009), and clarified the spatial distribution and seasonal variability of Mg (Merkel et al., 2017), Ca (Burger et al., 2014), and Na (Cassidy et al., 2015, 2016).

2.1.2. XRS

XRS consists of three planet-facing gas-proportional counter (GPC) detectors and a sun-pointing Si-PIN detector within the Solar Assembly for X-rays (SAX). XRS measured the surface (shallower than ~ 100 μm) abundances of rock-forming elements via planetary X-Ray Fluorescence (XRF). The measured elements can be distinguished based on the energy of incident X-rays and the capabilities of the instrument detectors. The four detectors of XRS cover an energy range of 1–10 keV. 1.25 keV and 3.69 keV Kα lines were observed for Mg and Ca, respectively. An abundance ratio map of Mg, Ca, Al, S, and Fe to Si was constructed, which clarified the existence of a large Mg-

concentrated terrane between 240°E and 320°E longitude in the northern hemisphere (Weider et al., 2015). As Ca fluorescence is observable only during solar flares, spatial coverage of the Ca surface abundance is still incomplete. However, it can be seen that Ca enhances around the high-Mg region (HMR) in the northern hemisphere (Nittler et al., 2020).

2.2. **Analysis**

First, the production rate of the exospheric component from the altitude profile obtained by the MASCS is deduced. All the dayside limb scan data from 2011 to 2015 were used for the analysis. The column density of exospheric atoms along the line of sight of spacecraft is approximated by the Chamberlain analytic model (Chamberlain, 1963), as follows:

$$N(z) = 2KH\zeta n_0 \, exp\left(\frac{-U + U_0}{k_B T}\right) \tag{2.1}$$

where z, n_0, and T are tangential altitude, near-surface density, and temperature, respectively. $2K$ is the ratio of the apparent column density along the line of sight of the spacecraft to the vertical column density, which is approximated by:

$$2K \sim \sqrt{\frac{2\pi(R_{Me} + z)}{H(z)}} \tag{2.2}$$

H, similar to scale height, is defined by the following equation:

$$H(z) = \frac{k_B T (R_{Me} + z)^2}{G M_{Me} M_{atom}} \tag{2.3}$$

where $M_{\mathrm{Me}}, M_{\mathrm{atom}}, R_{\mathrm{Me}}$ are the mass of Mercury, the mass of atoms, and the radius of Mercury, respectively. U and U_0 are the potentials of the particles at altitude z and at the surface, respectively, expressed by the following equations:

$$U(z) = -\frac{GM_{Me}M_{atom}}{(R_{Me}+z)} + M_{atom}b\cos Z\,(R_{Me}+z) \quad (2.4)$$

$$U_0 = U(z=0) \quad (2.5)$$

where b and $\cos Z$ are the solar radiation acceleration and the cosine of the solar zenith angle, respectively. In Equation (2.1), ζ is the following partition function:

$$\zeta = \frac{1}{2} + \frac{1}{2}erf\left(\sqrt{\lambda}\right) - \sqrt{\frac{\lambda}{\pi}}e^{-\lambda} - \frac{\sqrt{\lambda_0^2-\lambda^2}}{2\lambda_0}e^{-\psi}\left(1+erf\left(\sqrt{\lambda-\psi}\right)\right) + \sqrt{\frac{\lambda(\lambda_0-\lambda)}{\pi\lambda_0}}e^{-\lambda} \quad (2.6)$$

where λ, λ_0 are the escape parameters at altitude z and at the surface defined as:

$$\lambda(z) = \frac{GM_{Me}M_{atom}}{k_B T(R_{Me}+z)} \quad (2.7)$$

$$\lambda_0 = \lambda(z=0) \quad (2.8)$$

and ψ is defined as:

$$\psi(z) = \frac{\lambda(z)^2}{\lambda(z)+\lambda_0} \quad (2.9)$$

The Chamberlain model does not consider photoionization. However, photoionization is not effective within the field of view of MASCS (<10^4 km) because typical flight scales (the product of the photoionization lifetime and the thermal velocity) of Mg, Ca, and Na at a heliocentric distance of 0.4 au are approximately $10^{6.5}$ km, $10^{4.5}$ km, and 10^5 km, respectively.

The apparent column density $N(z)$ in cm^{-2} is derived from the observed radiance $4\pi I$ in Rayleigh from the following conversion formula:

$$N = 10^6 \frac{4\pi I}{g} \quad (2.10)$$

where g is the g-factor calculated by Equation (1.14). In calculation of g-factor, the values of oscillation strength and solar flux are taken from the National Institutes of Standards and Technology Atomic Spectra Database Lines Form (https://physics.nist.gov/PhysRefData/ASD/ lines_form.html) and the LASP Interactive

Solar Irradiance Datacenter (LISIRD; https://lasp.colorado.edu/lisird/data/sorce_ssi_l3/), respectively. The g-factor is assumed to be uniform for a single TAA assuming that atoms are at rest with respect to Mercury, although it has a standard deviation that is less than approximately 30% owing to the atoms' radial velocity distribution against the sun. The production rate S is estimated from the product of the near-surface density and first-order moment of velocity distribution function:

$$S = n_0 \int_0^{\infty} v^2 dv \int_{\theta=\frac{\pi}{2}}^{\theta=0} d\cos\theta \int_0^{2\pi} d\phi\, f(v,T)\, v = \frac{n_0}{2}\sqrt{\frac{2k_B T}{\pi M_{atom}}} \quad (2.11)$$

$f(v,T)$ in the equation is the Maxwellian distribution.

The Levenberg-Marquardt method is used to estimate the near-surface density n_0 and temperature T from the altitude profile by fitting with the model profile (Fig. 2.1). For Mg and Ca, because some data show an unknown sharp increase in brightness at low altitudes (gray-hatched in the Fig. 2.1a, b), possibly owing to uncorrected scattering from the bright surface, only data above 500 km for fitting are used (Fig. 2.1a, b). For Na, because it is difficult to precisely evaluate the production rate of higher-energy components owing to the low signal-to-noise ratio of the data or to the limitation of the adopted physical model as pointed out by Cassidy et al. (2015), I used only the production rate of the lower-energy component, which was ejected through the PSD (Fig. 2.1c). Near-surface density, temperature, and production rate of Mg, and temperature of Na obtained in our analysis was consistent with Fig. 8 of Merkel et al. (2017) and Fig. 8 of Cassidy et al. (2015), respectively. The results for Ca cannot be compared directly with Burger et al. (2014), since the used assumptions are different.

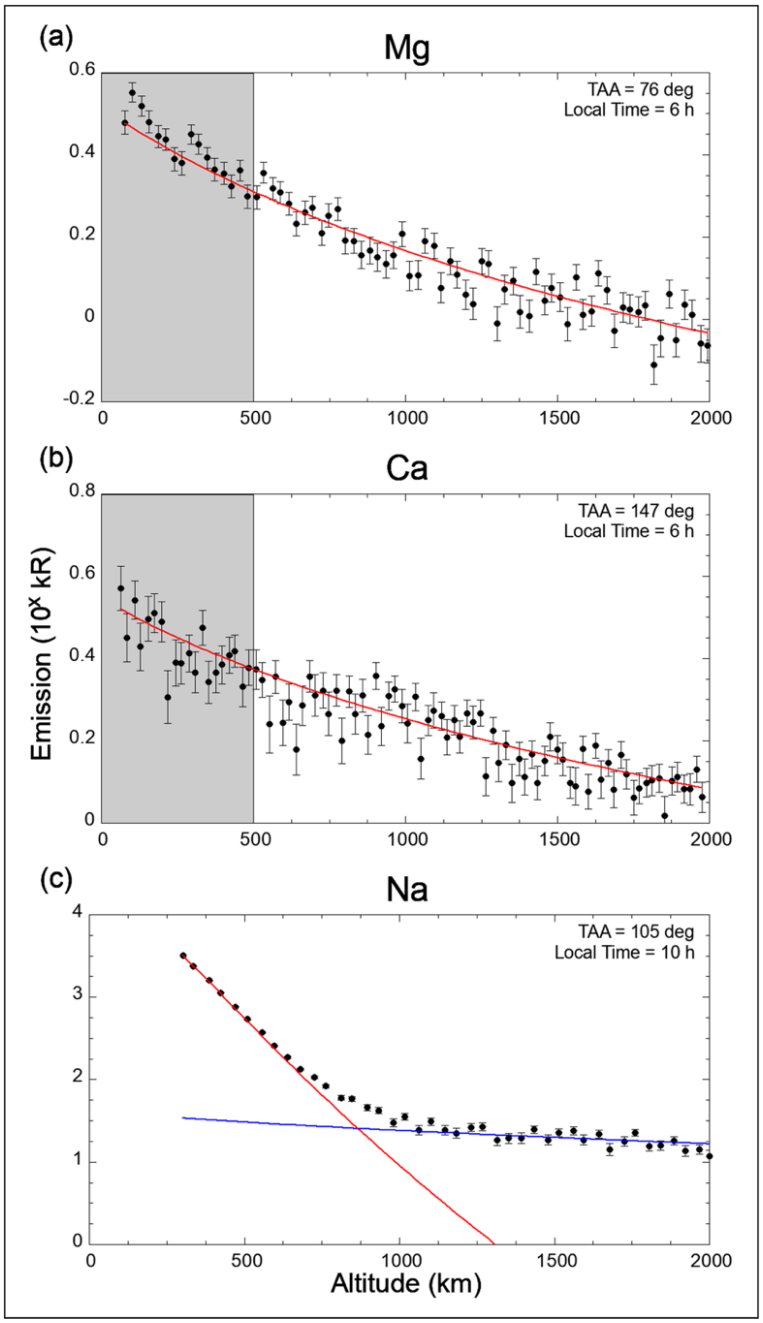

Fig. 2.1. Fitting to the altitude profile of (a) Mg, (b) Ca, and (c) Na.

For Mg and Ca, fitting was performed while ignoring the observations with a tangential altitude lower than 500 km (the gray region). The Na profile was fitted assuming two components: a lower-energy component and a higher-energy component, and only the production rate of the lower-energy component derived from PSD was used. The Levenberg-Marquardt method was used for fitting.

However, I confirmed that the order of temperature and production rate is consistent with their Fig. 6. To remove the effect of seasonal variability and local time dependence, the production rate was divided by that at the antipodal points at the same TAA, the same local time, and the different Mercury years. Then, I defined a "relative production parameter" Σ_{exos} at the tangential point longitude of ϕ, TAA of α, and local time of h as follows to remove the dependency on TAA and local time:

$$\Sigma_{exos}(\phi, \alpha, h) \equiv log_{10}\left(\frac{S(\phi, \alpha, h)}{S(\phi + \pi, \alpha, h)}\right) \quad (2.12)$$

A certain longitude comes to the same local time every other Mercury year, because of Mercury's 3:2 spin-orbit resonance. Thus, the data of $S(\phi, \alpha, h)$ and $S(\phi + \pi, \alpha, h)$ are obtained from successive Mercury years. When calculating Σ_{exos}, I averaged the production rate S obtained from the data for each local time of 2 h and a TAA of 4°. Because the seasonal variation and local time dependence is assumed as offset by the calculation shown in Equation (2.12), $\Sigma_{\mathrm{exos}}(\phi, \alpha, h)$ are expected to strongly depend on the ratio of surface abundance. Note that $\Sigma_{\mathrm{exos}}(\phi, \alpha, h) > 0$ means $S(\phi, \alpha, h) > S(\phi + \pi, \alpha, h)$, and $\Sigma_{\mathrm{exos}}(\phi, \alpha, h) = -\Sigma_{\mathrm{exos}}(\phi + \pi, \alpha, h)$. For Mg and Ca, the correlation coefficient between $\Sigma_{\mathrm{exos}}(\phi)$ and the surface Mg and Ca abundance ratio defined as $\Sigma_{\mathrm{surf}} \equiv \log_{10}\big(\sigma(\phi)/\sigma(\phi + \pi)\big)$, is calculated, where σ is the surface density of Mg and Ca around the equator. The surface density distributions of Mg and Ca (Fig. 2.2) were made through weighted average and moving average applied to observational data as was described in detail in Nittler et al. (2020). Only data at the equator were used in this study. The surface Na density in the Northern Hemisphere was presumed by Peplowski et al. (2014) based on observations by the Gamma-Ray Spectrometer (GRS) onboard MESSENGER. However, the production rate of the Na

exosphere cannot be compared to the surface Na density because the exosphere data concentrated around the equator do not spread in the latitude direction and the surface data, on the other hand, have little information in the longitudinal direction.

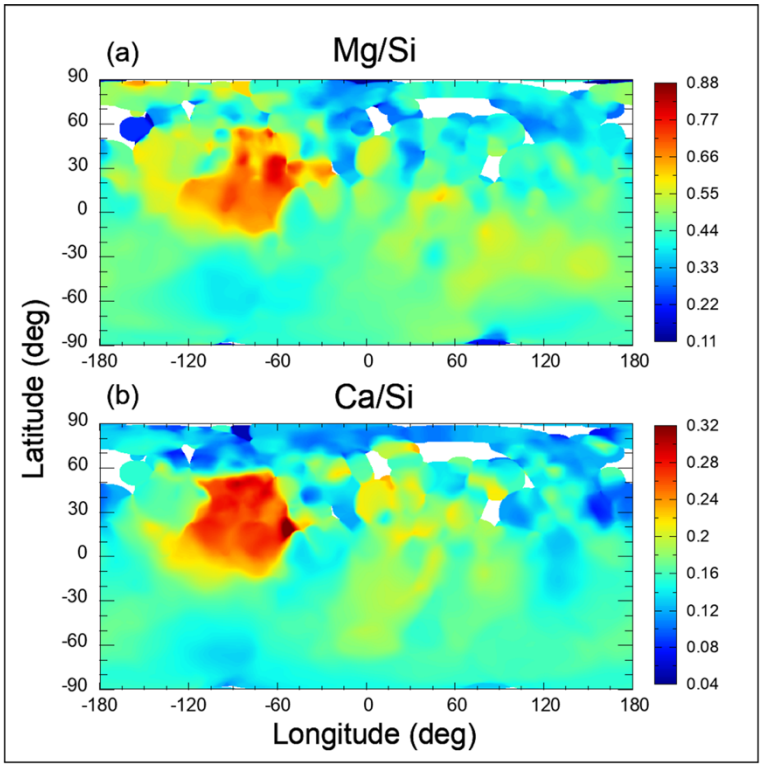

Fig. 2.2. Surface density distributions of (a) Mg and (b) Ca deduced from the observations by MESSENGER/XRS.

2.3. **Results and Discussion**

2.3.1. Mg

In Fig. 2.3a, the relative production parameters of Mg (colored dots) and the surface Mg abundance ratio at the equator (black solid line) as a function of longitude are plotted. The value of error is calculated through the propagation of error of fitting parameters, n_0 and T in Equation (2.1). In all the analyses below, including those of Ca and Na, noisy data with relative error of $S(\phi)/S(\phi+\pi)$ greater than 10% were

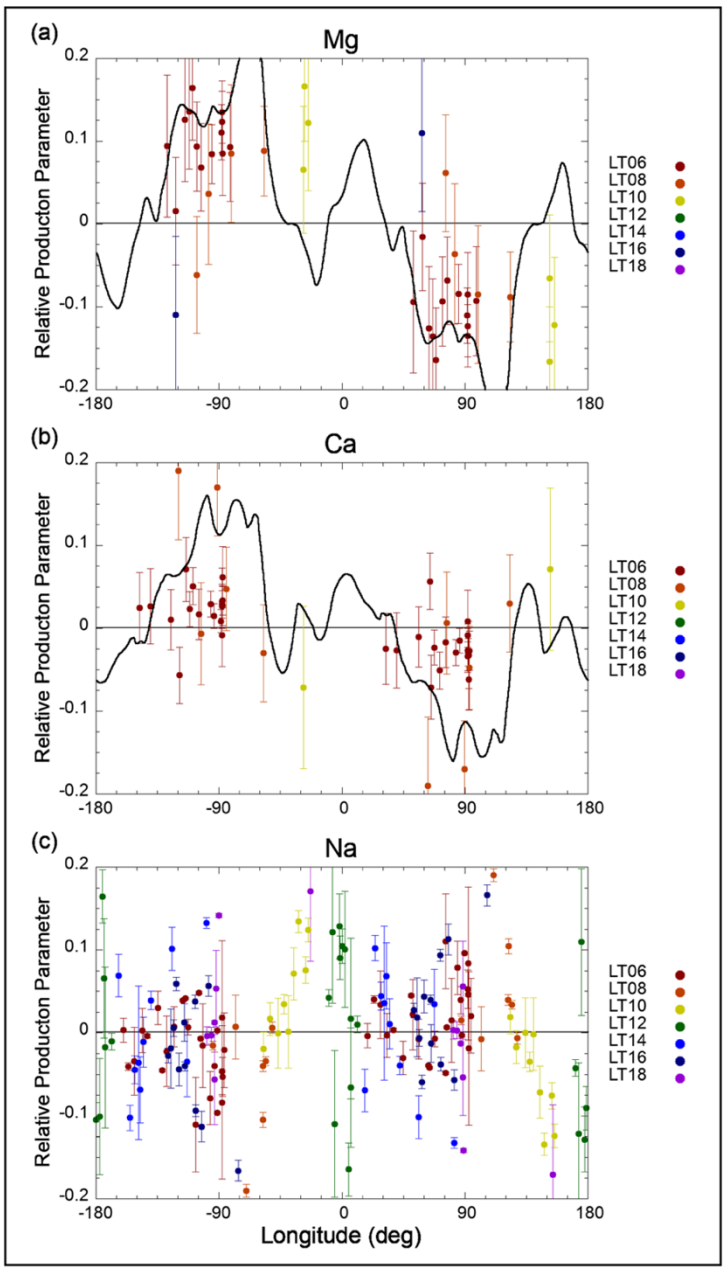

Fig. 2.3. Dependence of the relative production parameter on longitude.

Dots are the relative production parameter of the exospheric atoms, which is the common logarithm of the ratio of production rate at a certain longitude to that at an antipodal point. The dot color represents the local time at which the observations were performed. The black solid lines in (a) and (b) are, respectively, the common logarithm of surface Mg and Ca abundance ratio at a certain longitude to that at an antipodal point.

systematically removed. The correlation coefficient between the production rate ratio and surface abundance ratio was $r = 0.70 \pm 0.17$, with a 95% confidence interval of $0.65 < r < 0.76$. The amount of data used in this study was higher than that used in a previous study (Merkel et al., 2018), which only used local time 06 data. In addition, calculating the surface Mg abundance ratio in the same way as the production rate of the Mg exosphere enabled statistical tests using the correlation coefficient, which clarified the exosphere-surface correlation for Mg on Mercury. Carefully looking at Fig. 2.3a, the trend of production rate and that of surface abundance apparently disagree at local time 10. Production rate due to MIV is smaller at local time 10 than at local time 06 and 08 (Merkel et al., 2017). Since Mg ejected at local time 06 and 08 is included in the exosphere at local time 10 due to diffusion, the effect of the enhancement around -80°E is probably appeared also in the exosphere at local time 10.

2.3.2. Ca

The relative production parameters of Ca (colored dots) and the surface Ca abundance ratio at the equator (solid black line) as a function of longitude are plotted in Fig. 2.3b. The correlation coefficient between the production rate ratio and surface abundance ratio was $r = 0.22 \pm 0.14$, with a 95% confidence interval of $0.12 < r < 0.32$. This result indicates that the exosphere-surface correlation of Ca is weaker than that of Mg.

The difference between these results attributes to the difference of their g-factor. Because solar flux at emission wavelength of Ca (422.7 nm) is approximately ten times larger than that of Mg (285.2 nm), g-factor of Ca is also much larger than that of Mg. Consequently, Ca experiences more solar radiation acceleration and is more likely to

flow in the tailward direction. To confirm this difference between the two components, I performed three-dimensional Monte Carlo simulations of the trajectories of Mg and Ca atoms in the exosphere. In this model, 10,000 atoms of Mg or Ca are simultaneously ejected only once from 280°E (red arrow in Fig. 2.4), where Mg and Ca are concentrated. Ejected atoms move due to the gravity of Mercury and the sun and solar radiation pressure. The g-factor is set as a function of the radial velocity with respect to the Sun considering the Doppler shift. Mercury is assumed at the perihelion, or TAA = 0°. Fig. 2.4 shows the line-of-sight column density of Mg and Ca atoms in 60 minutes after ejection, seen from the south pole as well as the observations by the MASCS. Note that these results do not match observations, since atoms were ejected only once and

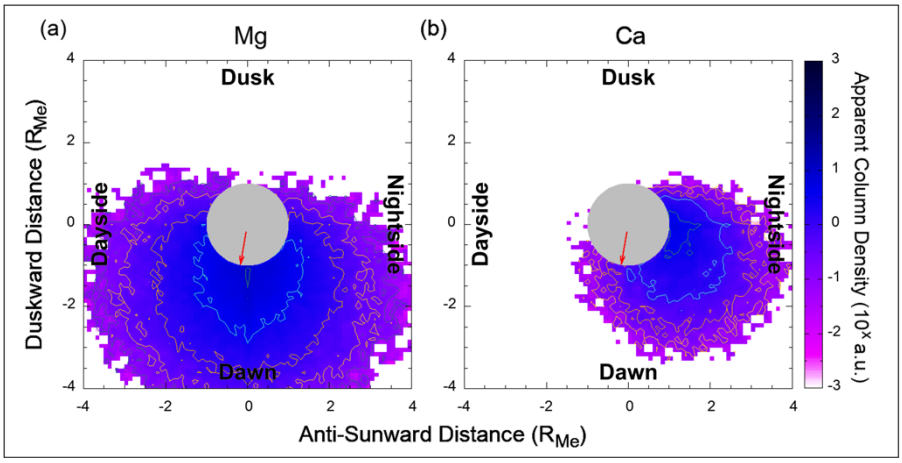

Fig. 2.4. Trajectories of Mg and Ca atoms seen from the south pole using test particle simulations at perihelion.

The color scale, which is displayed on a logarithmic scale, corresponds to the line-of-sight integration of the amount of the exosphere seen from the south pole as well as the observations by the MASCS. Note that the absolute value of the color scale does not have physical meaning. It can be seen that Ca tends to flow in the anti-sunward direction, unlike Mg. Note that these results do not match observations, since atoms were ejected only once and only from the single point.

only from the single point to describe the difference of behavior of Mg and Ca in the exosphere. Because the source of Ca has not yet been identified well, our calculation used several energies in the range of 3,000K to 40,000K. However, the qualitative results were the same as those in Fig. 2.4, which shows the case of 20,000K. These results show that information on the distribution of surface Ca is moved tailward by solar radiation. This makes the exosphere-surface correlation computationally smaller because our method using the Chamberlain model ignores horizontal transport when estimating the production rate.

2.3.3. Na

The relative production parameter of Na (colored dots) as a function of longitude is shown in Fig. 2.3c. Because Na has a larger amount of data with higher S/N ratio thanks to its brightness, the data with relative error of $S(\phi)/S(\phi+\pi)$ less than 5% will be exclusively used instead of 10% (Fig. 2.5a). The relative production parameter Σ_{exos} is close to 0 at most longitudes, but we can see $\Sigma_{\mathrm{exos}} > 0$ in the region from $-45°$E to $0°$E (red box in Fig. 2.5a). Note again that $\Sigma_{\mathrm{exos}}(\phi) > 0$ means that the production rate at the longitude of ϕ (e.g., $-45°$E) is larger than that at the oppsite side whose longitude is $\phi \pm \pi$ (e.g., $135°$E). The region from $-45°$E to $0°$E has an especially high maximum temperature of 650 K at the perihelion. Extracting regions whose surface temperature when the data were collected was high (> 550 K), we found that $\Sigma_{\mathrm{exos}} > 0$ in the region from $-45°$E to $45°$E (red box in Fig. 2.5b), which also means that $\Sigma_{\mathrm{exos}} < 0$ in the region from $135°$E to $-135°$E.

The cause of $\Sigma_{\mathrm{exos}} > 0$ in the region from $-45°$E to $45°$E can be explained well by assuming two forms of Na binding to the surface: physisorption and chemisorption.

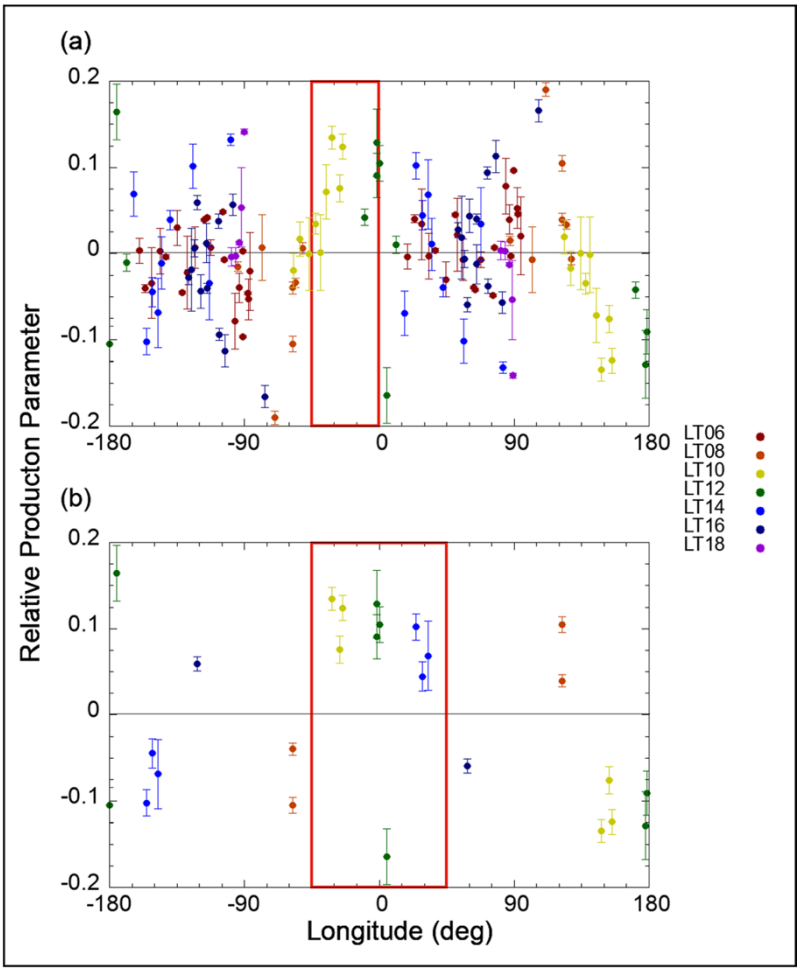

Fig. 2.5. Dependence of the Na relative production parameter on longitudes. (a) Data with relative error of $S(\phi)/S(\phi+\pi)$ is less than 5% are plotted. (b) Data with relative error of $S(\phi)/S(\phi+\pi)$ is less than 5% and with temperature above 550 K are plotted. The color of each dot represents the local time when the observations were performed.

Similar ideas have often been assumed in Na exosphere models, such as proposed by Leblanc and Johnson (2010). Most of the physisorbed components are composed of Na atoms that re-impacted the surface. Because they are easily ejected through thermal desorption as their binding energy is less than 2.0 eV, the distribution mainly corresponds to the surface temperature. In contrast, the binding energy of chemisorbed Na atoms is ranging from 2.6 eV on sodium orthosilicate to 7.9 eV on albite (Morrissey

et al., 2022), which implies that chemisorbed Na is distributed depending not only on surface temperature but also on geological features.

A possible scenario is as follows (Fig. 2.6): when the surface temperature is intermediate (lower than approximately 500 K), the thermal accommodation layer,

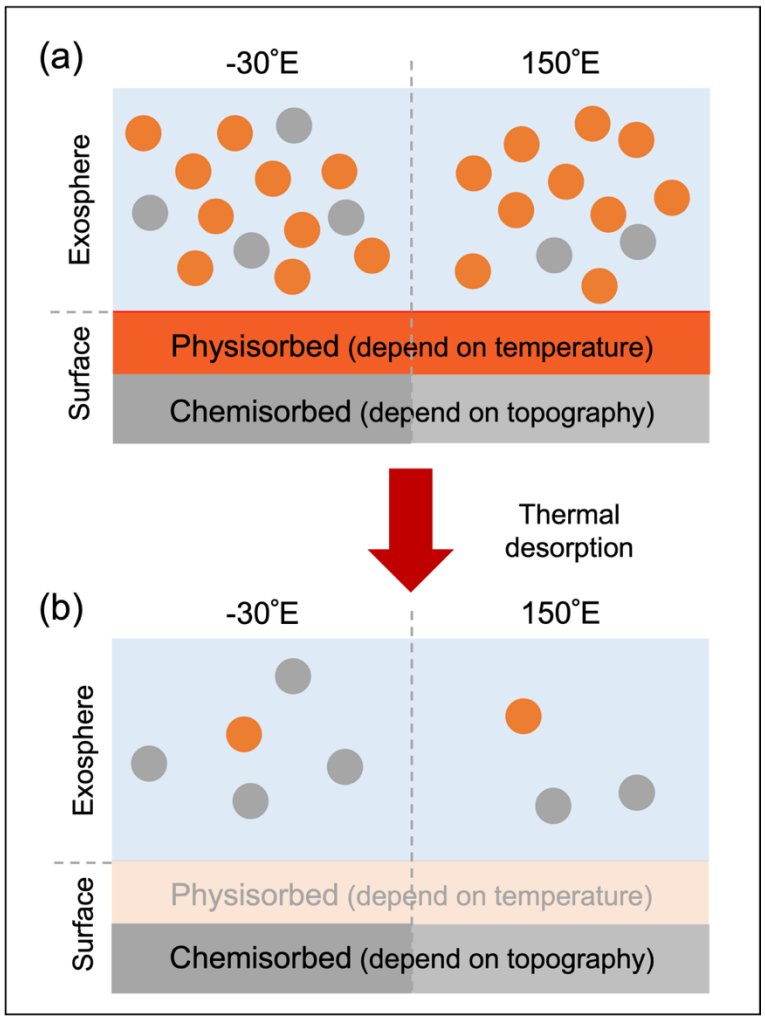

Fig. 2.6. A two-layer scenario of the surface Na.

(a) At the intermediate temperature of about 500 K, the exosphere mainly consists of physisorbed Na atoms. (b) When the surface temperature rises, the physisorbed Na layer is depleted, and chemisorbed Na atoms populate the exosphere. Thus, correlation is considered to appear in the regions with extremely high-temperature.

which is composed of physisorbed atoms, is not depleted and most of the produced Na exosphere is derived from the physisorbed component. Therefore, the production rate of the exosphere depends mainly on the surface temperature and UV flux. However, in the high-temperature region above 550 K, such as around 0°E (Fig. 2.7; based on Killen et al., 2004), physisorbed Na atoms are depleted by thermal desorption, and most of the ejected Na is occupied by chemisorbed atoms. Thus, the production rate of the exosphere begins to depend on geological features; that is, an exosphere-surface correlation appears in the high-temperature regions from $-45°$E to $45°$E (and from $135°$E to $-135°$E). Parameters related to thermal desorption, such as binding energy and oscillation frequency, have not been determined well: Hunten and Sprague (2002) adopted 1.4 eV and 10^{13} Hz, Leblanc and Johnson (2010) used a Gaussian distribution between 1.4 and 2.7 eV with a most probable value of 1.85 eV and 10^{9}-10^{11} Hz, Suzuki

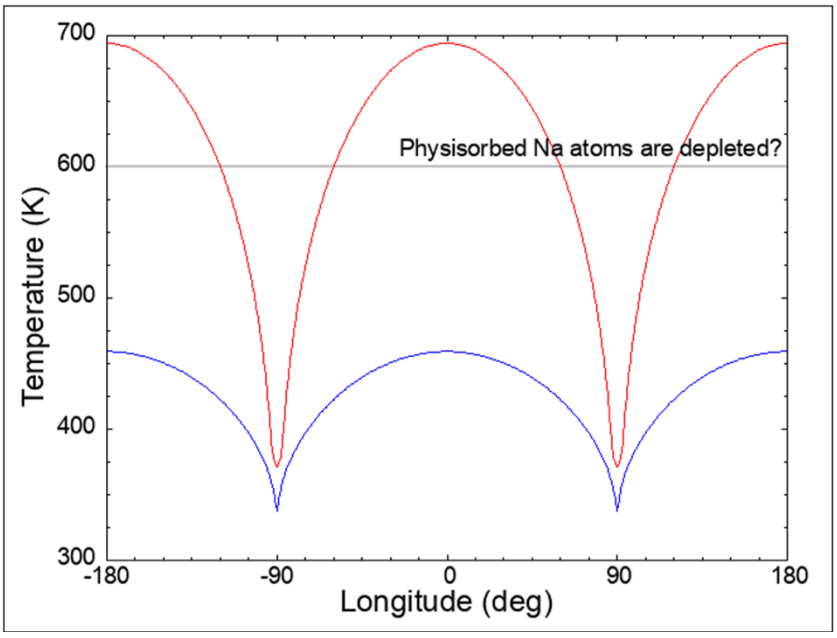

Fig. 2.7. The surface temperature experienced by each longitude.
The red line shows the maximum temperature, and the blue line shows the average temperature which each region experiences during Mercury's revolution.

et al. (2020) assumed 1.85 eV and 10^{13} Hz (Fig. 2.8), and Sarantos and Tsavachidis (2020) demonstrated that diffusion makes the energy barrier of the desorption higher. It typically takes approximately 10 minutes for the thermally desorbed atoms to re-impact the surface. If the binding energy is less than 1.85 eV and oscillation frequency is larger than 10^{13} Hz, the desorption rate per 10 minutes reaches nearly 100% in regions with temperatures above 550 K, which is consistent with our results. Note that the regions with larger production rates do not always correspond to surface composition anomalies, because the solar radiation acceleration of Na is even larger than that of Ca. In addition, the composition anomaly of the chemisorbed component does not always reflect the geological history of Mercury, as it also gradually varies through repeated thermal desorption.

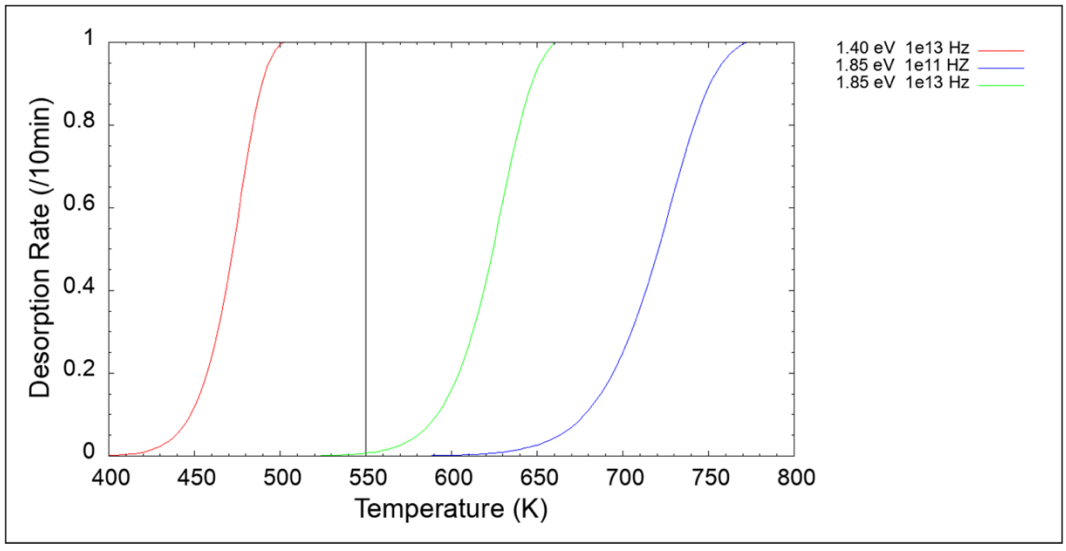

Fig. 2.8. Parameter dependence of the thermal desorption rate.

The red and green lines use parameter sets adopted by Hunten and Sprague (2002) and Suzuki et al., (2020), respectively. The blue line uses parameters assumed as the most probable values by Leblanc and Johnson (2010). Each line represents the proportion of thermally desorbed Na from the surface.

2.4. **Implications for Other Components**

From the discussion above, low volatility and low solar radiation acceleration are important factors for the exosphere-surface correlation. The solar radiation acceleration and photoionization lifetimes of some components of Mercury's exosphere are listed in Table. 2.1. The solar radiation acceleration of the atoms was calculated using the following equation:

$$b = \frac{1}{m_{atom}} \sum_i \frac{h}{\lambda_i} g_i \qquad (2.13)$$

where $m_{\mathrm{atom}}, h, \lambda_i,$ and g_i are the mass of atoms, Planck constant, wavelength of each emission line, and g-factor, respectively. The g-factor at rest and at 1 au was calculated using values from Killen et al. (2009).

Additionally, a long photoionization lifetime may be important, although this was not observed in this study. For reference, the photoionization lifetimes derived from Fulle et al. (2007) are also shown in Table. 2.1. Atoms with short photoionization lifetimes, such as aluminum, undergo photoionization and reneutralization in a short time. The distribution of exospheric atoms drastically changes during ionization due to the electromagnetic field, which weakens the exosphere-surface correlation. The same analysis as that in this study is required for species with short photoionization lifetimes.

Considering the constants in Table. 2.1, oxygen and sulfur, with small solar radiation acceleration, are expected to have an exosphere-surface correlation on Mercury. Because Na and K are more easily thermally desorbed, little exosphere-surface correlation will be observed for Mercury. However, it has been reported that the amount of Na in the Moon's exosphere increases above the low-albedo regions (Colaprete et al., 2016) and that of K is enhanced above the KREEP regions

(Rosborough et al., 2019). In cooler celestial bodies far from the central star, atoms with higher volatility and with larger solar radiation acceleration, may have correlation. For exoplanets orbiting stars of different stellar types, atomic species exhibiting exosphere–surface correlation may change because their magnitudes of stellar radiation acceleration change.

Component	Solar radiation acceleration @1 au (m/s^2)	Photoionization lifetime @1 au (s)	Exosphere-surface correlation on Mercury
Na	2.5×10^{-2}	1.9×10^{5}	Little?
K	2.1×10^{-4}	4.3×10^{4}	Little?
Mg	1.9×10^{-3}	2.1×10^{6}	Strong
Ca	1.3×10^{-2}	1.4×10^{4}	Weak
O*	2.5×10^{-6}	2.0×10^{6}	Strong?
S*	4.4×10^{-6}	4.2×10^{5}	Strong?

Table. 2.1. Solar radiation acceleration and photoionization lifetime of each atom at 1 au.

* Note that neutral oxygen and sulfur were not observed by MESSENGER.

2.5. **Summary**

In celestial bodies with thin atmospheres, atoms are supplied from the surface to the exosphere owing to the effects of the space environment, such as heating, UV radiation, and the impact of micrometeoroids. Thus, the spatial distribution of some components in the exosphere is expected to reflect the distribution of each component on the surface, as well as geological features, such as craters and volcanic terrains. In this study, the existence of an exosphere-surface correlation on Mercury is verified using observations by MASCS and XRS onboard MESSENGER. As a result, it is clearly shown that Mg has a strong correlation, as suggested by Merkel et al. (2018), and Ca has a weak

correlation. As solar flux at the emission wavelength of Ca is much larger than that of Mg, g-factor of Ca is also larger than that of Mg. Therefore, I attributed this weak correlation of Ca to effective tailward transportation by larger solar radiation acceleration. Although Na atoms are easily desorbed thermally, it is possible that a exospheric nonuniformity due to the surface abundance anomaly appears in the high-temperature regions owing to the rapid depletion of the physisorbed Na layer on the surface. However, exosphere–surface correlation may not be detected even in the high-temperature regions due to large solar radiation acceleration. Based on these results, volatility and solar radiation acceleration are consider to control the correlation. S and O may also have an exosphere-surface correlation on Mercury, and it is expected that this correlation will be found in various components on cooler celestial bodies such as Europa and Ganymede. For example, Na exosphere of Europa may reflect the surface abundance distribution of NaCl supplied from the ocean underneath its surface. For exoplanets, species exhibiting the exosphere–surface correlation also differ depending on the stellar type of their host stars.

The presence or absence of correlation is a very interesting and useful issue, but there has not been enough observational data to discuss this. I hope that observations by the BepiColombo will allow us to discuss this issue in more detail. This will provide us with insights into the latitudinal direction — we could only discuss the distribution in the longitudinal direction in this study. The MSASI (Yoshikawa et al., 2010) onboard the Mio spacecraft provides a detailed structure of the Na exosphere. PHEBUS (Quémerais et al., 2020) and the Search for Exospheric Refilling and Emitted Natural Abundances (SERENA: Orsini et al., 2021) onboard the MPO spacecraft will clarify the distribution of various components in the exosphere while the Mercury Radiometer and

Thermal infrared Imaging Spectrometer (MERTIS: Hiesinger et al., 2020) onboard the MPO will reveal a wide range of surface material distributions on Mercury.

3. Estimation of Water Production Rate and Active Fraction of Long-Period Comets

Observation of comae is one of the important means to understand the chemical properties of comets. In particular, production rate ratios of various volatile molecules to those of water have been used to assume thermal history, redox environment during formation and ice-to-dust ratio of comets (e.g., Ootsubo et al., 2012; Russo et al., 2016). Moreover, estimation of water production rate is important for understanding the cometary activity, since most of ejected gas from nuclei are water molecules within the heliocentric distance of approximately 2.5 au. In this chapter, I focus hydrogen atoms dissociated from water molecules. Hydrogen atoms are generally more spread out than water molecules and it is expected that water production rates can be evaluated without being affected by complicated environments of inner comae especially for hyper-active comets. Besides, hydrogen comae are so bright and expanded that they can also be observed by small telescopes with severe restrictions onboard spacecraft such as CI. In expanding discussion to various planetary bodies in the future, the optimal species for observations may differ depending on targets. It is essential to prepare various observation means for comprehensive observations.

In this chapter, water production rates of four long-period comets are estimated using observational data of the Hisaki satellite. Furthermore, active fraction, an index of activity, is calculated from deduced water production rate. In Section 3.1, the Hisaki satellite and EXCEED onboard it are introduced. The method of instrument calibration is described in Section 3.2. Subsequently, the method used for estimating the water production rate and active areas of comets is presented in Sections 3.3 and 3.4. In Section 3.5, results are shown and compared to the results obtained by other

instruments.

3.1. **Hisaki Satellite and EXCEED**

Hisaki is a small Japanese scientific satellite that was launched on September 14, 2013 (Tsuchiya et al., 2011; Yamazaki et al., 2014; Yoshikawa et al., 2014; Yoshioka et al., 2013). It orbits the Earth with a perigee of 954 km and an apogee of 1,157 km. EXCEED is a spectroscope used to measure the atomic and ionic emission lines between wavelengths of 52 nm and 148 nm. It has a wide field-of-view (FOV) and has been used to observe the spatial distribution of extreme UV (EUV) emissions around planets. It has also observed eight comets thus far, and four of them for which corresponding sky observation data are available were focused on in this study. Basic information of four comets' orbit and positions of comets and the Earth at the time of observations are shown in Fig. 3.1 and Table 3.1. Among the three types of slits installed in EXCEED, the middle-size slit (60 arcsec in width) was used to perform these comet observations. Fig. 3.2 shows the spectra of C/2013 US_{10} (Catalina) observed from 3:00 to 6:00 on November 28, 2015 (UTC), wherein the horizontal axis, vertical axis, and color scale denote the wavelength, viewing angle, and the number of detected photons per min, respectively. A list of the emission lines detected by Hisaki/EXCEED is presented in Table 3.2. The bright line seen around 79.6 nm in Fig. 3.2 is a ghost image of Ly-α line.

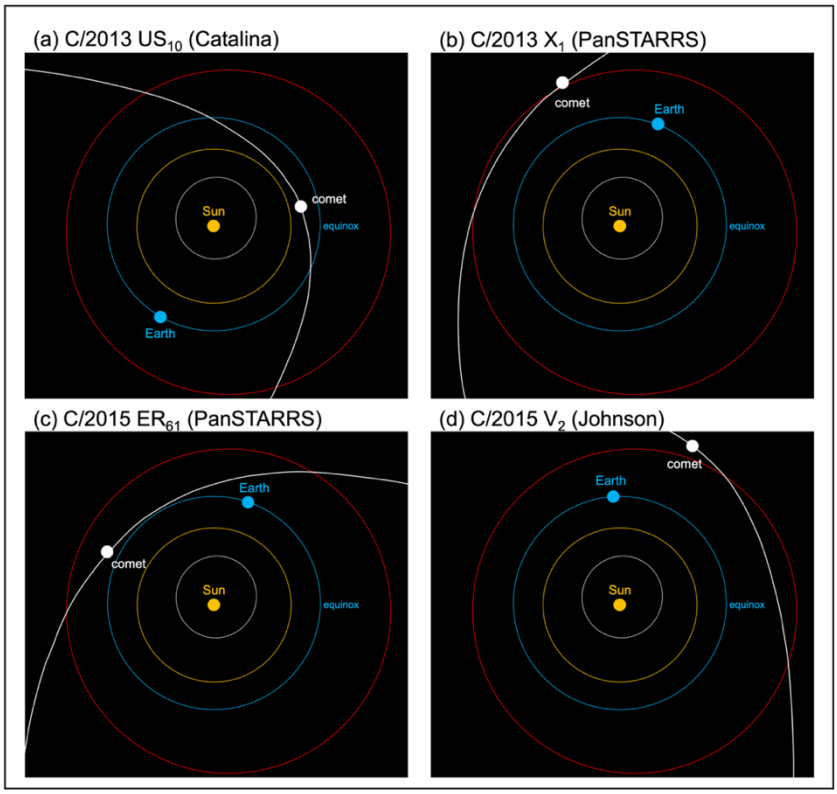

Fig. 3.1. Positions of comets and the Earth during observations.

The orange, blue, and white circles represent positions of the Sun, the Earth and comets at the time of observations. The gray, orange, blue, red, and white lines represent orbits of Mercury, Venus, the Earth, Mars and comets. The rightmost point in the Earth's orbit is the vernal equinox.

Comets	Date Passed Perihelion	q (au)	Observation Period	r_H (au)	r_G (au)
C/2013 US_{10} (Catalina)	11/15/2015	0.823	11/22/2015 – 12/02/2015	0.829 – 0.884	1.50 - 1.69
C/2013 X_1 (PanSTARRS)	04/20/2016	1.31	05/30/2016 – 06/02/2016	1.44 – 1.46	0.910 - 1.01
C/2015 ER_{61} (PanSTARRS)	05/09/2017	1.04	06/02/2017 – 06/03/2017	1.11 – 1.12	1.38 - 1.40
C/2015 V_2 (Johnson)	06/12/2017	1.64	06/25/2017	1.65	0.892 - 0.901

Table 3.1. Orbit information of observed four comets.

q denotes perihelion distance. r_H and r_G denote heliocentric distance and geocentric distance of comets at the time of observations.

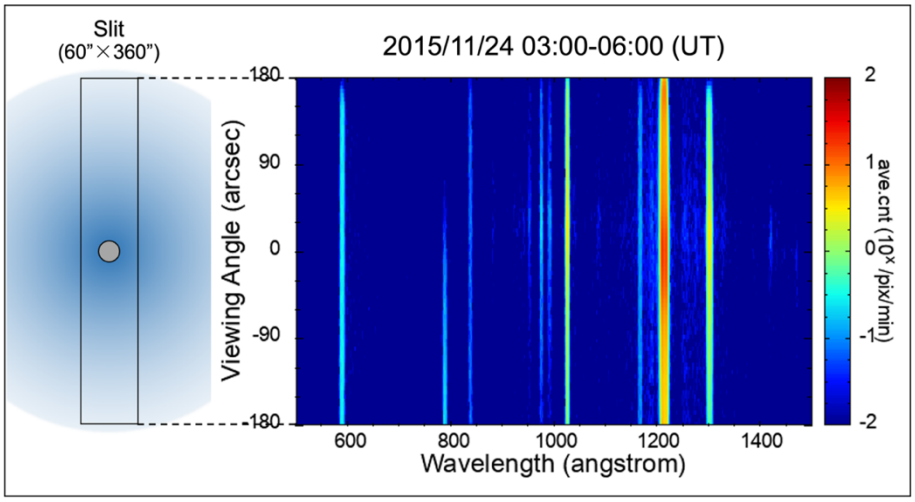

Fig. 3.2. An example of the data obtained by Hisaki/EXCEED.

The horizontal axis donates the wavelength, vertical axis donates the viewing angle, and the color scale represents the number of detected photon (logarithmic scale). The 1-dimensional spatial distribution of the radiance of emission lines such as Ly-α can be observed. The bright line seen around 79.6 nm is a ghost image of Ly-α line.

Wavelength (nm)	Atom	Wavelength (nm)	Atom
58.4	He	108.8	CO, C-X
83.4	O+	116.8	N
87.8	O	121.6	H (Ly-α)
90.4	C+	127.7	C
93.8	H	130.4	O
95.0	H	132.9	C
97.3	H (Ly-γ)	133.5	C+
98.9	O	135.6	O
102.6	H (Ly-β)	142.5	S

Table 3.2. List of emission lines detected by Hisaki/EXCEED.

3.2. **Calibration of Sensitivity of the Detector Using Sky Observation Data**

In this section, a method for converting the number of detected photons into the radiance (in Rayleigh units) is described. Although standard stars are typically used for the post-launch calibrations of Hisaki, their signals are obscured by the geocorona in the wavelength range around Ly-α, wavelength of 121.6 nm (Fig. 3.3). Hence, the sky observation data are utilized for calibration, instead. Sky observation data are obtained by directing a few degree away from comets to evaluate radiance of light from sources other than comets such as geocorona and interplanetary media, and are typically used to subtract the background signals.

In the detector design, the sensitivity at wavelengths of 119–125 nm is reduced by not coating it with fluorescent material to avoid signal saturation (see Fig. 16 in Yoshioka et al., 2013). Despite that, an excessive number of photons still degrade the sensitivity over time. In contrast, the Ly-β emission is approximately 1,000 times less bright than the Ly-α emission; therefore, the sensitivity degradation is considerably lower around 102.6 nm. In fact, the Ly-α/Ly-β ratio of the sky observation data gradually decreases compared with the early data obtained in half a year after launch (Mar. 9, 2014), as shown in Fig. 3.4a. Note that Venus was observed on Mar. 9, 2014 and the data around the viewing angle of -70" (gray shaded area in Fig. 3.4a), where Venus appears, were excluded in the calibration processes. The Ly-α/Ly-β ratio can be observed to decrease and its spatial non-uniformity is more noticeable over time. The spatial non-uniformity of sensitivity is owing to the dumbbell shape of one of the slits installed in EXCEED. It was primarily employed to simultaneously observe the Jovian aurora and Io plasma torus; it has a width of 20” at the center and 140” at both ends (see Fig. 8 in Yoshioka et al., 2013). This shape allows considerably more photons to enter at

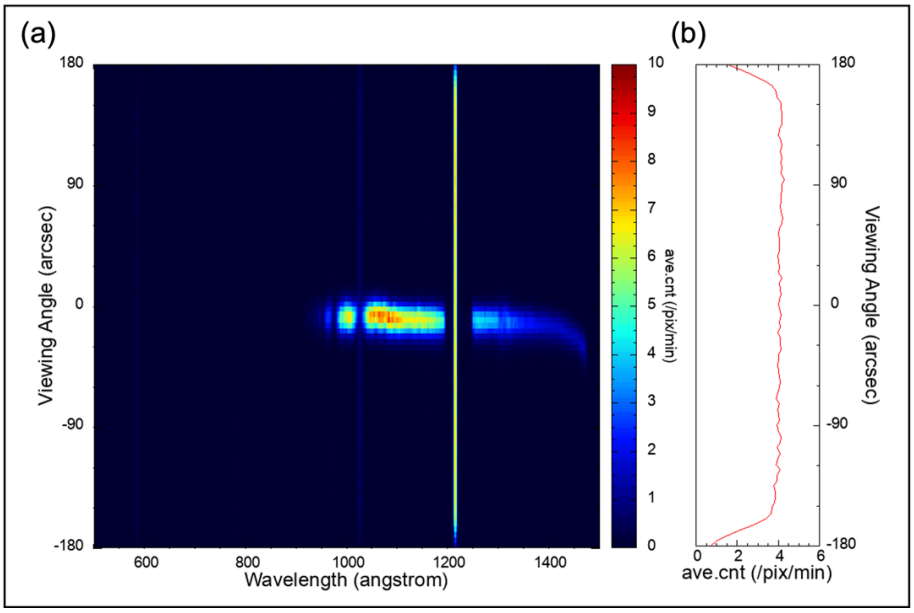

Fig. 3.3. An example of observational data of a standard star, GD71, obtained by Hisaki/EXCEED on 01/17/2014.

(a) Two-dimensional spectra, whose format is the same as Fig. 3.2. GD71 is shown around the viewing angle of 0°. (b) Distribution of the number of counts around Ly-α emission line. This is obtained by integrating of the 2D spectra in the wavelength range of 121.6±0.5 nm. Horizontal axis is counts averaged per pixel per min, and the vertical axis is the viewing angle. No obvious signals from GD71 are found.

the end region than at the center, resulting in more rapid degradation. Assuming that (1) the geocorona is spatially uniform within the small FOV of EXCEED (400") and (2) hydrogen atoms glow only because of solar resonance scattering, resulting in a long-term constant Ly-α/Ly-β ratio, the Ly-α emission sensitivity can be evaluated using the following equation:

$$p(\phi) = p_0(\phi) \times \frac{r(\phi)}{r_0(\phi)} \tag{3.1}$$

where $p, p_0, r, r_0,$ and ϕ denote the current sensitivity in count/Rayleigh, sensitivity before launch, apparent current Ly-α/Ly-β ratio of the geocorona, Ly-α/Ly-β ratio of the geocorona observed just after launch, and viewing angle, respectively. While analyzing

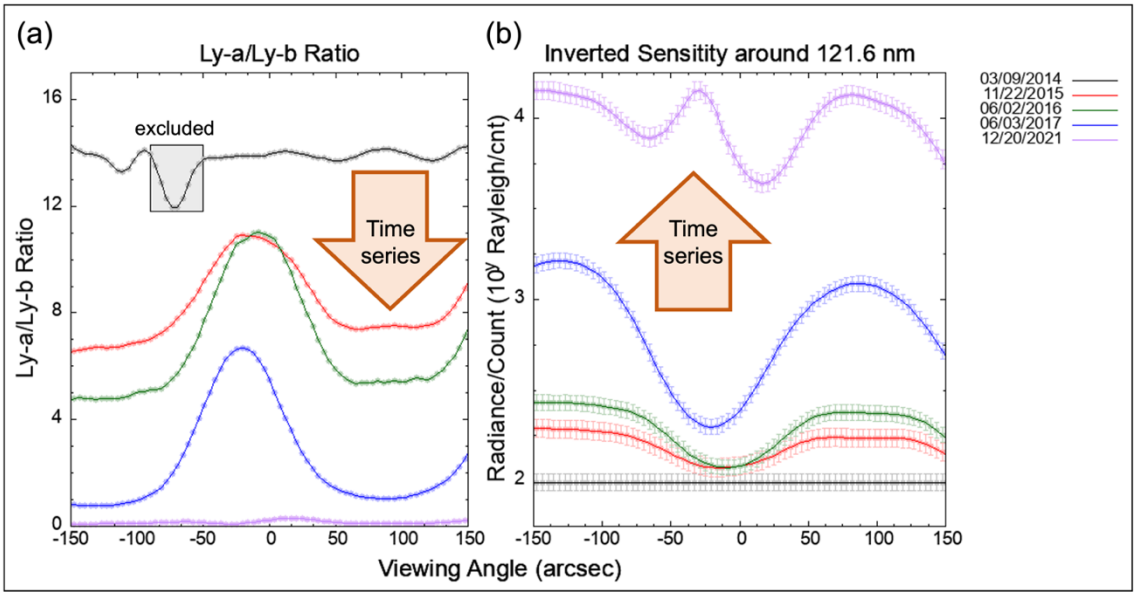

Fig. 3.4. Time variation of the observed Ly-α/Ly-β ratio of geocorona (a) and of reciprocal of sensitivity (b).

The horizontal axis represents the viewing angle, and the vertical axis in (a) represents the Ly-α/Ly-β ratio, and that in (b) represents the conversion coefficient from the number of detected photons to the radiance (logarithmic scale). The degradation and enhancement of non-uniformity can be observed. The bump in the red line in (a) around -70" (gray-shaded area) is caused by Venus appearing in the FOV, which was omitted during analysis.

the data obtained in March 9, 2014, data from -90" to -50" (gray shaded area in Fig. 3.4a) were excluded to omit the signal derived from Venus, and the sensitivity was assumed to remain uniform then. The calibrated sensitivity for Ly-α obtained in this manner is shown in Fig. 3.4b. The x-axis represents viewing angle, whereas the y-axis represents the inverse of sensitivity in Raylaigh/count on a logarithmic scale, which is equivalent to the conversion coefficient from the number of detected photons to the radiance.

3.3. **Estimation of Water Production Rates**

3.3.1. Conversion of Observational Data to Hydrogen Column Density

The spatial distributions of the Ly-α radiance around the comets were obtained after performing the calibration described in Section 3.2. Thereafter, data were integrated every 6 h for the darker comet, C/2015 V2 (Johnson) and every 3 h for the other three comets. The averaged net observation time during each period was approximately 35%. During integration, the sky observation data in wherein the local time of Hisaki was close to each data point were subtracted to cancel the signal derived from the geocorona.

As comets' nuclei cannot be observed directly by EXCEED, the viewing angle was converted into the altitude (impact parameter), assuming that the brightest pixel contained the nuclei. The apparent column density along the line of sight was obtained by dividing the radiance by the g-factor, which is the glow efficiency, under the optically thin condition. In calculating g-factor, oscillator strength listed in NIST Atomic Spectra Database Lines Form (https://physics.nist.gov/PhysRefData/ASD/lines_form.html) was used and solar flux was calculated by combining time series data of total Ly-α line flux listed in Composite Solar Lyman-alpha (https://lasp.colorado.edu/lisird/data/composite_lyman_alpha/) and equation expressing the shape of solar Ly-α spectra (equations 8 to 11 of Kowalaska-Leszczynska et al. (2018) with updated model parameters in Kowalaska-Leszczynska et al., 2020: Fig. 3.5). Swings effect, variation of g-factor due to Doppler effect arising from the relative velocity between the Sun and comets, was considered, but Greenstein effect, variation of g-factor due to Doppler effect arising from each atom in comae was ignored since it only changes g-factor by less than 1.5% (see Appendix 3.A1). The deduced column density profile for C/2013

US10 (Catalina) is shown in Fig. 3.6.

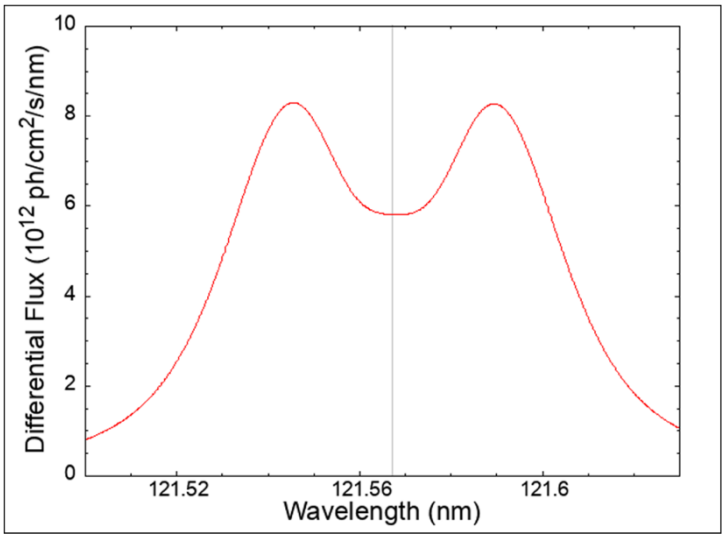

Fig. 3.5. Calculated solar spectra assuming the period of the observation of C/2013 US_{10} (Catalina) on November 22, 2015.

Due to the emission and self-absorption of solar atmosphere, two peaks are appeared in the spectra around 121.567 nm.

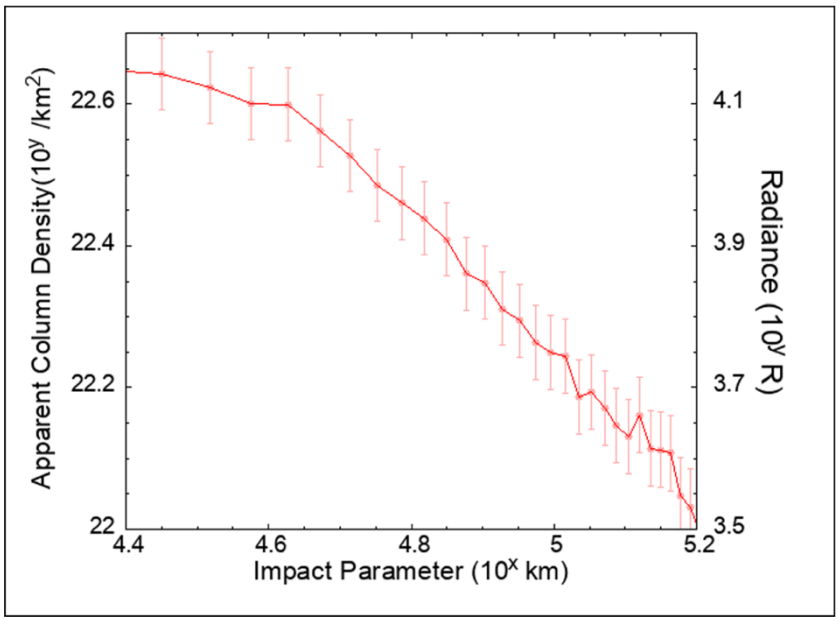

Fig. 3.6. Hydrogen column density profile (y1 axis) and Ly-α radiance profile (y2 axis) of C/2013 US_{10} (Catalina) obtained from 3:00 to 6:00 on November 28, 2015 (UTC).

3.3.2. Calculation of Water Production Rate Using One-dimensional Column Density Profile

To estimate the water production rate from the apparent column density profile, I used line of sight integration of the following three generation analytical model of the H_2O-OH-H system adopted by Kaneda et al. (1986), which was introduced in Subsection 1.3.4.3:

$$n(t,r) = \frac{Q_{H_2O\to H}\left(t - \frac{r}{v_{H_2O\to H}}\right)}{4\pi r^2 v_{H_2O\to H}} e^{-\frac{r}{\tau_H v_{H_2O\to H}}} + \frac{Q_{OH\to H}\left(t - \frac{r}{v_{OH\to H}}\right)}{4\pi r^2 v_{OH\to H}} e^{-\frac{r}{\tau_H v_{OH\to H}}} \quad (3.2)$$

I adopted $\tau_{H_2O} = 27$ h, $\tau_{OH} = 23$ h, $\tau_H = 159$ d at the heliocentric distance of 1 au following the database of Photo Ionization/Dissociation RATES ((https://phidrates.space.swri.edu/), and $v_{H_2O\to H} = 20$ km/s, and $v_{OH\to H} = 8$ km/s following Kaneda et al. (1986). Q_{H_2O} is assumed to be constant during the integration time. Q_{H_2O} and t are free parameters in Equation (3.2). However, since hydrogen number density at the altitude of r ($\ll v_{OH\to H}\, t$) does not depend on t, I fixed $t = 10$ day and focused only on Q_{H_2O} hereafter. An example of the results of fitting the analytical model to observational data is shown in Fig. 3.7. The observed Ly-α radiance profile has obvious bends around $10^{4.7}$ km, $10^{4.5}$ km, $10^{4.3}$ km, and $10^{4.3}$ km for comet Catalina, C/2013 X_1 (PanSTARRS), C/2015 ER_{61} (PanSTARRS), and C/2015 V_2 (Johnson), respectively. It is assumed that the altitude profile below the bend is formed owing to mixture of the following effects: blur owing to lower spatial resolution, motions of H_2O and OH molecules, multiple scattering, and intermolecular collisions, which will be discussed in Chapter 4. In this study, only on the area above the bend was focused to estimate the water production rate, as these effects do not explicitly affect the distribution there.

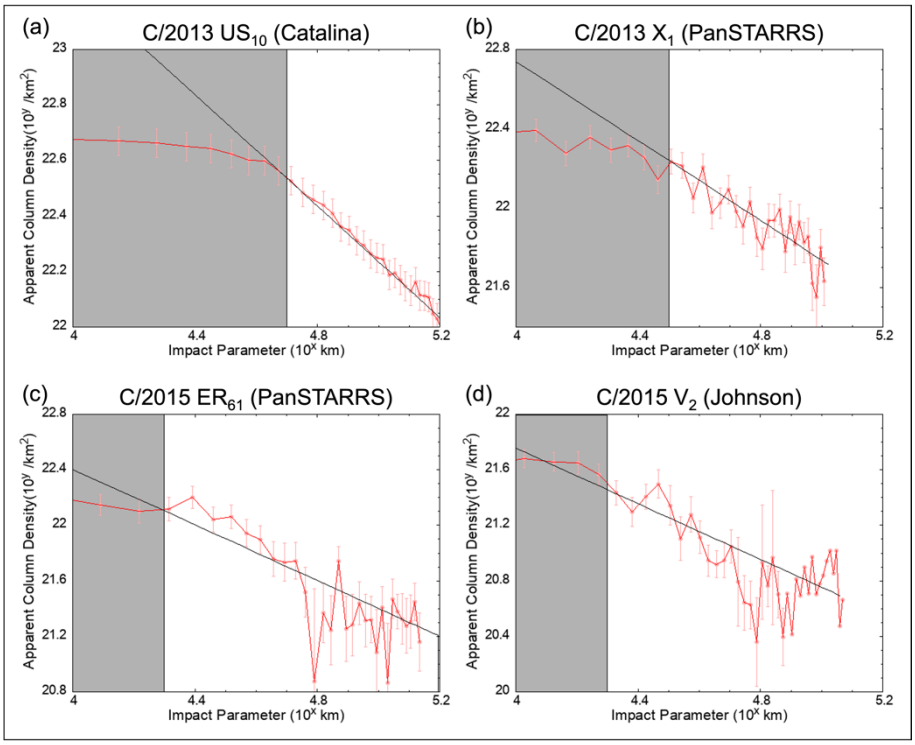

Fig. 3.7. Comparison of hydrogen column density profiles deduced from observations and from model.

Red lines represent hydrogen column density profiles and black lines represent calculated profile using Equation (3.2) (both logarithmic scale). The gray-shaded areas are excluded from fitting.

3.4. **Estimation of Active Area and Active Fraction**

Active area is the estimated area of active regions on the nucleus surface, which is the ratio of the water production rate obtained from observations and water sublimation rate per unit area expected from the radiation equilibrium temperature (Lis et al., 2019).

As described in Subsection 1.3.2.1, radiation equilibrium temperature and expected sublimation rate are calculated using sublimation model of Cowan & A'Hearn (1979):

$$F_0 r_H^{-2}(1 - A_V)\,\overline{cos\,\theta} = (1 - A_{IR})\sigma T^4 + L(T)Z(T) \qquad (3.3)$$

T is radiation equilibrium temperature of the surface, which is variable. A_V, A_{IR} and $\overline{\cos\theta}$ are set to be 0.04, 1 and 0.25 following Lis et al. (2019). $L(T)$ is latent heat of

sublimation of water-ice, empirically expressed as

$$L(T) = 12420 - 4.8T\ [cal/mol] \tag{3.4}$$

$Z(T)$ is expected sublimation rate per unit surface, which is calculated by

$$Z(T) = \frac{p(T)}{m}\sqrt{\frac{m}{2\pi k_B T}} \tag{3.5}$$

where m and k_B are mass of water molecular and Boltzmann constant. $p(T)$ is saturated water vapor pressure, empirically calculated using the following equation (Washburn, 1928):

$$log_{10}\{p(T)\ [mmHg]\} = -\frac{2445.5646}{T} + 8.2312\, log_{10}\, T - 0.01677006T \tag{3.6}$$

Calculated equilibrium temperature is shown as a function of heliocentric distance in Fig. 3.8, when solar constant $F_0 = 1.37 \times 10^3\ \mathrm{W/m^2}$. Temperature of the surface ice is assumed to be uniform due to the small thermal inertia of comets.

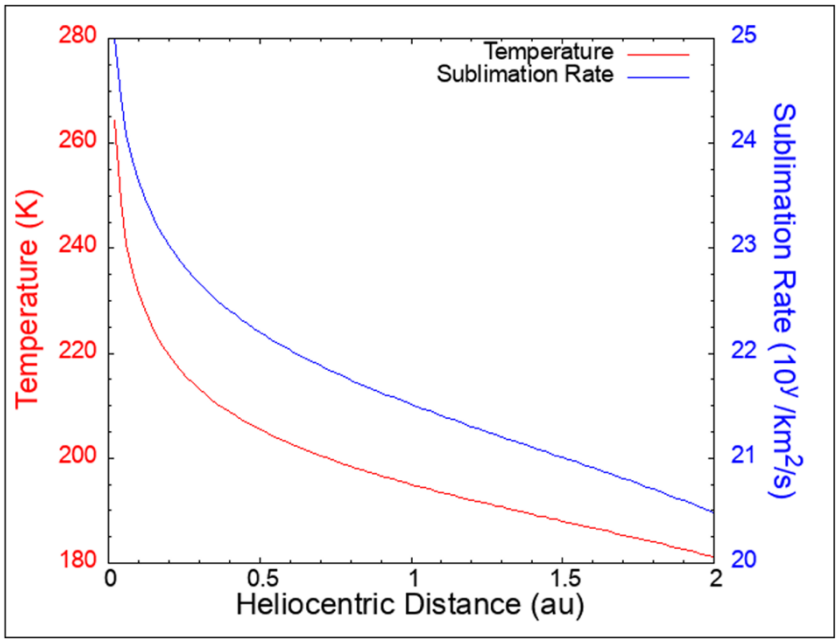

Fig. 3.8. Calculated surface equilibrium temperature (red line) and sublimation rate per unit surface (blue line) as a function of heliocentric distance.

Active fraction is the ratio of the active area to the total nucleus' surface area. In calculating surface areas of nuclei, effective radii obtained in Paradowski (2020) were used. Since nucleus size of C/2013 X_1 (PanSTARRS) has not been identified, its active fraction could not be estimated.

3.5. **Results and Comparison with Other Observations**

The results obtained in this study are summarized in Table 3.3 and discussed in order below.

3.5.1. C/2013 US_{10} (Catalina)

C/2013 US_{10} (Catalina) is a long-period comet with a perihelion distance of 0.82 au and original semi-major axis of 1.4×10^4 au according to the database provided by the Minor Planet Center (http://www.minorplanetcenter.net/db_search/). Hisaki observed it from November 22, 2015 (r_H = 0.83 au) to December 2, 2015 (r_H = 0.88 au), soon after its perihelion passage on November 15, 2015 (r_H = 0.82 au). r_H denotes the heliocentric distance. The mean water production rate during the observations was $(4.8 \pm 0.2) \times 10^{28}$ /s. This comet has also been observed by the SWAN camera onboard SOHO using UV light. The estimated water production rate from SWAN observations was $(1.94 \pm 0.06) \times 10^{29}$ /s at r_H = 0.87 au (Combi et al., 2018), which is approximately four times the production rate estimated in this study. Surface equilibrium temperature and expected sublimation rate per unit surface are approximately 198 K and 5.1×10^{27} /km^2/s, and nucleus size was estimated to be 1.65 km (Paradowski, 2020). Thus, active area and active fraction can be calculated to be 8.8 ± 0.1 km^2 and 25.8 ± 0.4%, respectively.

Comets	Observation Period	r_H (au)	Q_{H2O} (/s)	Active Area (km^2)	Active Fraction (%)
C/2013 US10 (Catalina)	11/22/2015 – 12/02/2015	0.829 – 0.884	$(4.8\pm0.2) \times 10^{28}$	8.8±0.1	25.8±0.4
C/2013 X1 (PanSTARRS)	05/30/2016 – 06/02/2016	1.44 – 1.46	$(6.9\pm0.7) \times 10^{27}$	7.4±0.6	---
C/2015 ER61 (PanSTARRS)	06/02/2017 – 06/03/2017	1.11 – 1.12	$(4.3\pm0.6) \times 10^{27}$	1.8±0.4	16.7±0.3
C/2015 V2 (Johnson)	06/25/2017	1.65	$(1.4\pm0.3) \times 10^{27}$	1.9±0.4	5.3±1.1

Table 3.3. Summary of the results of this study.

r_H denotes heliocentric distance and Q_{H2O} denotes the estimated water production rate.

3.5.2. C/2013 X_1 (PanSTARRS)

The perihelion distance and original semi-major axis of C/2013 X_1 (PanSTARRS) are 1.31 au and 4.5×10^3 au, respectively. It was observed from May 30, 2016 (r_H = 1.44 au) to June 2, 2016 (r_H = 1.46 au), soon after it passed its perihelion on April 20, 2016 (r_H = 1.31 au). The estimated mean water production rate was $(6.9 \pm 0.7) \times 10^{27}$ /s. This is less than tenth part of that estimated from SWAN observations, which estimated it to be $(1.09 \pm 0.07) \times 10^{29}$ /s at r_H = 1.45 au after perihelion passage (Combi et al., 2018). Surface equilibrium temperature and expected sublimation rate per unit surface are approximately 189 K and 1.1×10^{27} /km^2/s. Thus, active area is calculated to be 7.4 ± 0.6 km^2. Since nuclear size is unknown, active fraction cannot be identified.

3.5.3. C/2015 ER_{61} (PanSTARRS)

The perihelion distance and original semi-major axis of the long-period comet C/2015 ER_{61} (PanSTARRS) are 1.04 au and 7.0×10^2 au, respectively. It should be noted that a steep brightening of this comet was observed of on April 4, 2017 (see for example, Sekanina 2017). We observed it from June 2, 2017 (r_H = 1.11 au) to June 3, 2017 (r_H = 1.12 au). The estimated mean water production rate was $(4.3 \pm 0.6) \times 10^{27}$ /s. Surface equilibrium temperature and expected sublimation rate per unit surface are approximately 193 K and 2.4×10^{27} /km^2/s, and nucleus size was estimated to be 0.94 km (Paradowski, 2020). Thus, active area and active fraction can be calculated to be 1.8 ± 0.4 km^2 and 16.7 ± 0.3%, respectively. This comet has also been observed by iSHELL installed at the NASA Infrared Telescope Facility (IRTF), which evaluated its water production rate to be $(3.98 \pm 0.45) \times 10^{28}$ /s at r_H = 1.04 au (May 13 2017) after its perihelion passage (Saki et al., 2021). According to the well-calibrated amateur website,

the Comet OBServation Database (COBS database; https://www.cobs.si/cobs/analysis/), the magnitude of this comet decreased from approximately 7.7 on May 13, 2017, to less than 8.5 on June 2, 2017. Considering this diminution of activity, water production rate was expected to be ~1 × 10^{28} /s on June 2, 2017, which is twice as large as our estimate.

3.5.4. C/2015 V_2 (Johnson)

C/2015 V_2 (Johnson) is a long-period comet with a perihelion distance and original semi-major axis of 1.64 au and 4.0 × 10^4 au, respectively. According to A'Hearn's classification (A'Hearn et al., 1995), this comet is a dynamically new comet. It passed its perihelion on June 12, 2017 (r_H = 1.64 au) and was observed by EXCEED on June 25, 2017 (r_H = 1.65 au). Its mean water production rate was estimated to be (1.4±0.3) × 10^{27} /s. This comet was also observed by SWAN and iSHELL. SWAN estimated its water production rate to be (8.4±0.2) × 10^{28} /s at r_H = 1.65 au on June 25, 2017, whereas iSHELL estimated it to be ~1.5 × 10^{28} /s at r_H = 1.64 au on June 7, 2017 (Combi et al., 2021). Considering that the activity of comet Johnson has been stable for a long time (see Fig.1 in Combi et al., 2021), iSHELL observations would estimate water production rate of ~1 × 10^{28} /s also on June 25, 2017. Surface equilibrium temperature and expected sublimation rate per unit surface are approximately 186 K and 7.2 × 10^{26} /km^2/s, and nucleus size was estimated to be 1.70 km (Paradowski, 2020). Active area and active fraction are 1.9±0.4 km^2 and 5.3 ± 1.1%, respectively.

3.6. **Summary and Unsolved Issues**

We observed four long-period comets using a UV spectrometer called EXCEED onboard the Hisaki satellite and estimated their water production rates and active areas.

Sensitivity of EXCEED around the wavelength of Ly-α (121.6 nm) has been significantly decreased over time due to the excessive brightness of surrounding geocorona. Since Ly-α emissions of standard stars are typically weaker than those of geocorona, a new calibration method using the Ly-α/Ly-β ratio of the geocorona was developed. The water production rates of four long-period comets were quantitatively estimated by comparing their obtained Ly-α radiance profiles with a simple analytical model. For all the four comets, smaller water production rates were obtained compared to other observation methods using SOHO/SWAN and IRTF/iSHELL. The cause of these systematic differences is constants such as velocities and lifetimes of particles in comae. In the Kaneda model, estimated water production rates is approximately proportional to the assumed velocities of hydrogen atoms, while those from observations by IRTF/iSHELL and SOHO/SWAN are proportional to the assumed velocity of water molecules and lifetimes of water molecules, respectively. Beside, most analytical models such as the Kaneda model assume that all the particles flow outward, and thus, estimated production rates are approximately half of those with numerical calculations assuming both outward and inward flows. In the case of observations by Earth-orbiters such as the Hisaki satellite, cometary Ly-α emissions are possibly reduced by 20% due to geocoronal absorption (Kuwabara et al., 2017). These accumulation of errors are thought to have led the large divergence of the results from observation instruments and analytical means. Further observational constraints on the physical parameters on particle kinetics in comae are primarily necessary.

As the opportunities for observing of long-period comets are limited, an increase in the number of observations is necessary for a statistical discussion. The proposed calibration method can increase the amount of observational data of comets analyzed in

the future, thereby providing a clearer insight into the different characteristics of comets and their effects on the planetary environments. In this study, spherically symmetrical Kaneda model was adopted as a simple analytical model of cometary hydrogen comae. To discuss the anisotropy of comae, I would like to construct an analytical model considering solar radiation acceleration with reference to Chamberlain model used in Chapter 2, although it was unnecessary due to positions of comets and the Earth in this time.

4. Radiation Transfer Model of the Lyman Alpha Line in the Comae of Comets

In Chapter 3, the spatial distributions of Ly-α radiance between the observational data of the Hisaki satellite and the analytical model of Kaneda et al. (1986) were compared . However, they deviate remarkably below the impact parameter of 5×10^4 km. In this chapter, I focus on multiple scattering, which is considered to be responsible for this discrepancy. In Section 4.1, the multiple scattering is introduced. The computational model for the radiative transfer processes of Ly-α rays in the comae of comets constructed in this study is explained in Section 4.2. In Section 4.3, the results of numerical calculations and observations using Hisaki are compared. Finally, the phenomena arising from multiple scattering in the comae of comets based on these results are discussed in Section 4.4.

4.1. **Multiple Scattering**

Hydrogen atoms absorb Ly-α rays and rapidly re-emit them (resonance scattering). Under optically thin conditions, most of the observed Ly-α rays were those emitted from the Sun and scattered only once by hydrogen atoms in the comae (known as single scattering: Fig. 4.1a). In contrast, under the optically thick conditions, the rays are scattered multiple times by several hydrogen atoms before reaching observers (known as multiple scattering: Fig. 4.1b). If the efficiency of absorption and re-emission of these rays were 100%, multiple scattering would barely change the observed Ly-α radiance distributions. However, as the actual efficiency is approximately 40% in reality, Ly-α radiance in the vicinity of nuclei becomes darker than expected by high hydrogen density.

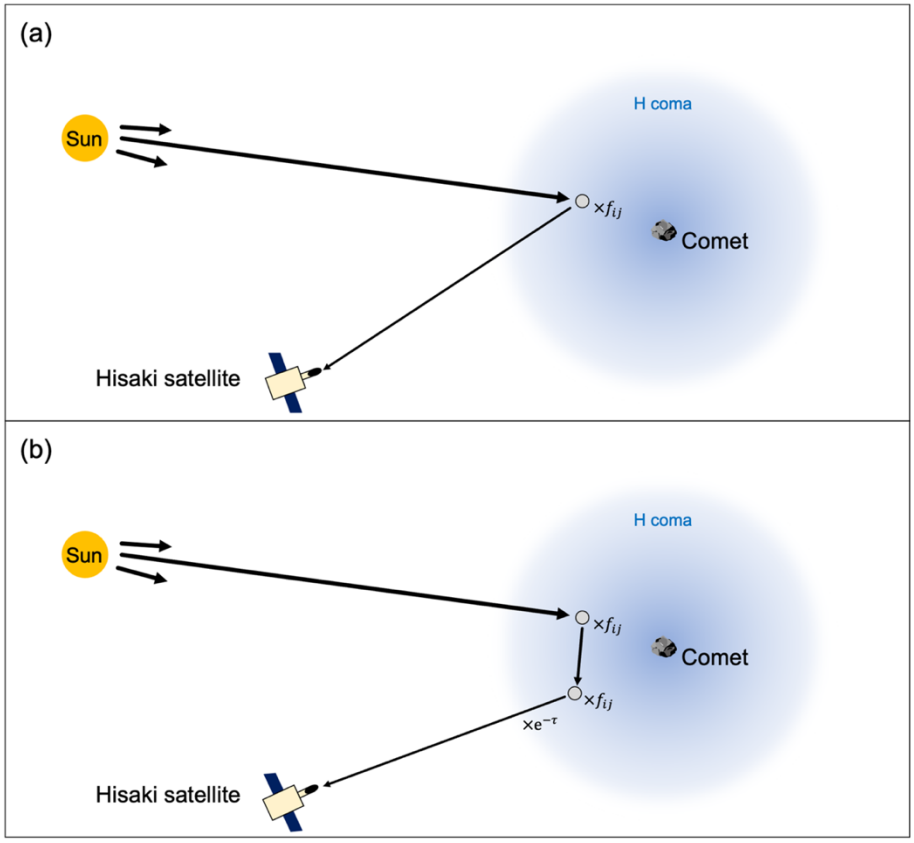

Fig. 4.1. Schematic representation of (a) single scattering and (b) multiple scattering, where f_{ij} and τ are oscillation strength and optical thickness, respectively.

As for comets, attempts have been made to reproduce the observed high-wavelength-resolution spectra of C/1996 B2 (Hyakutake) using the radiation transfer model (Richter et al., 2000). However, few studies have quantitatively calculated spatial distributions of Ly-α radiance although the necessity of considering multiple scattering has been recognized. This is mainly because UV observations of comets have long been driven primarily by instruments with low spatial resolution such as SOHO/SWAN, which cannot distinguish between optically thick and thin areas (e.g., Combi et al., 2019).

4.2. **Model Settings**

4.2.1. Number Density Distribution of Hydrogen Atoms

Prior to constructing the radiation transport model, the number density distribution of hydrogen atoms is numerically calculated. The number density of H_2O, OH, and H is calculated by a combination of the one-dimensional equation of continuity,

$$\frac{\partial f_i(r,v,t)}{\partial t} + v\frac{\partial f_i(r,v,t)}{\partial r} = 0 \ (i = 1,2,3) \tag{4.1}$$

and change in the particle number due to photodissociation and photoionization is as follows.

$$\frac{\partial f_1(r,v,t)}{\partial t} = -\frac{f_1(r,v,t)}{\tau_1} + \delta(r)\delta(v - v_1)Q_{\mathrm{H_2O}} \tag{4.2}$$

$$\frac{\partial f_2(r,v,t)}{\partial t} = -\frac{f_2(r,v,t)}{\tau_2} + \delta(v - v_2)\int \mathrm{d}v \frac{f_1(r,v,t)}{\tau_1} \tag{4.3}$$

$$\frac{\partial f_3(r,v,t)}{\partial t} = -\frac{f_3(r,v,t)}{\tau_3} + \delta(v - v_3)\int \mathrm{d}v \frac{f_1(r,v,t)}{\tau_1} + \delta(v - v_{3'})\int \mathrm{d}v \frac{f_2(r,v,t)}{\tau_2} \tag{4.4}$$

The first term of right hand of each equation indicates the loss of each particle due to photodissociation or photoionization. Other terms express the supply due to sublimation of the surface ice or photodissociation of parent molecules. r, v and t are the altitude from nuclei, velocity of particles, and time, respectively. f_i is the phase-space density of H_2O ($i = 1$), OH ($i = 2$), and H ($i = 3$). τ_1 and τ_2 are the photodissociation lifetimes of H_2O and OH molecules, and τ_3 is the photoionization lifetime of the H atoms. I adopt τ_1 =27 h, τ_2=23 h, and τ_3=159 d at the heliocentric distance of 1 au following the database of PHoto Ionization/Dissociation RATES (https://phidrates.space.swri.edu/) as was done in Chapter 3. The velocity of sublimated H_2O molecules is set at $0.8 \times r_h^{-2}$ km/s (v_1) and velocity of generated particles through the photodissociation was assumed to be uniform for each dissociation process. The

velocity of OH molecules and H atoms generated through $H_2O \rightarrow OH + H$ was set at $0.8 \times r_h^{-2}$ km/s (v_2) and 20 km/s (v_3), respectively, and that of H atoms generated by $OH \rightarrow H + O$ was set to be 8 km/s ($v_{3'}$). All the parameters except for velocity of H_2O and OH molecules are the same as those used for the model in Chapter 3 (Kaneda et al., 1986). Interatomic collisions and other kinds of parent molecules of hydrogen atoms were ignored in this calculation to simplify the discussion. The Runge–Kutta (RK4) method was adopted as a time evolution scheme. Calculated number densities of hydrogen atoms are approximately proportional to assumed water production rates and inversion of assumed velocities of hydrogen atoms.

Fig. 4.2 shows the number density distribution and the column density distribution along the line of sight of the Hisaki satellite as calculated by the constructed model. Geometry and water production rates are set assuming the observation of C/2013 US_{10} (Catalina). Currently, no apparent bend appears around the altitude of 5×10^4 km, contrary to the observations by Hisaki.

4.2.2. Radiance Distribution of Lyman Alpha Emission

Using the number density distributions calculated in Subsection 4.2.1, Ly-α radiance distributions were calculated. Subsequently, I calculate the quantity of Ly-α rays entering the field of view of Hisaki from a particular direction after leaving the Sun and being scattered several times in the comae using the Monte–Carlo method following Richter et al. (2000). To reduce the computational cost, I virtually eject photons from Hisaki and calculate the probability of them reaching the Sun, utilizing the symmetry of scattering phase function. The specific processes are described below (Fig. 4.3).

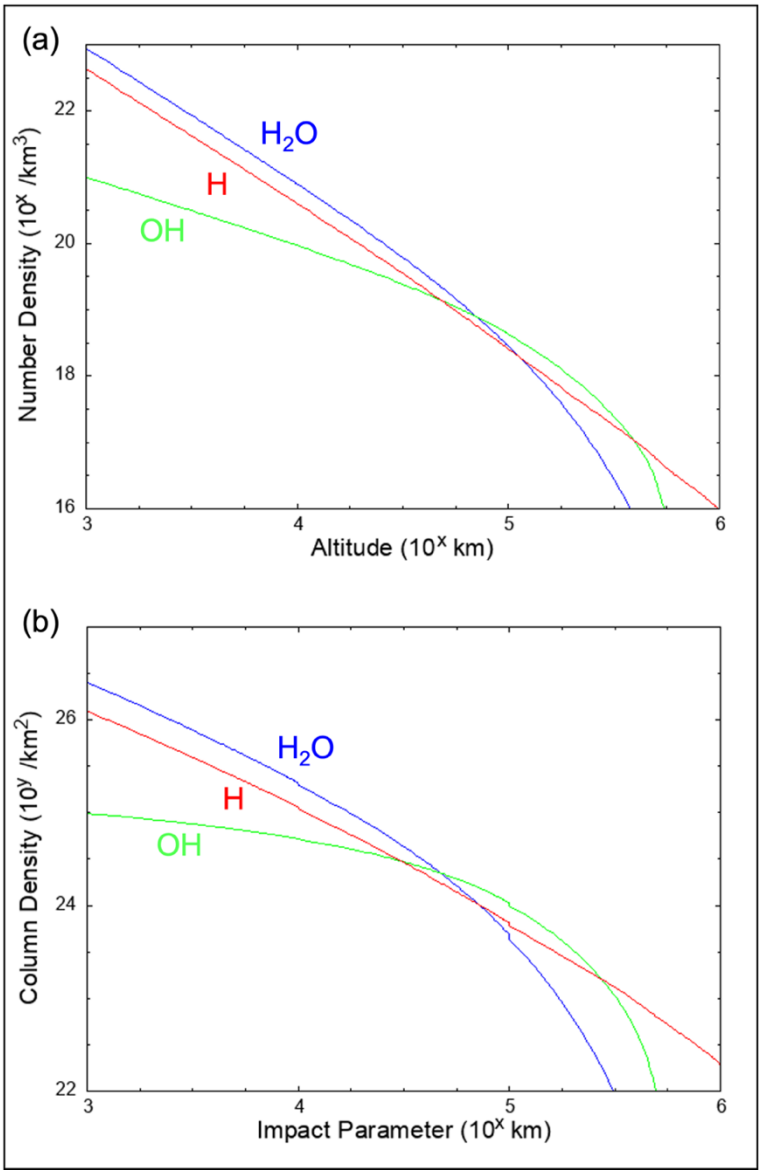

Fig. 4.2. (a) Number density and (b) column density along the line of sight of the Hisaki satellite as calculated using the constructed model.

The blue, green, and red lines represent the number density and column density of H_2O, OH and H, respectively.

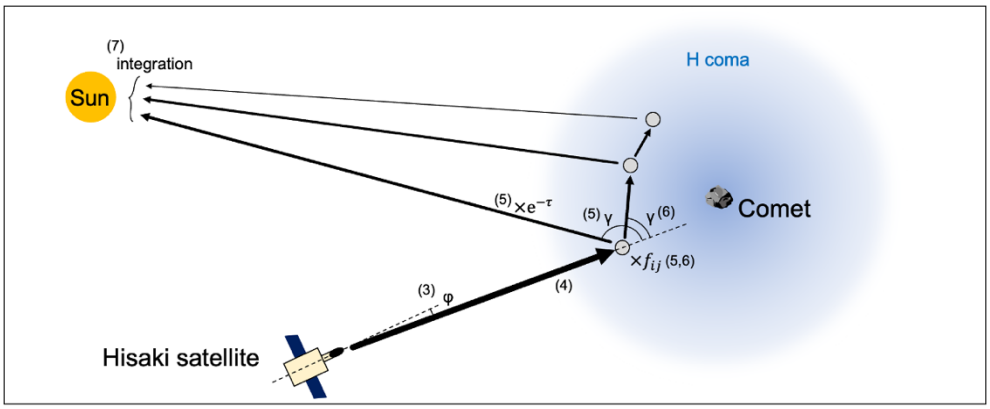

Fig. 4.3. Schematic representation of radiation transfer model constructed in this study. f_{ij}, τ, ϕ and γ are the oscillation strength, optical thickness, viewing angle, and scattering angle, respectively. (4) to (7) correspond to the calculation processes described in the text.

(1) Set a viewing angle ϕ

(2) Set a wavelength λ

(3) Eject photons from Hisaki into the direction of the viewing angle ϕ

(4) Let photons travel straight through the coma until the optical thickness reaches a random number τ. The cumulative probability density of the random number τ is $1 - e^{-\tau}$.

(5) Calculate the probability of reaching the Sun after scattering. This corresponds to the radiance of Ly-α rays entering Hisaki after being scattered i-times. The probability density of being scattered in the direction of the scattering angle of γ is $\left(\frac{11}{12} + \frac{1}{4}\cos^2\gamma\right)/4\pi$ (Brandt and Chamberlain, 1959). Besides, the number of photons reaching the Sun is reduced by scattering efficiency, which is determined by excitation efficiency and single scattering albedo, and by the probability of being scattered into other directions while proceeding to the Sun,

$e^{-\tau}$. Oscillator strength $f_{12} = 0.4$ is used as an excitation efficiency and single scattering albedo is assumed to be 1 as comae are sufficiently tenuous.

(6) Determine the subsequent scattering angle γ for the calculation of the radiance of the $(i+1)$-th scattered component. The probability density of scattering angle γ follows $\left(\frac{11}{12} + \frac{1}{4}\cos^2\gamma\right)/4\pi$, again. When scattered, the number of photons is reduced by a factor of f_{ij}.

(7) Repeat (4) to (6) n-times and integrate the radiance of Ly-α rays entering Hisaki after being scattered for i-times as calculated in step (5) from $i = 1$ to n. The value of "n" can be decided arbitrarily considering the balance of calculation cost and calculation accuracy.

(8) Repeat (2) to (7) with changing the wavelength and integrate obtained brightness over the wavelength.

(9) Repeat (1) to (8) for different impact parameters and obtain the radiance profile of Ly-α rays.

The solar spectra around the Ly-α line are generated with reference to Kowalaska-Leszczynska et al. (2018, 2020). Hydrogen temperature in the comae is assumed to be 5×10^3 K. Dependence of the results on temperature is discussed in Appendix 4. A1. As radiance decreases with the oscillator strength each time it scatters, the results are almost the same when considering four or more scattering events as well as when considering up to three-time scatterings. The dependence of the results on the number of scatterings is also discussed in Appendix 4. A2. Therefore, only the results of calculations considering up to three-time scattering are shown in this chapter. The calculated radiance is proportional to the solar radiation flux, and, in optically thick

regions, is inversely proportional to the scattering cross section. It also increases with the larger input hydrogen number densities, as discussed in Subsection 4.4.1. Note that absorption of Ly-α rays by particles other than hydrogen atoms, such as H_2O molecules and organic substances, is assumed to be far less than that by hydrogen atoms in this study.

4.3. **Comparison with Observational Data Obtained by the Hisaki Satellite**

The calculated Ly-α radiance distribution is represented by the red lines in Fig. 4.4, whereas the blue lines in Fig. 4.4 represent the radiance distributions only considering single scattering and black points are observational data by Hisaki. Observations of Ly-α radiance distributions by Hisaki are well reproduced by consideration of multiple

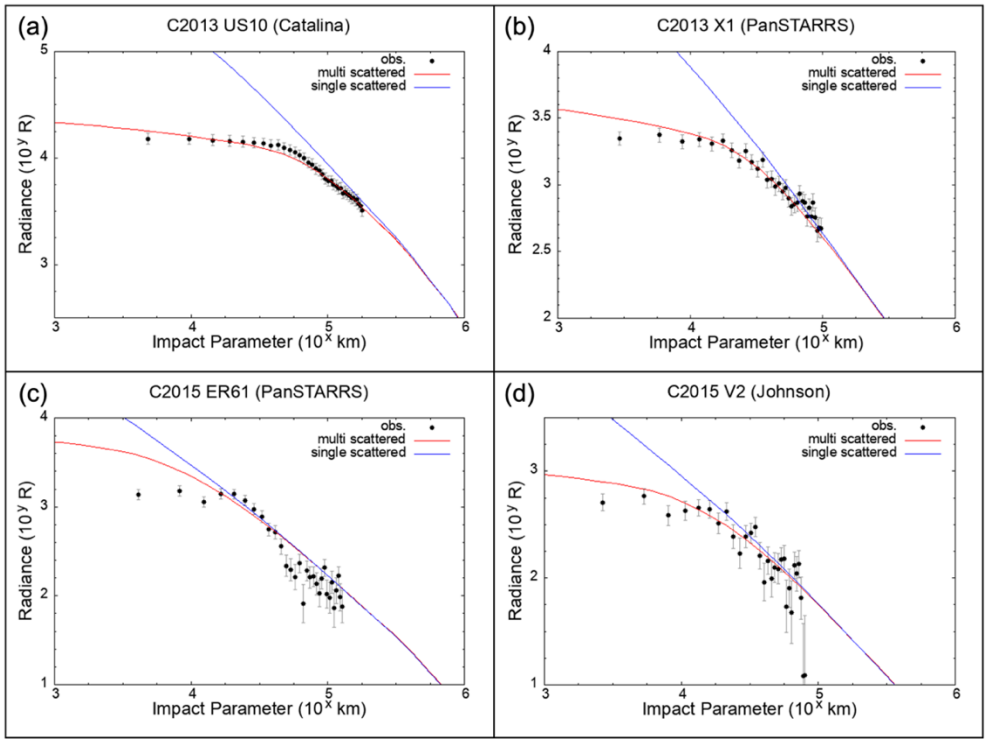

Fig. 4.4. Comparison of calculated Ly-α radiance distribution and observational data obtained by the Hisaki satellite.

scattering, which shows that the Ly-α rays in the comae are greatly affected by multiple scattering.

However, only for C/2015 ER_{61} (PanSTARRS), consistency between the model and the observations did not improve as much as that in the other comets, even if multiple scattering was considered. I attribute this to the fact that only C/2015 ER_{61} among the four comets has experienced outbursts (e.g., Sekanina 2017). When outbursts occur, more dust containing water ice is transported to high altitudes than the amounts present in ordinary comets. As a result, because the generation regions of water molecules and hydrogen atoms expand, hydrogen density in the vicinity of the nuclei is considered to be conversely lower than usual. Besides, scattering due to soaring dust is also possible cause. For 67P/CG, possible UV attenuation due to dusts was pointed out (Johansson et al., 2017).

When the spatial resolution is low, the image is smoothed and a bend possibly appears in the radiance profile curve, as shown Fig. 4.5. The red line represents a

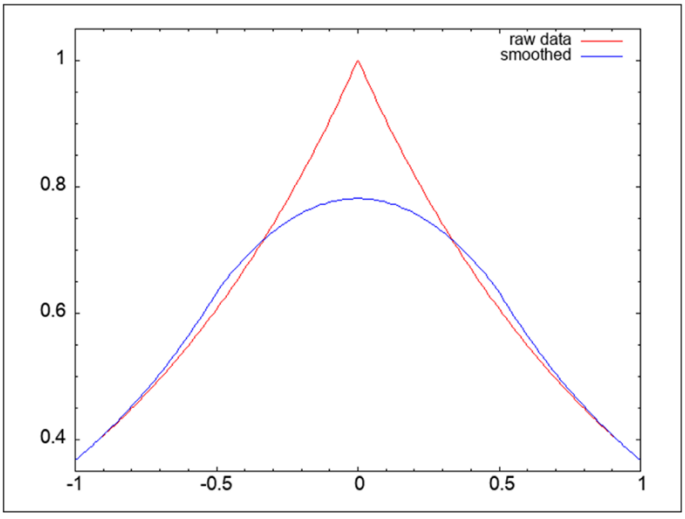

Fig. 4.5. An example of the appearance of an inflection point due to the low spatial resolution.

The red line is $y = e^{-|x|}$, and the blue line is the moving average of the red line.

function of $y = e^{-|x|}$, and the blue one is the moving average of the red one. Additionally, an inflection point appears in the graph. Similarly, a bend can occur in the Ly-α radiance profile in the comae due to the low spatial resolution. However, this effect should appear below the impact parameter of 3×10^3 km as the pointing and tracking accuracy of Hisaki is in the order of 10". Although there have been several numerical models considering the effect of interatomic collisions, they are unlikely to produce an apparent bend around the altitude of 5×10^4 km (e.g., Fig. 6 of Tenishev et al., 2008). From these facts, I conclude that the Ly-α radiance distributions obtained by Hisaki can be primarily explained by multiple scattering.

4.4. **Importance of Multiple Scattering in General Comets**

In this section, the constructed radiation transfer model is applied to general comets with a variety of activities (i.e., water production rate), to discuss the conditions under which the multiple scattering becomes dominant, and phenomena caused by multiple scattering. I set the heliocentric and geocentric distances of comets to 1 au and the phase angle to 60°.

4.4.1. Conditions Under Which Multiple Scattering Occur

Fig. 4.6a shows the Ly-α radiance in the anti-Sunward side as a function of the hydrogen column density calculated with various water production rates. When the column density is lower than 5×10^{22} /km^2, radiance is proportional to column density, suggesting that single scattering should be dominant. To clarify this, I introduce an index named "effective g-factor" index defined by I/N$\times10^6$, where I is the Ly-α radiance (Rayleigh) and N is the hydrogen column density (cm^2). Fig. 4.6b shows the calculated

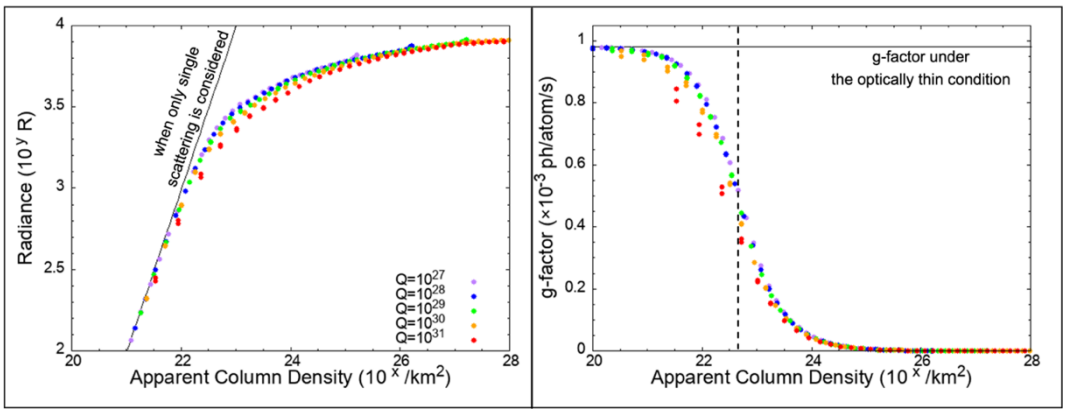

Fig. 4.6. (a) Ly-α radiance and (b) effective g-factor as a function of column density along the line of sight.

Multiple scattering becomes dominant over the number density of 5×10^{22} /km^2.

effective g-factor as a function of column density. Effective g-factor at a column density of 5×10^{22} /km^2 is already half of that under the optically thin condition calculated by Equation (1.14), and above the column density of 1×10^{24} /km^2, it becomes less than 5% of the g-factor under the optically thin condition. The column density is converted to the impact parameter as shown in Fig. 4.7, using the hydrogen number density model constructed in Subsection 4.2.1. Thus, multiple scattering becomes dominant below the impact parameter of 10^5 km for comets with a water production rate of 10^{29} /s.

Observations using an instrument with low spatial resolution, such as SOHO/SWAN, are reproduced by spatially averaging the radiance from the nuclear to the impact parameter of r corresponding to the spatial resolution. The relationship between the spatial resolution and effective g-factor is shown in Fig. 4.8. The disregard of multiple scattering causes an error of more than twice in the deduced hydrogen column density with a spatial resolution of 3×10^6 km when the water production rate is 10^{29} /s. Thus, when a particular comet with a geocentric distance of 1 au and with a water production rate of over 10^{29} /s is observed by SOHO/SWAN, whose spatial

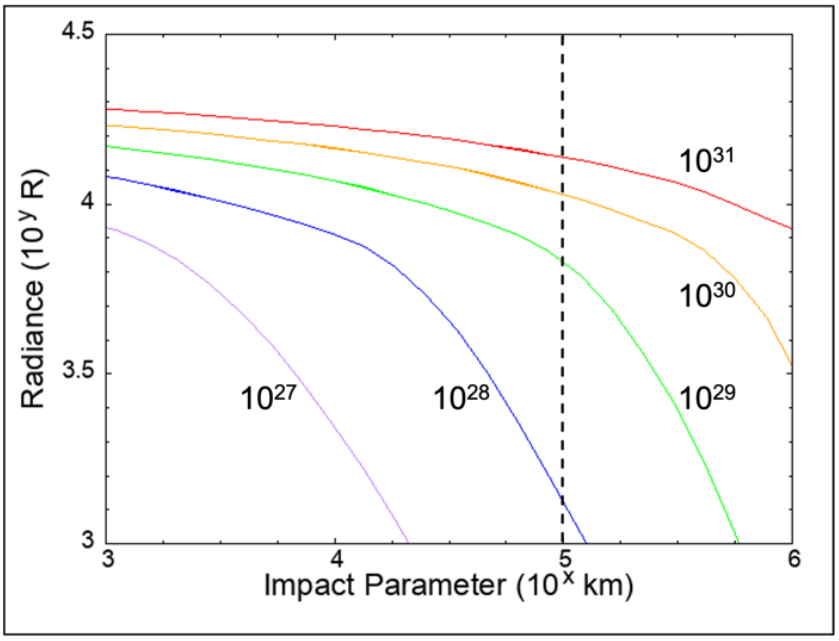

Fig. 4.7. Ly-α radiance as a function of impact parameter.

Numbers attached to lines are water production rates (/s).

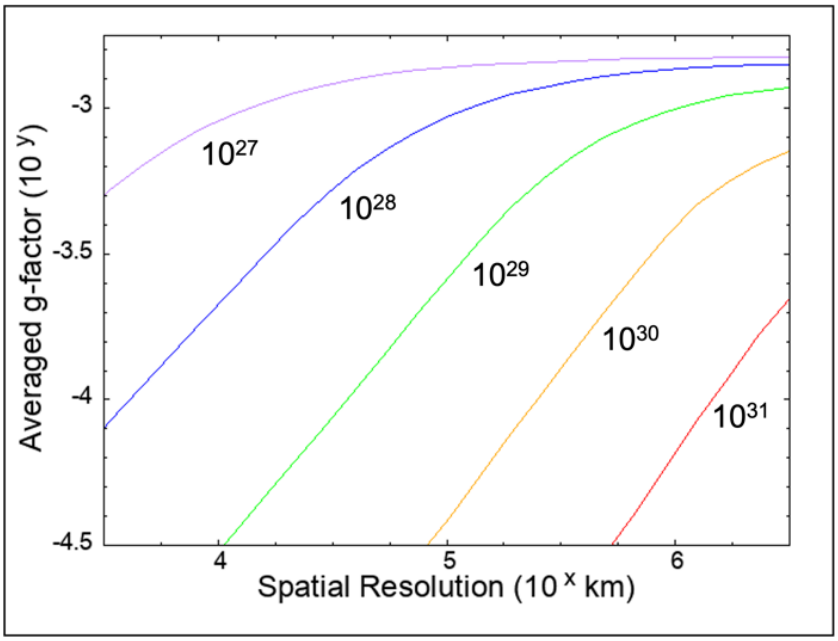

Fig. 4.8. Averaged effective g-factor as a function of spatial resolution.

Numbers attached to lines are water production rates (/s).

resolution is 1° (Bertaux et al., 1995), the water production rate would be underestimated at less than half of the actual value.

4.4.2. Sunward / Anti-sunward Side Asymmetry

Radiance in both the sunward regions and anti-sunward regions with a water production rate of 10^{31} /s is shown in Fig. 4.9. Although the hydrogen number density calculated in Subsection 4.2.1 was spherically symmetrical, Ly-α radiance on the anti-Sunward side is 1.5% darker than that on the Sunward side. This is because photons scattered on the anti-sunward side tend to undergo longer optical path length and be scattered more times than those on the sunward side. Although it is an interesting phenomenon that a spherically symmetry number density distribution produces an asymmetrical brightness distribution, it is challenging to detect asymmetry of less than

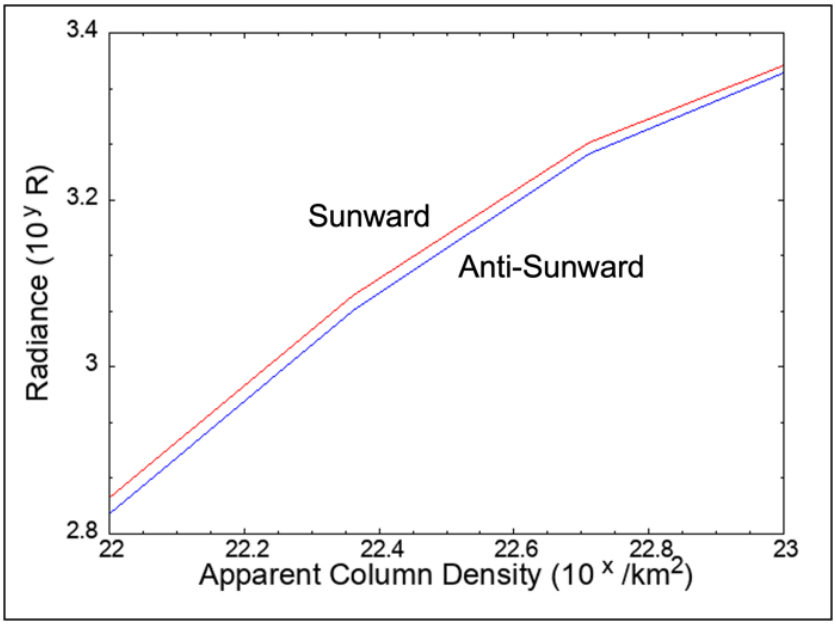

Fig. 4.9. Sunward / anti-sunward asymmetry of Ly-α radiance.

Even when hydrogen number density is spherically symmetrical, Ly-α radiance on the Sunward side is 1.5% brighter than that on the anti-Sunward side when the water production rate is 10^{31} /s.

1.5%.

4.4.3. Apparent Increase of D/H Ratio

The wavelength of the Ly-α line of deuterium is 121.534 nm, which differs by 33 pm from that of hydrogen (121.567 nm). As hydrogen temperature in the comae is several thousand kelvins at most and the width of their emission lines is sufficiently narrow (~5 pm), the emission line of hydrogen and that of deuterium do not overlap. In addition, the D/H ratio of comets is 5×10^{-4} (67P/CG: Altwegg et al., 2015) at maximum. Thus, even in the vicinity of nuclei, where the hydrogen Ly-α line becomes optically thick, the deuterium Ly-α line remains optically thin. This implies that in approaching nuclei, the rate of increase of radiance of hydrogen Ly-α rays weakens, whereas that of deuterium Ly-α rays steadily increases (Fig. 4.10a), thereby increasing of the apparent

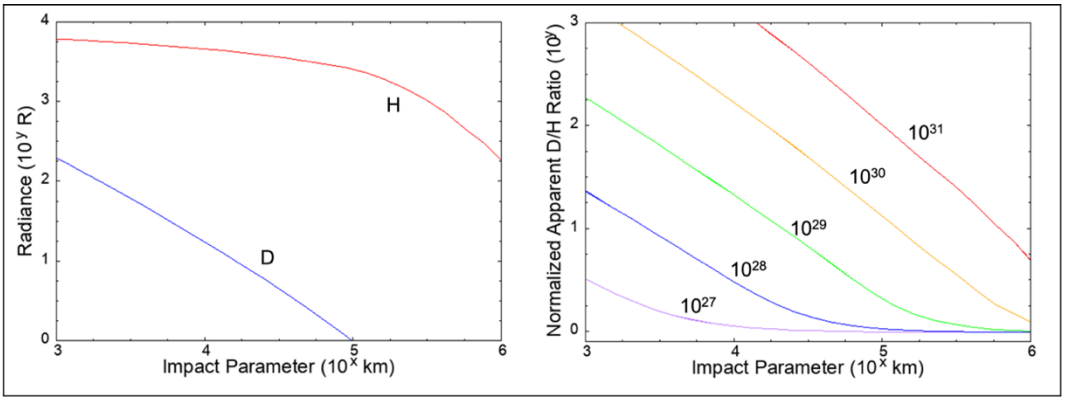

Fig. 4.10. (a) Ly-α radiance profiles of hydrogen and deuterium with a water production rate of 10^{29} /s. (b) Apparent D/H ratio as a function of the impact parameter.

(a) As the impact parameter decreases, deuterium Ly-α radiance steadily increases. In contrast, the rate of increase of radiance of hydrogen Ly-α weakens. (b) Numbers along the lines are water production rates (/s). Apparent D/H ratio increases as the impact parameter decreases.

D/H ratio. Fig. 4.10b shows the apparent D/H ratio when the D/H number density ratio is fixed at 1. For the case of a comet with a water production rate of 10^{29} /s, the apparent D/H ratio is consistent with the D/H number density ratio in optically thin regions; however, it decreases below the impact parameter of 2×10^{5} km. This is a theoretical prediction and will possibly be verified by the ongoing CI mission (Snodgrass & Jones, 2019). Besides, this effect is significant for the feasibility study on the measuring the D/H ratio by CI (see Chapter 6).

4.5. **Summary**

Through the analysis of observational data obtained by the Hisaki satellite conducted in Chapter 3, I found that the slope of the Ly-α radiance distribution in the comae of the comets significantly decreases below the impact parameter of 5×10^{4} km. Subsequently, I constructed a Monte–Carlo radiation transfer model accounting for multiple scattering of photons, which has long been qualitatively considered to be necessary, resulting in observations being successfully reproduced.

Using the constructed model, I quantitatively demonstrated the conditions under which multiple scattering is dominant for general comets. In particular, the number density should be calculated considering multiple scattering even for low spatial resolution instruments such as SOHO/SWAN.

I clarified that a spherically symmetric number density distribution could generate a Ly-α radiance distribution with 1.5% sunward/anti-sunward asymmetry. Besides, the apparent D/H ratio increased in the vicinity of nuclei. Variation of the apparent D/H ratio due to multiple scattering will possible be verified by the ongoing CI mission.

5. Optical Design and Performance Evaluation of the Hydrogen Imager Onboard Comet Interceptor Spacecraft

As discussed in the summary of previous comet exploration missions in Subsection 1.3.1, there have previously been no spacecrafts that approach long-period comets. Currently, the Comet Interceptor (CI) mission, which is the first mission to approach a long-period comet or an interplanetary object is underway. I am especially engaged in the development of Hydrogen Imager (HI) onboard CI. Section 5.1 describes the specifics of CI and HI. The required performance of HI is examined in Section 5.2. In Section 5.3, the basic design of the optical system of HI and optimization of parameters are discussed. I describe experiments to measure the transmittance of the band-pass filter (BPF) and the reflectance of the mirrors adopted in the bread board model (BBM) of HI in Section 5.4, and the characteristics of gas filter's transmittance adopted in the BBM of HI in Section 5.5.

5.1. **Comet Interceptor Mission and Hydrogen Imager**

5.1.1. Comet Interceptor Mission

CI is a spacecraft led by JAXA and ESA (Snodgrass & Jones, 2019). After its planned launch in 2029, it will stay at the second Lagrangian point of the Sun-Earth system for several years (L2 waiting phase). When a long-period comet or an interstellar object with a good observed condition is found, CI will leave the L2 point to fly by the comet (approach phase). This will be the first time a long-period comet or an interstellar object will have been approached.

Flyby observations of comets risk damage to spacecrafts due to dust ejected from nuclei. Therefore, in the CI mission, two probes (B1 and B2) will be separated from the

parent probe (A) a few days before the closest approach (CA) and will get closer to the comet than the parent (comet fly-by phase). Although the target body will be determined after launch and the specific trajectory of spacecraft has not been determined, B1 is planned to come within 850 km of the target.

5.1.2. Hydrogen Imager Onboard CI B1

HI is a camera onboard the B1 probe which investigates the radiance distribution of Ly-α emission in detail. During the approach phase, HI will intermittently capture the two-dimensional radiation distribution of Ly-α in the coma (imaging mode). An interference filter is used to transmit only rays with the wavelength around the Ly-α line. During the comet fly-by phase, HI is used as a photometer without spatial divisions to acquire higher time resolution (light curve mode). Although the data obtained at each instant is zero-dimensional, Ly-α radiance profiles with high spatial resolutions can be substantially obtained using the movement of the probe relative to the comet nucleus. In addition, Ly-α radiances of both hydrogen and deuterium can be quantitatively measured by using absorption cells, a process which is introduced in detail in the next section.

5.1.3. Absorption Cells Installed in HI

Measuring spatial distributions of D/H ratios will reveal dependence of escape flux of cometary gases on particle mass. It is unlikely to be able to measure the D/H ratio distribution using HI unless the target comet is hyper-active. However, this instrument is important to establish a D/H ratio measurement method using small instruments for future spatial resolution. In addition, by comparing the D/H ratio measured by optical

observations by HI and the HDO/H_2O ratio measured by particle measurement by MANiaC, will clarify elementary processes of molecule photodissociation in cometary comae such as timescales and excess energy.

Spectrometers with sufficient wavelength resolution to distinguish hydrogen and deuterium Ly-α emission lines are too heavy to be mounted on small satellites. Then, absorption cells (Fig. 5.1) are important as optical devices for measuring D/H ratios under severe constraints of being mounted on small spacecraft. Absorption cells are glass cells of several centimeters of length that are filled with hydrogen (deuterium) molecules. They have been installed in a Lyman-alpha photometer onboard Venera (Bertaux et al., 1978), in SWAN onboard SOHO (Bertaux et al., 1995) and in the Ultraviolet Spectrometer (UVS) onboard Nozomi (Taguchi et al., 2000). By using absorption cells, radiance of Ly-α rays of hydrogen and deuterium, whose wavelength differs by only 33 pm, can be measured separately. A schematic image of this measurement principle is shown in Fig. 5.2. When a voltage is applied to filaments inside cells, the filaments are heated, resulting in the dissociation of hydrogen (deuterium) molecules into atoms. Note that I express turning on/off the voltage applied

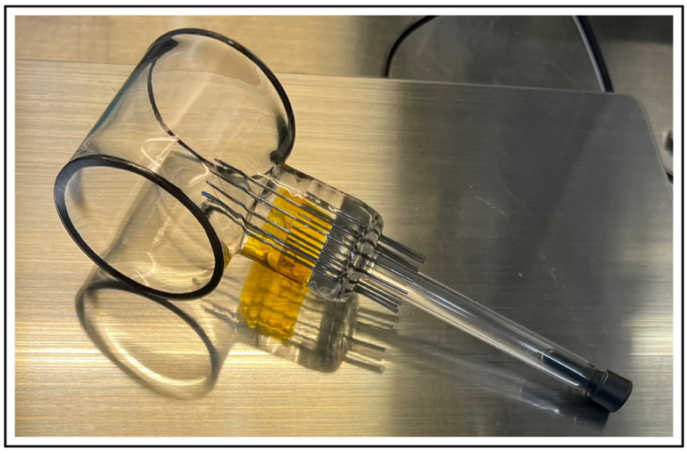

Fig. 5.1. Picture of an absorption cell.

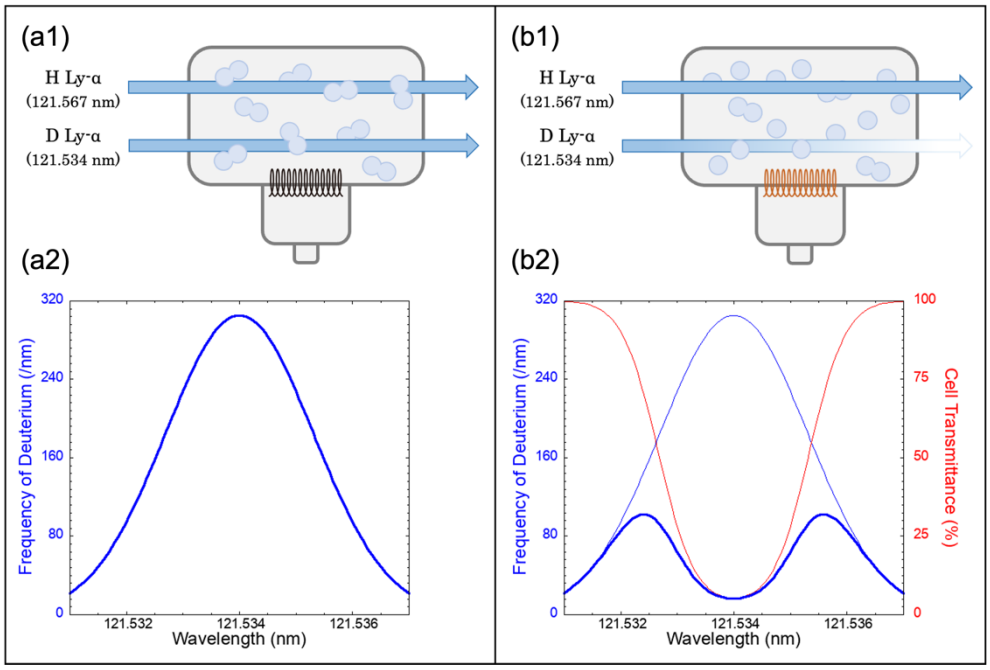

Fig. 5.2. Schematic representation of measurement principle.

This is an example of an instance which deuterium absorption cells are used. The blue line in (a2) is an example spectrum of deuterium Ly-α in comets' comae. When applying voltage on the filament, dissociated deuterium in the cell absorbs Ly-α like the red line in (b2) and observed spectrum changes into the thick blue line in (b2).

to the filaments in cells as "turning on/off cells" hereafter. Dissociated atoms then absorb Ly-α rays with a wavelength of 121.567 nm (121.534 nm), and thus cells work as switchable, narrow band-stop filters (notch filters). In this way, radiance of Ly-α rays of hydrogen (deuterium) atoms can be measured using the difference in radiances for cases when the cell is turning on and off. However, the doppler effect alters the wavelength of Ly-α emissions from targets. This causes the emissions to appear outside of the narrow absorption wavelength range when the relative velocity between the target and the observer is larger. Therefore, the viewing angle of HI will be set orthogonally to the velocity vector of the B1 probe during the comet fly-by phase to reduce the relative

velocity between the target and the spacecraft as shown in Fig. 5.3.

To measure the radiance of Ly-α emission by hydrogen and deuterium during the comet fly-by phase, the deuterium cell is repeatedly switched on and off while the hydrogen cell remains constant. The apparent D/H ratio is converted to the number density ratio using the results discussed in Subsection 4.4.3. This process is discussed in Section 6.4 in detail. If the relative velocity between the comet and the spacecraft is small during the approach phase, the temperature of hydrogen in the coma can also be measured by observations with a variety of filament temperatures, which is described in detail in the Appendix 5.A1.

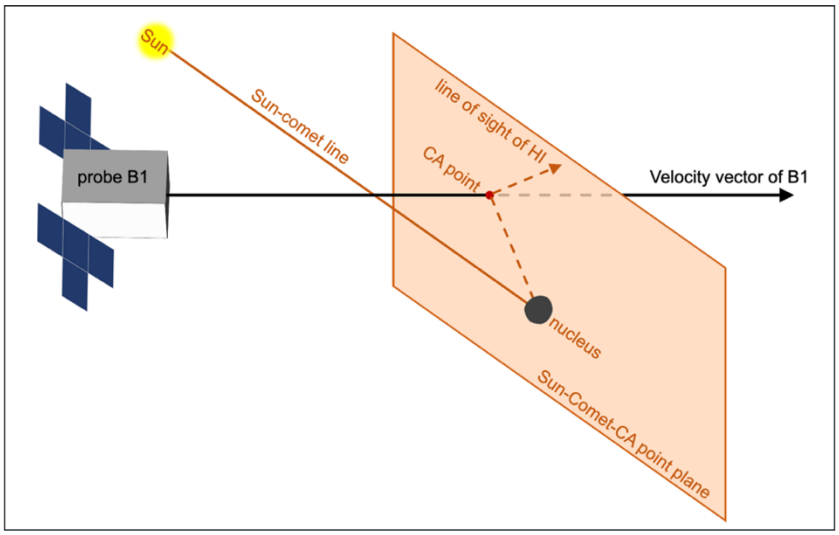

Fig. 5.3. Schematic representation of the B1 probe's orbit and line of sight of HI during the comet fly-by phase.

5.2. **Required Performance of HI**

5.2.1. Field of View and Spatial Resolution

To measure background radiance, such as Ly-α emission from interplanetary media in the field of view, the entire coma extending 10^5-10^7 km must be captured from a distance of approximately 1 au using imaging mode during the approach phase. Thus, FOV is required to be wider than $\tan(10^7 \text{ km}/1 \text{ au}) = 3.8°$.

As discussed in Chapters 3 and 4, multiple scattering and interatomic collisions are expected to be effective below the altitude of 10^4-10^5 km. To calculate the water production rate using the method described in Chapter 3 and to analyze the detailed effects of multiple scattering and interatomic collisions on the Ly-α radiance distribution, it is necessary to observe optically thick areas and thin areas separately. This requires that spatial resolution be finer than 10^3 km (one tenth of 10^4 km) in imaging mode during the approaching phase, when the distance between the spacecraft and the target is larger than 10^6 km. Therefore, spatial resolution is required to be finer than $\tan(10^3 \text{ km}/10^6 \text{ km}) = 0.06°$.

5.2.2. Wavelength Resolution

In comae of comets, OI 1304 and NI1168 are relatively bright emission lines whose wavelengths are close to Ly-α 121.6 nm. Since oxygen and nitrogen are heavier than hydrogen, they tend to stay close to nuclei. Therefore, they can be contaminants especially in the comet fly-by phase when the coma near the nucleus is observed. The oscillator strengths of HI1216, the OI1304 triplet, and the NI1168 doublet are 4.16×10^{-1}, $\sim 5 \times 10^{-2}$, and 3×10^{-2}, respectively, according to NIST Atomic Spectra Database Lines Form (https://physics.nist.gov/PhysRefData/ASD/ lines_form.html). According to

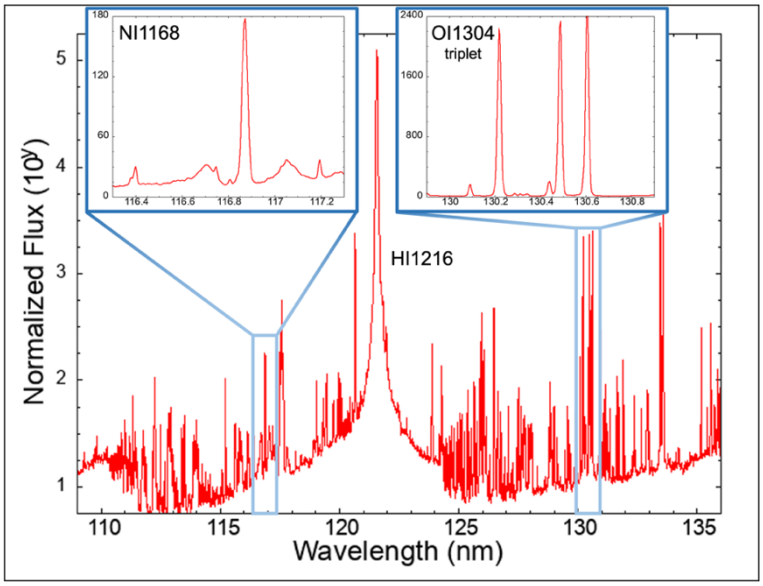

Fig. 5.4. An example of solar spectra.

Solar spectra were derived from the documentation of BAS2000.

the documentation of BAS2000 (https://bass2000.obspm.fr/solar_spect.php, based on Curdt et al., 2001), the solar flux ratio of these lines is approximately HI1216 : OI1304 : NI1168 ~ 5×10^2 : 10 : 1 (Fig. 5.4). Here it should be note that the solar fluxes of the three lines of the oxygen triplet are all the same magnitude, and that the solar flux of NI1169 is approximately five times larger than that of NI1167. Thus, radiance ratio is HI1216 : OI1304 : NI1178 ~ 7×10^3 : 50 : 1, if the number densities of hydrogen, oxygen and nitrogen atoms are the same. As discussed in Chapter 4, multiple scattering possibly reduces Ly-α radiance by approximately less than one-fiftieth of radiance calculated when only considering single scattering. Therefore, if the transmittance of the BPF at the wavelength of 130.4 nm is one-fifth less than that at the wavelength of 121.6 nm, contamination of OI1304 and NI1178 can be reduced by less than 10% of the radiance of HI1216. Since the number density of oxygen atoms is considered to be smaller than that of hydrogen atoms in practice, this restriction is relaxed a little more.

When using absorption cells for observations during the comet fly-by phase, a spatial resolution higher than 16 pm, which is half of difference in wavelength of Ly-α rays of hydrogen and deuterium, should be achieved to measure the Ly-α radiance of hydrogen and deuterium separately.

5.2.3. Effective Area

One of the features of the CI mission is the selection of a target comet after launch. Therefore, we should determine required performance by understanding the frequency distribution of brightness of long-period comets observed in the past. Table 5.1 and Fig. 5.5 show Ly-α radiances and water production rates at the heliocentric distance of 1 au based on past UV observations. To unify standards of comparison, the following scaling is performed. First, if the heliocentric distance r_H published in the paper is not 1 au, water production rates are converted to those at r_H = 1 au assuming that they are proportional to r_H^{-2}. Radiance is converted to the value at the heliocentric distance of 1 au assuming it is proportional to r_H^{-4} since both water production rate and g-factor are assumed to be proportional to r_H^{-2}. Most values in Table 5.1 have already been converted to those at r_H = 1 au by Combi et al. (2019). Thus, the shape of the histogram does not change remarkably even when water production rates are assumed to be proportional to r_H^{-1} or r_H^{-3}. For instances in which radiance is not described in papers, it is calculated using the analytical solution of Kaneda et al. (1986) and marked with an asterisk (*) in Table 5.1.

The expected range of observed Ly-α radiance is approximately 10^3-10^5 R at an altitude of 10^5 km, which means that wide dynamic range is necessary. Assuming that the radius of the detector is 10 mm as described in Subsection 5.3.1, dark noise (~ 1

cps/cm^2) and noise due to radiation rays (< 5 cps/cm^2) are expected to be ~ (1+5) cps/cm^2 × π × (1 cm)^2 ~ 2 × 10^1 cps. Therefore, for the signal to be 10 times larger than the noise, (2 × 10^2) cps, the effective area (geometrical area times total efficiency) is required to be larger than ~2×10^2 cps / 10^3 R / 10^6 × 4π/(3.8°/180× π)^2 sr ~ 6×10^{-4} cm^2, even in the darkest case (~10^3 R).

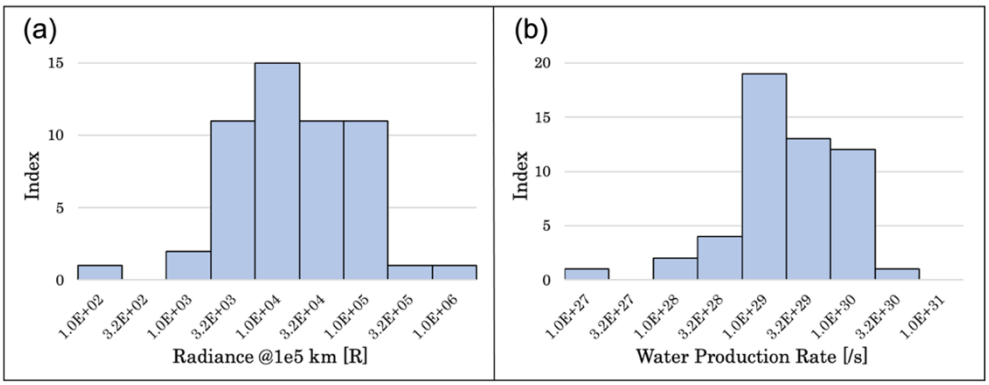

Fig. 5.5. Histogram of (a) Ly-α radiance at the altitude of 10^5 km and (b) water production rate reported in previous studies.

All the values are converted into equivalent values at the heliocentric distance of 1 au.

Comets	r_h [au]	I [R] @10^5 km @1 au	Q_{H2O} [/s] @1 au	Reference
C/1973 E_1 (Kohoutek)	0.18	2.1×10^3	3.2×10^{27}	Keller & Merier, 1976
	0.434	1.8×10^3	1.2×10^{29}	Merier et al., 1976
	0.183	5.6×10^2	1.8×10^{29}	
	0.434	1.8×10^3	1.8×10^{29}	Combi & Smyth, 1988
	0.183	5.6×10^2	2.8×10^{29}	
C/1975 V_1 (West)	0.38	$*3.4\times10^4$	4.6×10^{29}	Combi et al., 2019
C/1995 O_1 (Hale-Bopp)	1	$*1\times10^6$	1.4×10^{31}	Combi et al., 2019
	0.92	7.2×10^4	8.5×10^{30}	Combi et al., 2000
C/1996 B_2 (Hyakutake)	1	$*3.8\times10^4$	5.1×10^{29}	Combi et al., 2019
C/1996 Q_1 (Tabur)	1	$*3.0\times10^2$	4.1×10^{28}	Combi et al., 2019
C/1997 O_1 (Tilbrook)	1	$*5.4\times10^3$	7.3×10^{28}	Combi et al., 2019
C/1998 U_5 (LINEAR)	1	$*3.5\times10^3$	4.8×10^{28}	Combi et al., 2019
C/1999 H_1 (Lee)	1	$*2.1\times10^4$	2.9×10^{29}	Combi et al., 2019

Table 5.1. List of observed Ly-α radiances at the altitude of 10^5 km and water production rates. All values were converted to the values at the heliocentric distance of 1 au.

Comets	r_h [au]	I [R] @10^5 km @1 au	Q_{H2O} [/s] @1 au	Reference
C/1999 J_3 (LINEAR)	1	*2.4×10^3	3.3×10^{28}	Combi et al., 2019
C/1999 N_2 (Lynn)	1	*3.0×10^3	4.1×10^{28}	Combi et al., 2019
C/1999 S_4 (LINEAR)	1	*2.4×10^3	3.2×10^{28}	Combi et al., 2019
C/1999 T_1 (McNaught –Hartley)	1	*4.1×10^4	5.5×10^{29}	Combi et al., 2019
C/2000 WM_1 (LINEAR)	1	*7.4×10^3	1.0×10^{29}	Combi et al., 2019
C/2001 A_2 (LINEAR)	1	*7.4×10^3	1.0×10^{29}	Combi et al., 2019
C/2001 OG_{108} (LONEOS)	1	*1.5×10^3	2.0×10^{28}	Combi et al., 2019
C/2001 Q_4 (NEAT)	1	*5.2×10^4	7.0×10^{29}	Combi et al., 2019
C/2002 C_1, (Ikeya-Zhang)	1	*1.5×10^4	2.0×10^{29}	Combi et al., 2019
C/2002 G_3 (SOHO)	1	*1.5×10^4	2.0×10^{29}	Combi et al., 2019
C/2002 O_4 (Hoenig)	1	*3.7×10^4	5.0×10^{29}	Combi et al., 2019
C/2002 T_7 (LINEAR)	1	*7.4×10^4	1.0×10^{30}	Combi et al., 2019
C/2002 V_1 (NEAT)	1	*7.4×10^3	1.0×10^{29}	Combi et al., 2019

Table 5.1. (continuation)

Comets	r_h [au]	I [R] @10^5 km @1 au	Q_{H2O} [/s] @1 au	Reference
C/2002 X_5 (Kudo –Fujikawa)	1	*6.6×10^3	9.0×10^{28}	Combi et al., 2019
C/2002 Y_1 (Juels –Holvorcem)	1	*7.4×10^3	1.0×10^{29}	Combi et al., 2019
C/2003 K_4 (LINEAR)	1	*3.7×10^4	5.0×10^{29}	Combi et al., 2019
C/2004 Q_2 (Machholz)	1	*4.4×10^4	6.0×10^{29}	Combi et al., 2019
C/2006 M_4 (SWAN)	1	*1.5×10^4	2.0×10^{29}	Combi et al., 2019
C/2006 P_1 (McNaught)	1	*5.2×10^4	7.0×10^{29}	Combi et al., 2019
C/2007 F_1 (LONEOS)	1	*4.4×10^3	6.0×10^{28}	Combi et al., 2019
C/2007 N_3 (Lulin)	1	*1.5×10^4	2.0×10^{29}	Combi et al., 2019
C/2009 K_5 (McNaught)	1	*1.1×10^4	1.5×10^{29}	Combi et al., 2019
C/2009 P_1 (Garradd)	1	*5.2×10^4	7.0×10^{29}	Combi et al., 2019
C/2009 R_1 (McNaught)	1	*7.4×10^3	1.0×10^{29}	Combi et al., 2019
C/2011 L_4 (PanSTARRS)	1	*7.4×10^3	1.0×10^{29}	Combi et al., 2019
C/2012 E_2 (SWAN)	1	*3.7×10^1	5.0×10^{26}	Combi et al., 2019

Table 5.1. (continuation)

Comets	r_h [au]	I [R] @10^5 km @1 au	Q_{H2O} [/s] @1 au	Reference
C/2012 F_6 (Lemmon)	1	*2.2×10^4	3.0×10^{29}	Combi et al., 2019
C/2012 K_1 (PanSTARRS)	1	*1.5×10^4	2.0×10^{29}	Combi et al., 2018
C/2012 S_1 (ISON)	1	*7.4×10^3	1.0×10^{29}	Combi et al., 2019
C/2013 A_1 (Siding Spring)	1.4	1.6×10^3	2.2×10^{28}	Crismani et al., 2018
	1.5	8.3×10^2	1.1×10^{28}	Mayyasi et al., 2020
C/2013 R_1 (Lovejoy)	1	*5.5×10^3	7.5×10^{28}	Combi et al., 2018
C/2013 US_{10} (Catalina)	0.84	1.0×10^4	3.4×10^{28}	This Dissertation
	1	*2.1×10^4	2.8×10^{29}	Combi et al., 2018
C/2013 V_5 (Oukaimeden)	1	*2.6×10^3	3.5×10^{28}	Combi et al., 2018
C/2013 X_1 (PanSTARRS)	1.45	7.7×10^3	1.5×10^{28}	This Dissertation
	1	*6.0×10^4	8.2×10^{29}	Combi et al., 2018
C/2014 E_2 (Jacques)	1	*1.1×10^4	1.5×10^{29}	Combi et al., 2018
C/2014 Q_1 (PanSTARRS)	1	3.9×10^2	5.3×10^{27}	Combi et al., 2018
C/2014 Q_2 (Lovejoy)	1	*1.7×10^5	2.3×10^{30}	Combi et al., 2018

Table 5.1. (continuation)

Comets	r_h [au]	I [R] @10^5 km @1 au	Q_{H2O} [/s] @1 au	Reference
C/2015 ER_{61} (PanSTARRS)	1.11	9.1×10^3	5.3×10^{27}	This Dissertation
C/2015 G_2 (MASTER)	1	$*3.0\times10^3$	4.1×10^{28}	Combi et al., 2018
C/2015 V_2 (Johnson)	1.65	1.8×10^4	3.8×10^{27}	This Dissertation
	1.637	$*4.0\times10^3$	2.4×10^{29}	Combi et al., 2021
C/2017 T_2 (PanSTARRS)	1.615	1.3×10^4	1.7×10^{29}	Combi et al., 2021
C/2019 U_6 (Lemmon)	1	$*9.9\times10^3$	1.4×10^{29}	Combi et al., 2021
C/2019 Y_1 (ATLAS)	1.078	$*1.6\times10^3$	2.1×10^{28}	Combi et al., 2021
C/2019 Y_4 (ATLAS)	1.054	$*1.6\times10^3$	2.2×10^{28}	Combi et al., 2021
C/2020 F_8 (SWAN)	1.055	$*5.5\times10^3$	7.5×10^{28}	Combi et al., 2021

Table 5.1. (continuation)

5.3. **Design of HI**

5.3.1. Detector

Aiming for the application of analysis methods developed in Chapters 2 and 3 to constrain particle scale lengths and to clarify nonuniformity of comae, HI is determined to take a two-dimensional images although there is also a way to make it a photometer without spatial resolution. Two options for detector systems are currently under consideration. The first is a combination of an image intensifier and CMOS camera (Murakami et al., 2016), and the second is a combination of micro-channel plate and resistive anode encoder (Yoshioka et al., 2013). Regardless of which one is adopted, the output images will consist of 256 × 256 pixels. The radius of the detector will be 12.5 mm for the image intensifier and CMOS case and 10 mm for the micro-channel plate and resistive anode encoder case. The latter case with stricter conditions is hereafter considered as nominal.

5.3.2. Basic Specifications of the Optical System

Optical telescopes are roughly divided into two categories: refracting telescopes and reflecting telescopes. Refracting telescopes have several disadvantages for UV observations such as the reduction of transmittance due to radiation rays and the difficulty of conducting performance evaluations due to the impossibility of running tests that use visible light in the air. Therefore, a reflecting-type telescope has been adopted as a basic design.

Cassegrain telescopes are reflective telescopes in which incident rays are reflected by the entrance and secondary mirrors and then focused on the detector at the back. In the HI case, the position of the entrance mirror is quite close to the aperture and the

secondary mirror to allow for the insertion of absorption cells. The performance of three mirror shapes was compared: spherical mirrors, parabolic mirrors, and 4th order non-conic mirrors. For the spherical mirrors, the radius and curvature of the entrance mirror were set to be 30 mm and -220 mm, respectively, and those of the secondary mirror are set to be 20 mm and 200 mm, respectively. The shapes of the parabolic mirror and the 4th order non-conic mirror were determined through optimization using Zemax. Parameters were optimized for each case using Zemax (Fig. 5.6) and their spot radius with an encircled energy (EcE) of 80% was compared (Table 5.2). Since smaller spot diameter means higher spatial resolution, non-conic mirrors performed the best, followed by parabolic mirrors and spherical mirrors. However, spherical mirrors can also achieve the required resolution of $0.06°$, since a spot radius of 49.8 μm

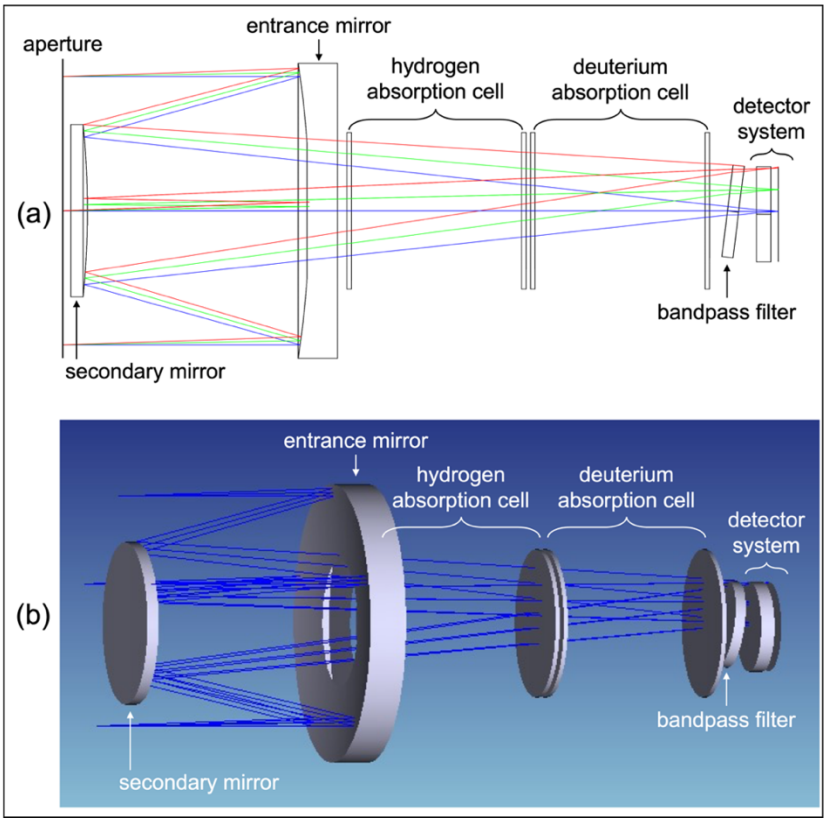

Fig. 5.6. (a) A two-dimensional layout and (b) a shaded model of Hydrogen Imager. These figures are drawn based on Zemax outputs.

	Spherical mirrors	Parabolic mirrors	4th order non-conic mirrors
Total length of optical system	159.9 mm	160.0 mm	145.6 mm
Spot radius @EcE 80%	49.8 μm	36.5 μm	28.2 μm
Expected spatial resolution	0.020°	0.015°	0.013°

Table 5.2. Comparison of performance between three types of mirrors.

corresponds to a spatial resolution of 0.02° in this optical system. Therefore, spherical mirrors are adopted considering the production cost.

5.3.3. Tolerance of the Position Error

When instruments are actually manufactured, deviations from the original design often occur. In this subsection, tolerances for manufacturing errors are evaluated. The variation of spot radii at EcE 80% when the positions or the tilts of the entrance mirror, secondary mirror, and the detector are altered is shown in Fig. 5.7. These variations are calculated using Zemax. The upper limit of allowable spot radius is set to be 75 μm (represented by orange lines in Fig. 5.7), which corresponds to 0.03°, or half of the required spatial resolution. The required accuracy for installed positions along the optical axis of both the entrance mirror and the secondary mirrors is approximately 100 μm (Fig. 5.7a,c). The required accuracy for the installed tilts of the entrance mirror and the secondary mirror is 1° (Fig. 5.7b) and 1.5° (Fig. 5.7d), respectively. When the tilt of the entrance mirror exceeds 1°, some incident rays cannot reach the detector and the

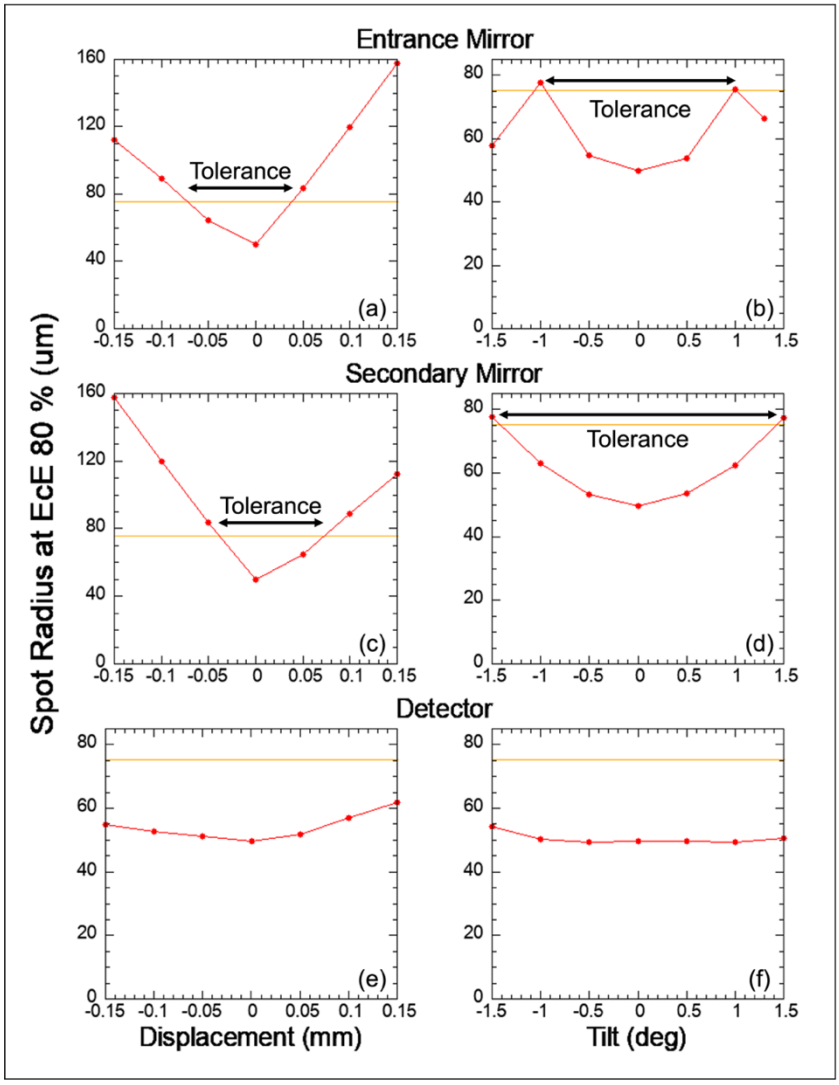

Fig. 5.7. Variation of spot radiii at an encircled energy of 80% when the positions or the tilt of the entrance mirror, secondary mirror, or detector are altered.

The orange lines represent the upper limit of allowable spot radius, 75 μm.

apparent spot radius becomes smaller. Since the position of the entrance mirror is close to both the aperture and the secondary mirror, the incident angles of rays to the detector are shallow and almost parallel to the optical axis. Therefore, the error tolerance for the installation position and tilt of the detector are very large (Fig. 5.7e,f).

5.3.4. Length of Baffles

To reduce stray light, it is necessary to prevent light from entering the detector without reflecting off of mirrors. In this subsection, I consider the required lengths of baffles, when baffles are made by the extension of mounts of the entrance mirror and secondary mirror mounts.

In the current design discussed in Subsection 5.3.2, some of the incident rays entering from the aperture reach the detector without hitting the mirrors. To completely block this path, lengths of baffles are determined to ensure that the edge of the detector and the edges of the baffles extended from the mounts of the entrance and secondary mirror are aligned (Fig. 5.8). There is one degree of freedom in the lengths of baffles, and the relationship between required lengths of the entrance mirror baffle and the secondary mirror baffle is as shown in Fig. 5.9. Since there is little difference in effective areas in either case, as will be discussed in the following subsection, the intermediate values of a 4 mm entrance mirror baffle and a 5.8 mm secondary mirror baffle was adopted in this time.

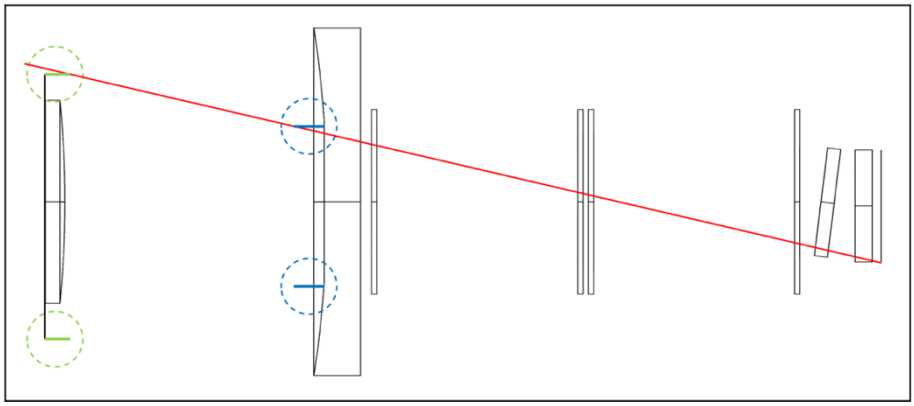

Fig. 5.8. Schematic representation of baffles.
Entrance mirror baffles (blue lines encircled by blue circles) and secondary mirror baffles (green lines encircled by green circles) prevent rays (red line) from entering the detector without mirror reflection.

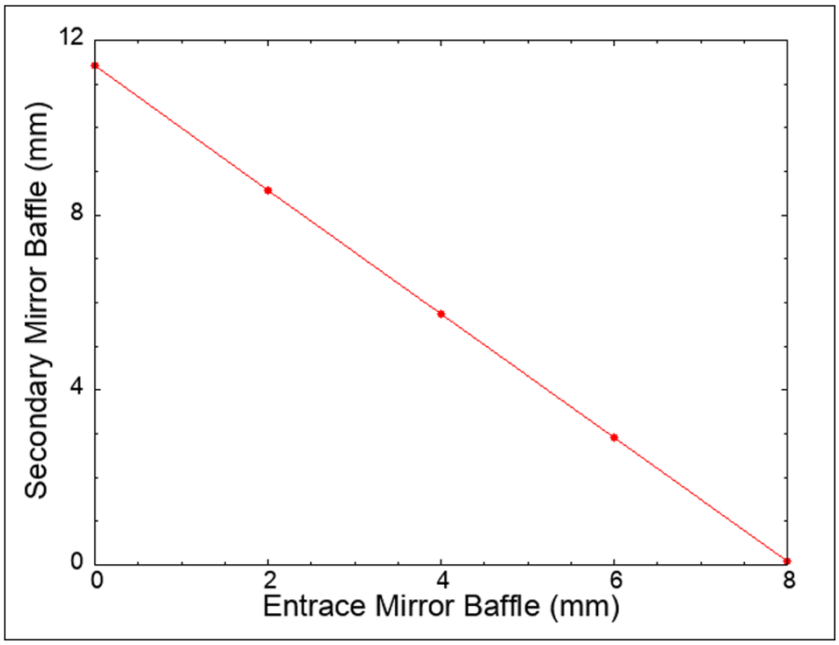

Fig. 5.9. Relationship between required lengths of entrance mirror baffle and secondary mirror baffle.

5.3.5. Calculation of Geometrical Effective Area

Since some rays are shaded by baffles and cannot reach the detector, baffles make the effective area smaller. I reproduce the progression of the rays in the optical system and evaluate effective area as a function of viewing angle using the Monte–Carlo method. The results are shown in Fig. 5.10. Effective areas are constant within the incident angle of 1°, gradually decrease until 1.9°, and sharply drop after that. This means that the field of view of this optical system is ±1.9°, or 3.8°. The geometrical effective area, which is the effective area assuming 100% efficiency of the transmittance of filters, reflectance of mirrors, and quantum detection, is 9.8 cm^2 at the viewing angle of 0°.

It was found that incident rays from the viewing angle between 2.5° and 4.7° unintentionally reach the detector after being reflected several times between the

entrance mirror and the secondary mirror. This component is thinly spread over the entire detector without being focused, and is further diminished by reflectance of the mirrors. The rays reflected multiple times between mirrors are detected at a rate less than 3% of the rate of the rays reflected between mirrors only once.

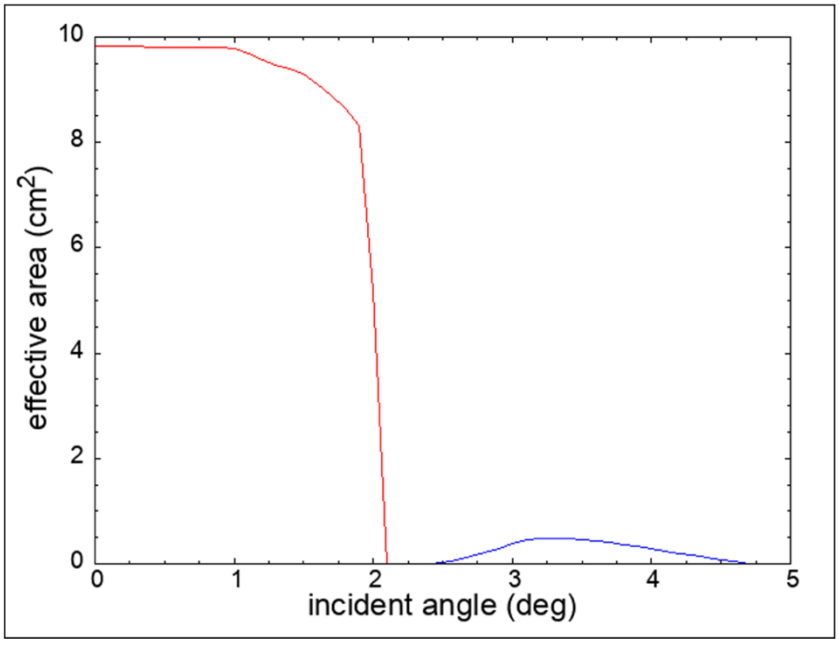

Fig. 5.10. Calculated effective areas as a function of incident angle.

The red line represents the number of photons that are correctly reflected by the entrance and secondary mirrors and enter the detector. The blue line represents the number of photons that are reflected between the mirrors several times before entering the detector.

5.4. **Measurement of Transmittance of the Band-pass Filters and Reflectance of Mirrors**

In calculations of the effective area of HI, performance evaluation of the BPF and mirrors installed in HI is necessary. In this section, experiments to measure transmittance of the BPF and reflectance of the mirrors used in BBM conducted in the beam line of BL5B at UV synchrotron radiation facility named UVSOR in Aichi-Prefecture, Japan are described.

5.4.1. Settings

Settings of the apparatus are shown in Fig. 5.11. Fig. 5.11a is an image of the inside of the vacuum chamber used in the experiment. The left side of the chamber is connected to the synchrotron, and the UV rays passed through a spectrometer are supplied from there. For the case of this beamline, spectral resolution is approximately 1 nm. The BPF used for the BBM of HI is installed on a gimbal on the left side, and the mirror used for the BBM and a photodiode (PD) are set on a gimbal on the right side.

According to the measurement conditions, position and angle of each device are moved as shown in Fig. 5.11b-d. In the case of measurement of BPF's transmittance, the mirror is always removed from the light path. Then, transmittance spectra of BPF is calculated from the ratio of those obtained with the BPF in the light path (called "filter in": Fig. 5.11c) to spectra obtained when the BPF is also away from the light path (called "direct": Fig. 5.11b). On the other hand, the BPF is always away from the light path, in the case of the measurement of mirror's reflectance. Reflectance spectra of mirror are spectra obtained when incident light is reflected by mirror and enter the PD (called "mirror in": Fig. 5.11d) divided by "direct" measurement. After measuring dark

current, I measure in “direct” condition once, “filter (mirror) in” condition three times, dark current once again, and finally “direct” condition once again. The reflection angle of the mirror is set to be 5° since it is the minimum reflection angle where the PD does not block the optical path.

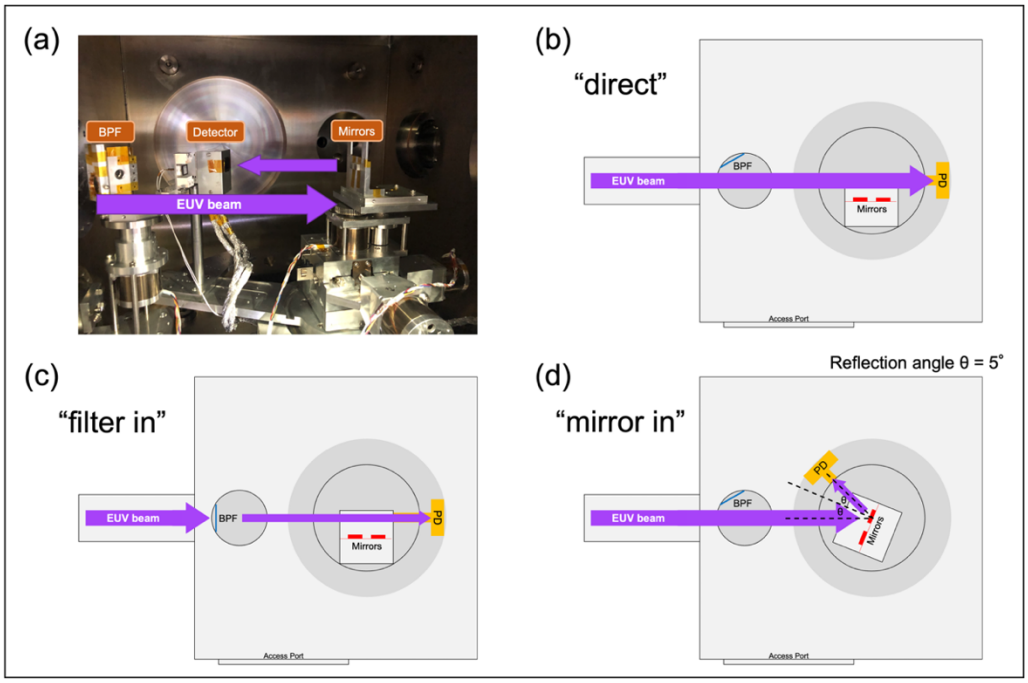

Fig. 5.11. Settings of experiments.

(a) A picture of inside of the vacuum chamber used in the experiment.

(b)-(d) Schematic images of settings in each condition.

5.4.2. Results

Measurement results of BPF’s transmittance and mirror’s reflectance are shown in Figs. 5.12 and 5.13, respectively. In both figures, (a) and (b) show the obtained spectra under the “direct” and “filter (mirror) in” conditions, and (c) are the transmittance (reflectance) spectra. When measuring the reflectance of mirror, pinhole attached to the upstream fell during the second “direct” measurement and only one

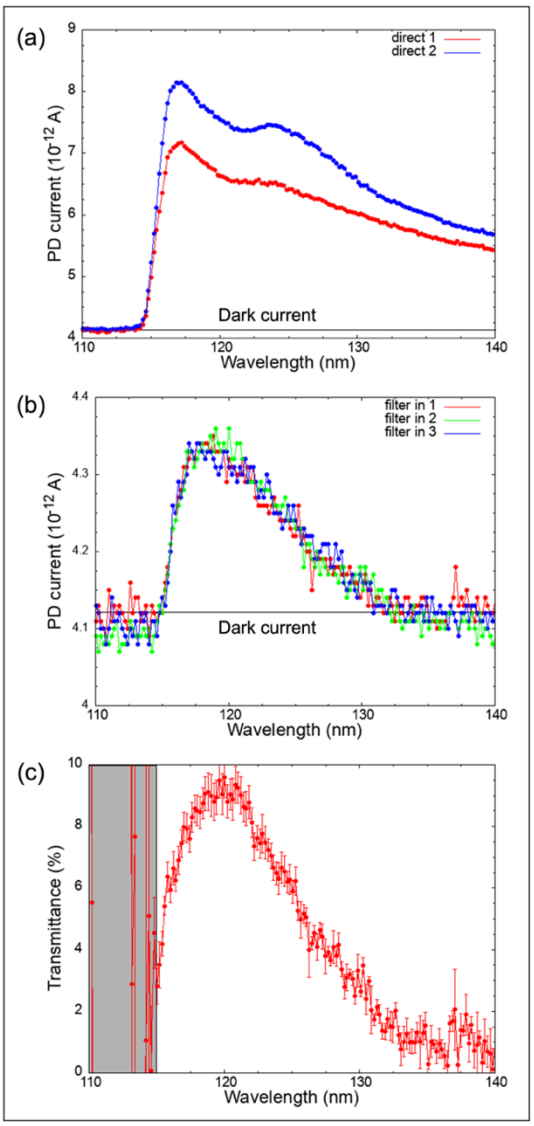

Fig. 5.12. Results of the experiment to measure the transmittance of the band-pass filter.

(a) Spectra of incident beam. (b) Spectra of transmitted rays. (c) Transmittance spectra of the band-pass filter.

Transmittance below the wavelength of 115 nm is meaningless since it is below the cutoff wavelength of the MgF_2 filter.

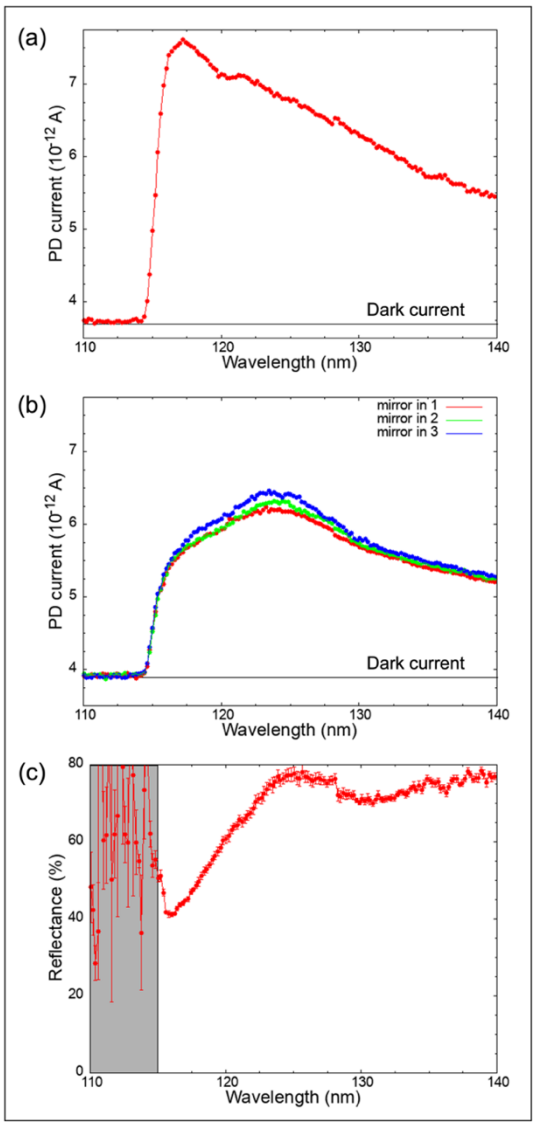

Fig. 5.13. Results of the experiment to measure the reflectance of the mirrors.

(a) Spectra of incident beam. (b) Spectra of reflected rays. (c) Reflectance spectra of the mirrors.

Transmittance below the wavelength of 115 nm is meaningless since it is below the cutoff wavelength of the MgF_2 filter.

	NI1168	HI1216	OI1304
Transmittance of the BPF (%)	8.6 ± 0.5	8.6 ± 0.5	2.4 ± 0.5
Reflectance of the mirror (%)	49 ± 1	67 ± 1	71 ± 1
Total effective area ratio (HI1216 ≡ 1)	0.53± 0.05	1	0.32± 0.07

Table 5.3. Summary of the results of the experiments.

Total effective area ratio is the ratio of transmittance × reflectance^2.

"direct" data are obtained. Variation of "direct" is within ±10% and does not significantly affect results. Note that transmittance spectra and reflectance spectra below the wavelength of 115 nm are not meaningful since cutoff wavelength of MgF_2 filter used in the experiment is approximately 115 nm. As shown in Table 5.3, BPF's transmittance is 8.6 ± 0.5% and mirror's reflectance is 67 ± 1%. On the other hand, at 117.8 nm and 130.4 nm, transmittance is 8.6 ± 0.5% and 2.4 ± 0.5%, and reflectance is 49 ± 1% and 71 ± 1%, respectively. This means that the ratio of effective areas, calculated from product of transmittance and squared reflectance, at the wavelength of 116.8 nm, 121.6 nm, and 130.4 nm is 0.53 : 1 : 0.32. It would be better if the transmittance of the BPF at 130.4 nm could be reduced by nearly half by making the peak wavelength of transmittance shorter to relatively lower the transmittance at 130.4 nm. The iteration and improve the performance will be continued.

As described in Subsection 5.3.5, geometrical effective area against incident rays with the viewing angle of 0° is 9.8 cm^2. The quantum efficiency is approximately 3% (Yoshioka et al., 2013), and transmittance of MgF_2 window of absorption cells with 1

mm thickness is approximately 55% (Kuwabara et al., 2018a), although they are not measured in this study. Combining these results, effective area of the HI BBM is calculated to be 1×10^{-3} cm^2, which satisfies the required performance estimated in Subsection 5.2.3.

5.5. **Performance Evaluation of Hydrogen Absorption Cells**

The absorption rate of hydrogen and deuterium Ly-α rays by absorption cells depends on the temperature of the filament, the pressure of the contained hydrogen (deuterium), and the position of the incident rays. Since this dependency varies with cell shape and filament material, it is necessary to measure transmittance and parameters such as filament temperature and hydrogen pressure should be optimized for each cell.

To investigate absorption spectra of cells, a detector system with quite a high wavelength resolution is required. Therefore, experiments at the UV synchrotron radiation facility named SOLEIL in France, which uses a Fourier Transformation Spectrometer (FTS) to achieve an ultrahigh wavelength resolution (Oliveira et al., 2011) are conducted.

5.5.1. Settings

Settings of the apparatus are shown in Fig. 5.14. Fig. 5.14a is an image of the inside of the vacuum chamber used in the experiment. The left side of the chamber is connected to the synchrotron, and the UV rays are supplied from there. The right side of the chamber is connected to the FTS, whose spectral resolution is approximately 0.4 pm (Oliveira et al., 2011). The absorption cell is installed at the center of the chamber.

Voltage can be applied to filaments from outside the chamber via conducting wires.

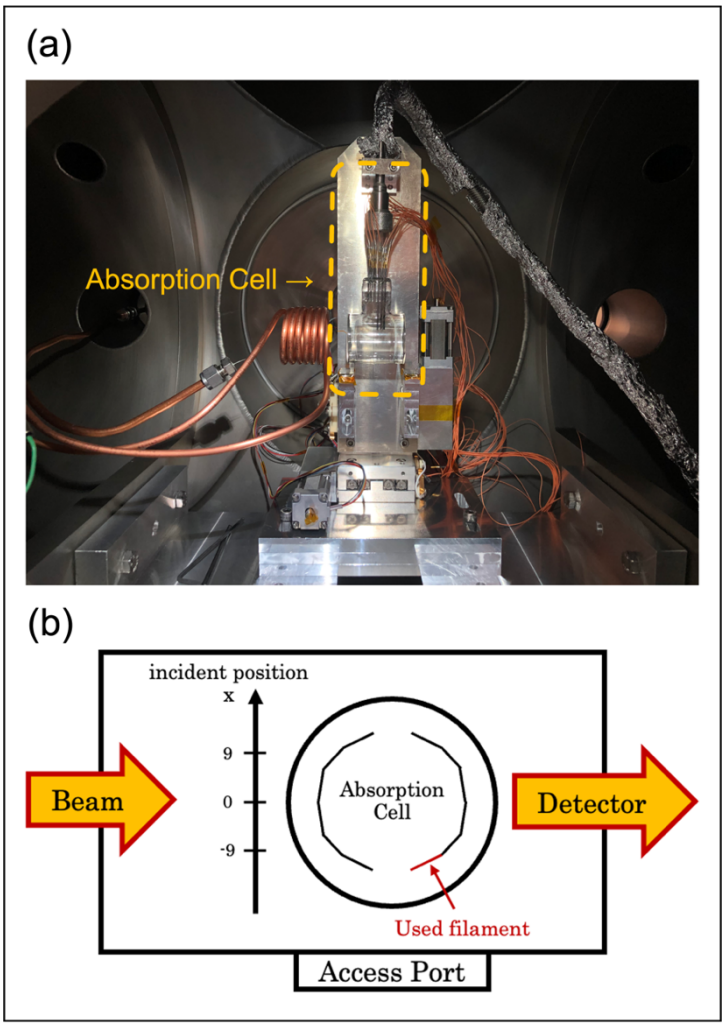

Fig. 5.14. Settings of the experiments.

(a) A picture of inside of the vacuum chamber used in the experiment.

(b) Schematic representation of the settings.

Since the resistivity of tungsten filaments is uniquely determined by temperature, filament temperature can be conversely estimated by measuring applied voltage and flowing current. In this study, resistivity ρ [Ω/m] is converted to temperature T [K] using the following equation based on the experimental results of Lide, 1994 (Fig. 5.15):

$$T = -6.42 \times 10^{14}\rho^2 + 3.7858 \times 10^{9}\rho + 71.279 \qquad (5.1)$$

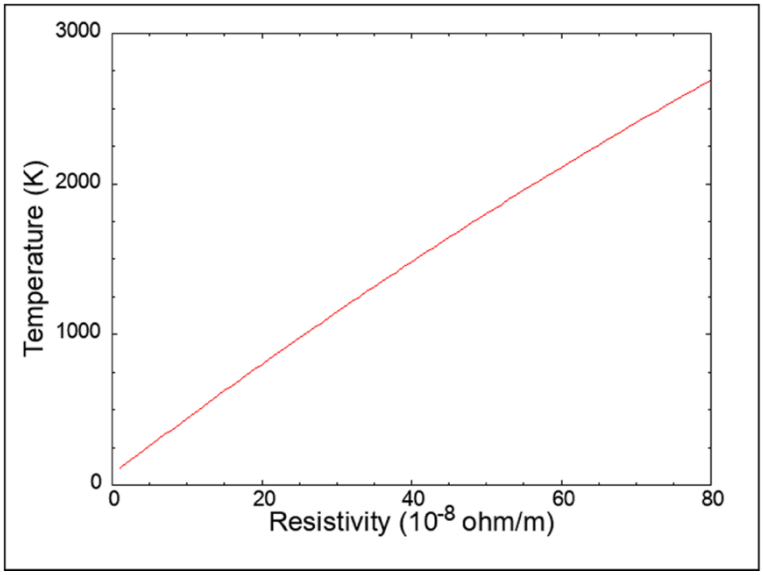

Fig. 5.15. Tungsten filaments' temperature as a function of resistivity.

Examples of obtained data are shown in Fig. 5.16 as red lines. Optical thickness at the line center τ_0, hydrogen temperature in the cell T, and incident synchrotron radiation I_0 are deduced by fitting the spectra $I(\lambda)$ calculated using the following equation (Kuwabara et al., 2018b) on the obtained data within a wavelength range of 121.567 ± 0.004 nm:

$$I(\lambda) = \frac{\int d\lambda' I_{ideal}(\lambda')\Gamma(\lambda - \lambda')}{\int d\lambda' \Gamma(\lambda - \lambda')} \tag{5.2}$$

$$I_{ideal}(\lambda') = I_0 \, exp\left\{-\tau_0 \, exp\left[-\left(\frac{\lambda - \lambda_0}{\Delta\lambda}\right)^2\right]\right\} \tag{5.3}$$

$$\Gamma(\lambda) = \frac{sin\left(\pi \times 1.2 \times \frac{\lambda}{\Delta\lambda_{FTS}}\right)}{\pi \times 1.2 \times \frac{\lambda}{\Delta\lambda_{FTS}}} \tag{5.4}$$

where $\lambda, \Delta\lambda$ and $\Delta\lambda_{\mathrm{FTS}}$ are wavelength, Doppler width of hydrogen (deuterium) in the cell, and full width at half maximum of the sinc function caused by the FTS finite optical path, respectively. $I_{\mathrm{ideal}}(\lambda')$ is the spectra calculated from Beer-Lambert law and $\Gamma(\lambda)$ is FTS instrumental function. Model function $I(\lambda)$ is calculated from the

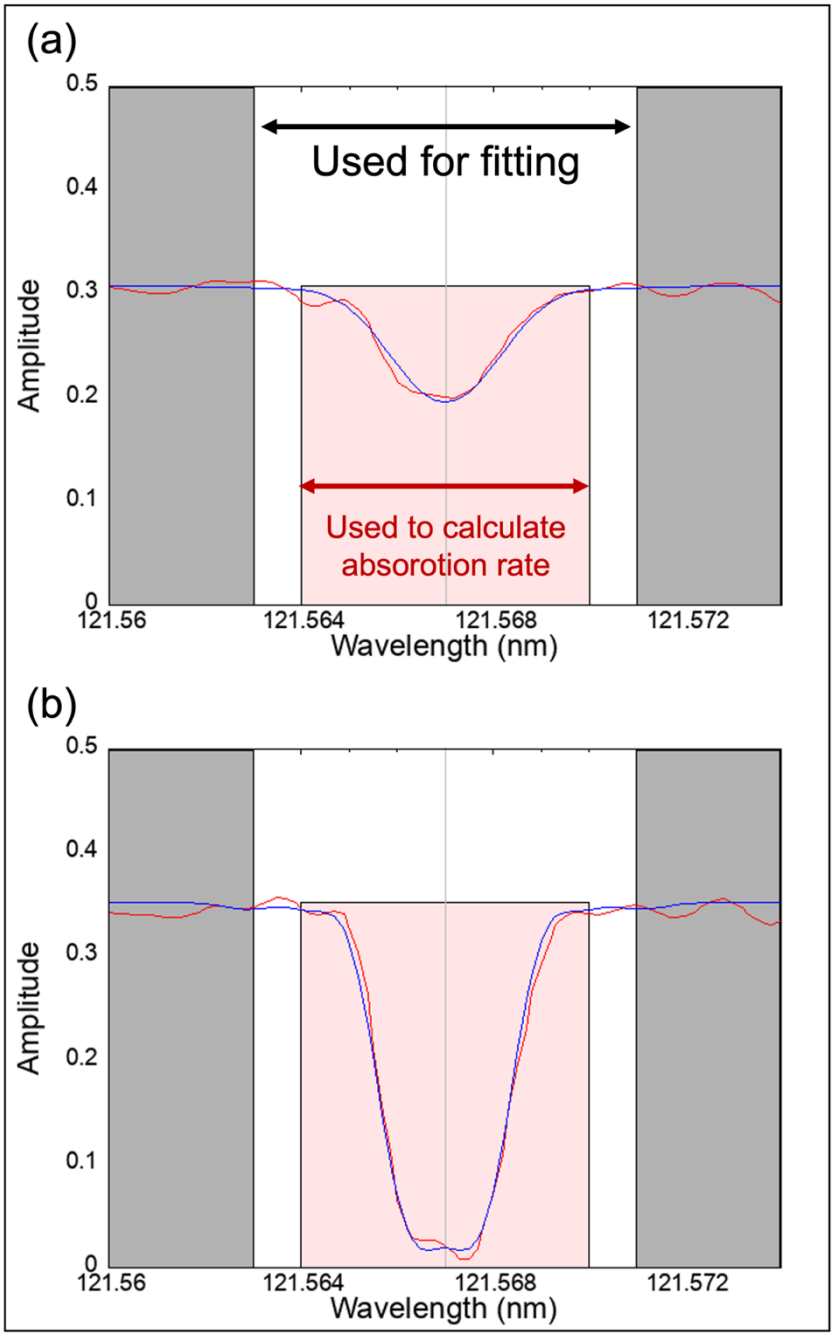

Fig. 5.16. Examples of obtained spectra (red lines) and fitted spectra (blue lines) for (a) an optically thin case and (b) optically thick case.

The spectra within the wavelength range of 121.567 ± 0.004 nm are used for fitting, and those within 121.567 ± 0.003 nm are used to calculate of absorption rate.

convolution of $I_{\mathrm{ideal}}(\lambda')$ and $\Gamma(\lambda)$. Examples of fitted spectra are shown in Fig. 5.16 as blue lines. When optically thin, larger τ_0 values deepen the dip due to the absorption deeper, while larger T values result in wider absorption lines. However, when optical thickness gets larger, both τ_0 and T work to widen absorption lines, making it hard to individually evaluate the parameters by fitting. Then, the absorption rate n within the wavelength range of 121.567 ± 0.003 nm (red regions in Fig. 5.16) is defined by following equation and is used in the comparison of performance of the absorption cell:

$$n = 1 - \int_{121.564\ nm}^{121.570\ nm} d\lambda \frac{I(\lambda)}{I_0} \tag{5.5}$$

The measurement conditions are organized in Table 5.4.

Conditions	H_2	D_2
Temperature dependence	1400 < T < 2000 K (100 K step)	1600 < T < 2000 K (100 K step)
Pressure dependence	200 < P < 600 Pa (100 Pa step)	200 < P < 400 Pa (100 Pa step)
Incident position dependence	-9 < X < 9 mm (4.5 mm step)	-9 < X < 9 mm (4.5 mm step)

Table 5.4. Summary of measurement conditions.

Parameters are fixed at T=1800 K, P=300 Pa, and X=0 mm except for the parameters to be changed.

5.5.2. Results

The results are summarized in Figs. 5.17–5.19.

As the temperature of the filament in the cell increases, the absorption rate also increases (Fig. 5.17a). This is because higher thermal energies supply

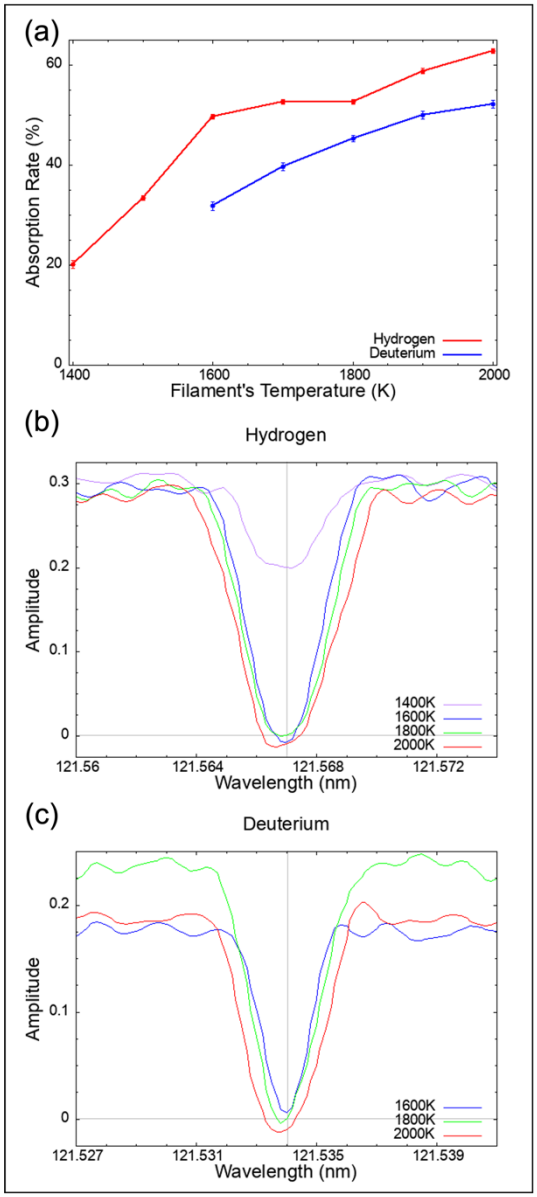

Fig. 5.17. (a) Dependence of absorption rate on filament's temperature. (b) Variation of absorption spectra of the hydrogen cell and (c) that of deuterium cell when filament's temperature is changed.

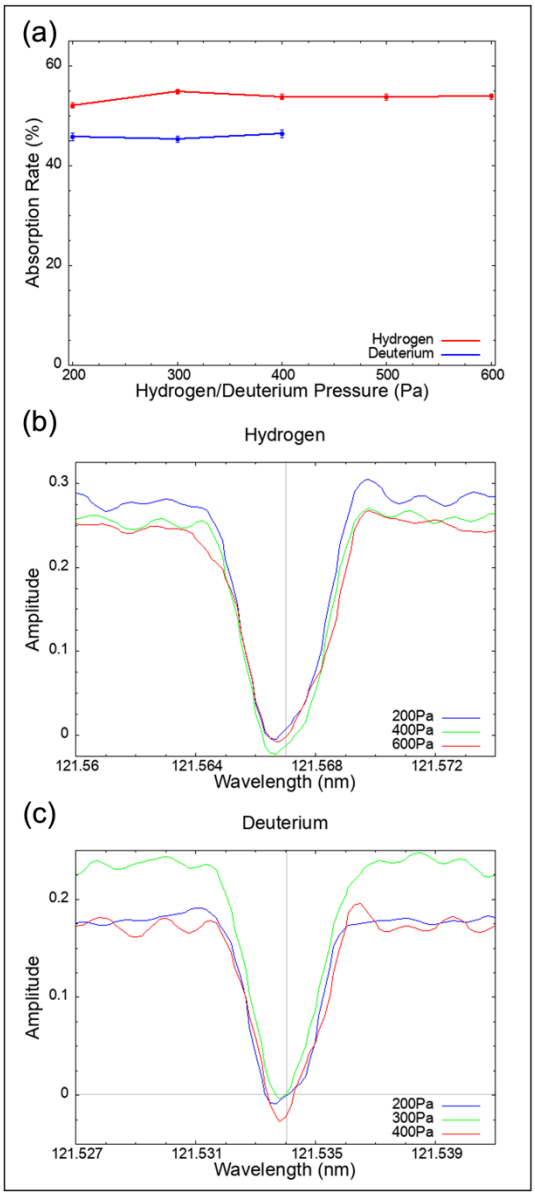

Fig. 5.18. (a) Dependence of absorption rate on gas pressure. (b) Variation of absorption spectra of the hydrogen cell when hydrogen pressure is changed and (c) that of deuterium cell when deuterium pressure is changed.

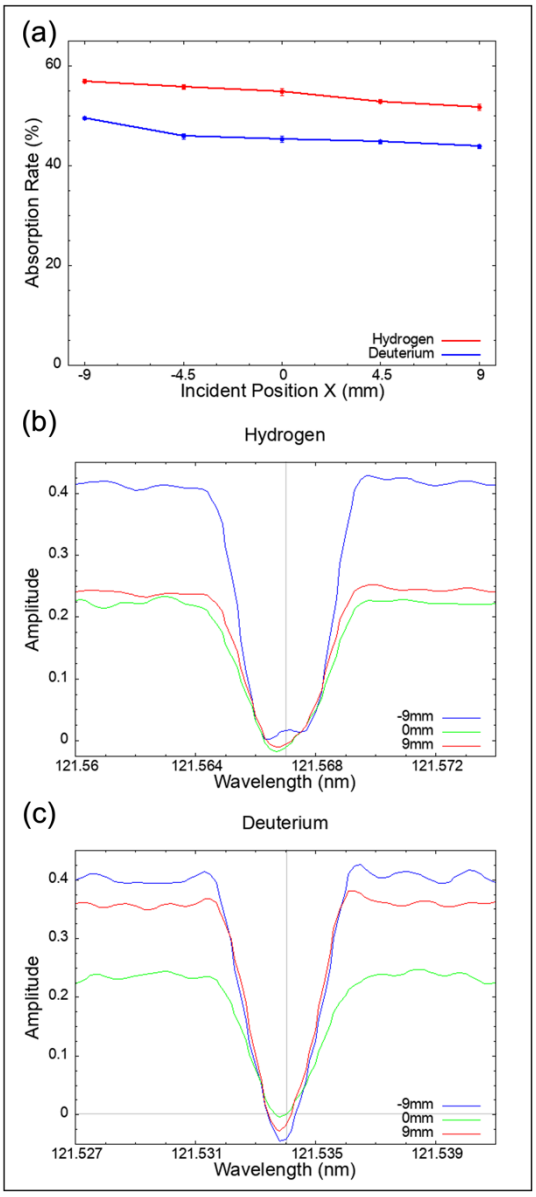

Fig. 5.19. (a) Dependence of absorption rate on incident position.

(b) Variation of absorption spectra of the hydrogen cell and

(c) that of deuterium cell when the incident position is changed.

hydrogen/deuterium molecules, resulting in the higher dissociation rate. For the hydrogen cell case, when filament's temperature exceeds 1600 K, the increase rate of absorption rate decreases. As shown in the spectra of Fig. 5.17b, the absorption rate at the line center reaches nearly 100%, and absorption gets saturated over the temperature of 1600 K. Since the lifetime of filaments becomes shorter with higher temperature, it is best to set the filament temperature to 1600 K when observing comets with HI.

Even when the pressure of hydrogen or deuterium changes, absorption rate hardly varies (Fig. 5.18a). This is considered to be due to the fact that higher hydrogen pressure causes a larger number of hydrogen atoms to dissociate, but simultaneously makes it harder for them to diffuse in the cell. Increased pressure increases the power consumption required to achieve a given temperature. On the other hand, absorption rate gets lower with further lowered pressure since the number of dissociated hydrogen atoms decreases (Kuwabara et al., 2018b). Therefore, a pressure of 300 Pa has been adopted as a nominal value. The dependence of absorption rate on the incident position is shown in Fig. 5.19a. For the hydrogen cell, absorption rates at X = -9 mm and 9 mm are 57% and 52%, respectively, and for the deuterium cell, they are 50% and 44%. Since the lighted filament is located near X = -9 mm as shown in Fig. 5.14, these results mean that absorption rate decreases as incident rays move away from the filament. As a different issue, absorption rates have an absolute error of approximately 8% depending on the temperature of hydrogen/deuterium in the coma for comets observed using cells, which is discussed in Subsection 5.5.3. Regarding the incident position dependence of absorption, we need to calibrate the effective area during the approach phase.

5.5.3. Absorption Rate as a Function of Hydrogen Temperature in Comae

In Subsection 5.5.2, absorption rate is defined simply as $\int \mathrm{d}\lambda\, I(\lambda)/I_0$ to compare cell performances. In reality, however, it varies depending on the hydrogen/deuterium temperatures (width of emission lines) of the target in reality. In this subsection, I investigate dependence of the absorption rate on the hydrogen/deuterium temperature when filament's temperature and hydrogen/deuterium pressure are set to be 1600 K and 300 Pa, respectively.

Fig. 5.20a shows the absorption spectrum of a hydrogen absorption cell with the filament temperature of 1600 K and hydrogen pressure of 300 Pa, and the Ly-α emission spectra of hydrogen whose temperatures are 400, 2,000, and 10,000 K in comae of comets. As hydrogen temperature rises, emission lines broaden and the number of rays with the wavelengths outside the absorption range of the cell increases. Therefore, the higher the hydrogen temperature of the target is, the lower the absorption rate of the cell becomes (Fig. 5.20b). This means that the absolute value of the absorption rate will have a systematic error during the observations unless the hydrogen/deuterium temperature of the target is identified. For example, the absorption rates of hydrogen and deuterium are 35 ± 4% (the relative error of 13%) and 41 ± 5% (the relative error of 12%) assuming that the hydrogen temperature is within 7,000 ± 2,000 K and the deuterium temperature is 3,500 ± 1,000 K referring to Weaver et al. (2008) and Tenishev et al. (2008). It is possibe that hydrogen temperature can be measured during the CI mission (see Appendix 5.A1), although measurement of deuterium temperature is not realistic.

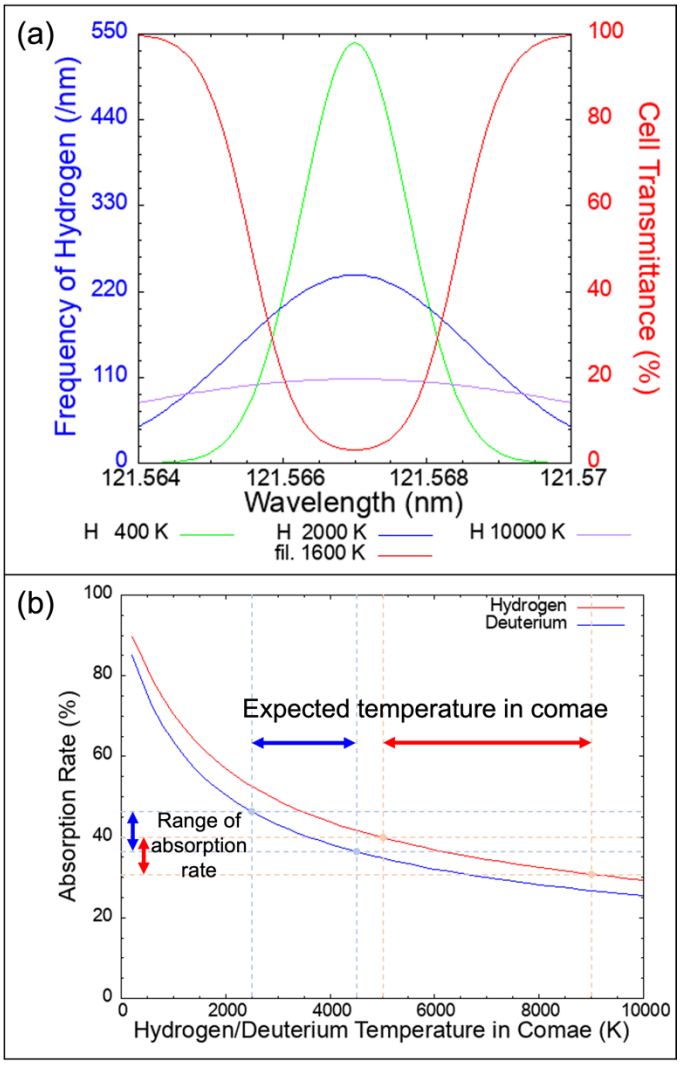

Fig. 5.20. (a) Examples of hydrogen's Ly-α spectra in comae as a function of hydrogen temperature (green, blue, and purple lines) and the absorption spectrum of the hydrogen cell (red line). (b) Dependence of absorption rate on hydrogen/deuterium temperature in comae.

5.6. **Summary**

I evaluated the required performance of CI/HI (Section 5.2), optimized the optical system (Section 5.3), and investigated the performance of the band-pass filter, mirrors, and absorption cells used in the BBM (Sections 5.4 and 5.5). Table 5.5 summarizes the required performance and BBM's performance. It can be said that BBM achieved the requirement overall. Although there will be no problem with adopting the current BPF, it is possible to further reduce the contamination of oxygen emission by making the peak wavelength of transmittance shorter to relatively lower the transmittance at 130.4 nm.

	Required	BBM
Field of view	3.8° (Subsection 5.2.1)	3.8° (Subsection 5.3.2)
Spatial resolution	0.06° (Subsection 5.2.1)	0.02° (Subsection 5.3.2)
Transmittance of the BPF	OI1304 / HI1216 < 0.2 (Subsection 5.2.2)	OI1304 / HI1216 = 0.32 (Subsection 5.4.2)
Wavelength resolution of the absorption cell	16 pm (Subsection 5.2.2)	6 pm (Subsection 5.2.1)
Effective area	6×10^{-4} cm^2 (Subsection 5.2.3)	1×10^{-3} cm^2 (Subsection 5.4.2)

Table 5.5. Comparison of the required performance and the performance of the bread board model.

6. Feasibility of Measurement of D/H Ratio Using Hydrogen Imager Onboard Comet Interceptor

As described in Subsection 1.3.5 and Subsection 5.1.3, we will optically observe the D/H ratio of long-period comets using absorption cells installed in CI/HI. In this chapter, the feasibility study of the D/H ratio measurement by HI is conducted through combining the numerical cmputation constructed in Chapter 4, and the results of optical design and performance evaluation experiments described in Chapter 5.

6.1. Required performance

As summarized in Tables 1.8 and 1.9, D/H ratios of comets measured so far are between $(1.61\pm0.24) \times 10^{-4}$ (103P/Hartley 2) and $(5.3\pm0.7) \times 10^{-4}$ (67P/CG). It is sufficient to measure the D/H ratio with a 30% relative error by HI to determine in three stages whether the D/H ratio is close to the that of the ocean of the Earth, as high as that of 67P/CG, or intermediate. As mentioned in Subsection 5.2.3, expected Ly-α radiance range at an altitude of 10^5 km is 10^3–10^5 R. In this chapter, I describe the feasibility of the D/H ratio measurement for comets with a D/H ratio between 1×10^{-4} and 1×10^{-3} and a brightness between 1×10^3 and 1×10^5 using absorption cell installed in HI.

6.2. Generation of Simulated Observational Data

The radiative transfer model constructed in Chapter 4 assumed the case of observations by the Hisaki satellite sufficiently far from the target (Fig. 6.1a). As can be seen from Fig. 6.1, in the case of Hisaki, rays reaching the observer are the sum of ones ejected from both the optically thin and thick region when the impact parameter is

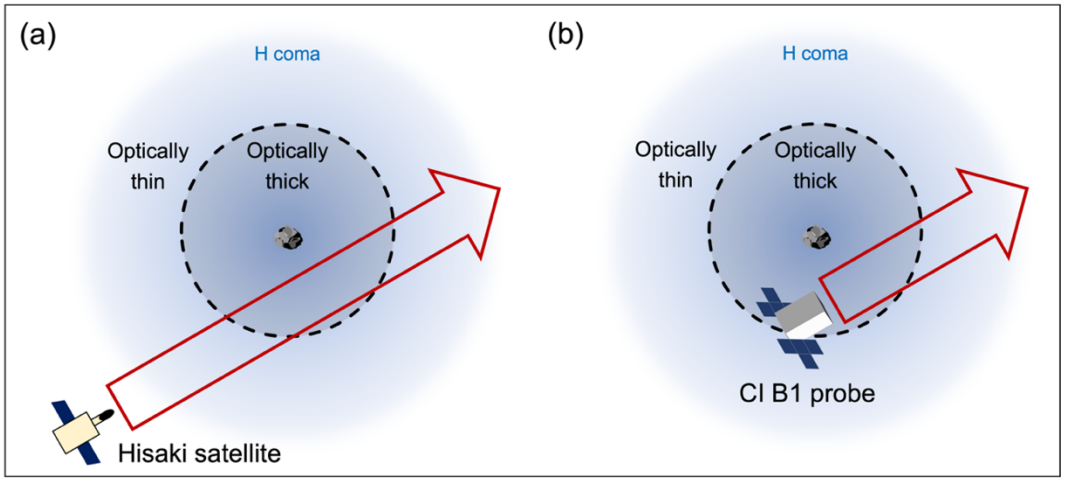

Fig. 6.1. Comparison of Hisaki/EXCEED and CI/HI position and the line of sight.

small. Alternatively, the expected Ly-α radiance obtained by the HI observations from the "inside" of the hydrogen coma (Fig. 6.1b) is depicted in Fig. 6.2. The red, green, and blue lines represent computed brightness for the HI case with the water production rate of 10^{27}, 10^{29}, and 10^{31} /s, respectively. In the case of HI observations, all the rays entering the instrument must have passed through the optically thick region. Therefore, Ly-α radiance decreases in the optically thick region, unlike the case of Hisaki (Fig.

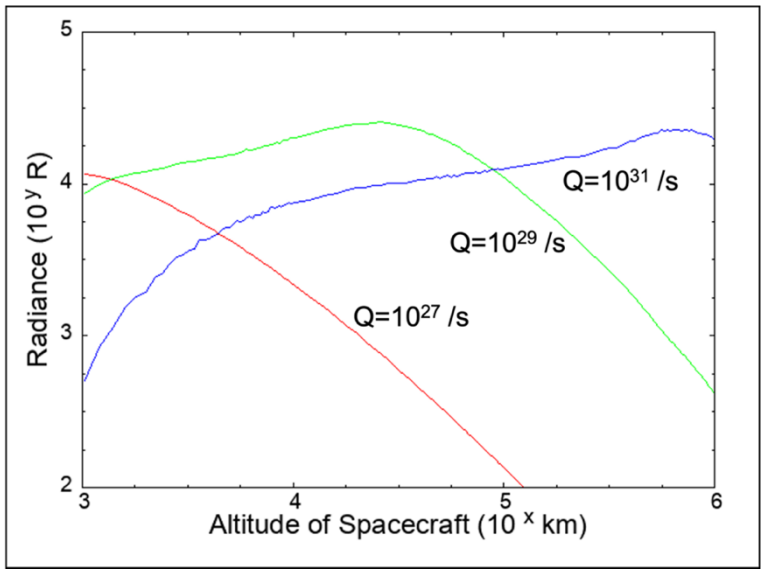

Fig. 6.2. Expected Ly-α radiance profile observed by HI during the comet fly-by phase.

4.4).

6.3. **S/N Ratio for Measuring Deuterium Lyman Alpha Radiance**

Using the effective area of HI calculated in Chapter 5, 1×10^{-3} cm^2, the number of signal counts detected by HI during the comet fly-by phase is calculated as shown in Fig. 6.3. This figure demonstrates the results only for a water production rate of 10^{29} /s and a D/H ratio of 1×10^{-4}. The red line in Fig. 6.3 is expected signal count from hydrogen atoms computed from the Ly-α radiance distribution of hydrogen (the green line in Fig. 6.2). The blue one is expected signal from deuterium. Radiance of deuterium Ly-α is calculated by multiplying hydrogen atom column density, D/H ratio, and coefficient $g/10^6$. Here, g is g-factor calculated assuming single scattering, which coincides with effective g-factor when the product of water production rate and D/H ratio is below approximately 10^{27} /s. Among the parameter survey conducted in this chapter, deuterium Ly-α may also be optically thick when water production rate is very

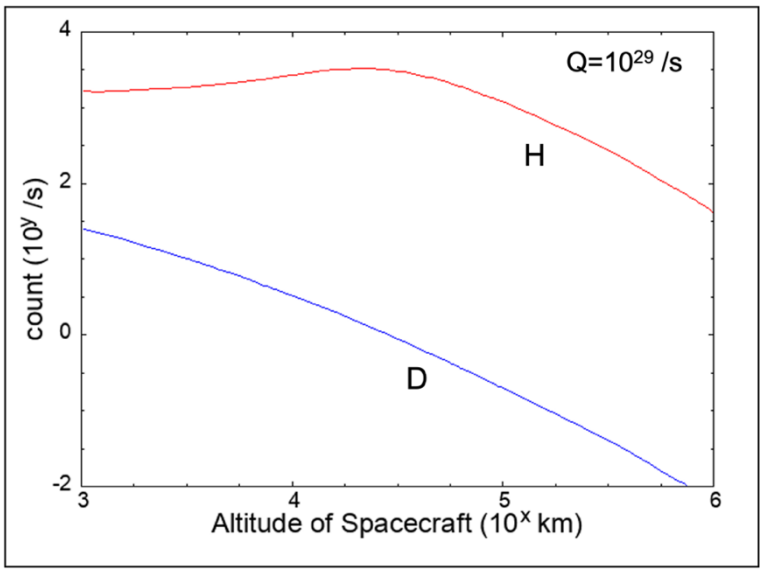

Fig. 6.3. Expected detected signal counts derived from hydrogen (red line) and deuterium (blue line) during the comet fly-by phase.

high and D/H ratio is particularly high. However, since, in these cases, the Ly-α radiance of hydrogen and deuterium is bright and S/N ratio is expected to be higher than other cases, much attention does not need to be paid this time.

The simulated data during the comet fly-by phase is shown in Fig. 6.4. This is generated by the random component by shot noise incorporated to the sum of signal counts due to Ly-α emission from cometary hydrogen, cometary deuterium, and interplanetary medium, to the dark noise, and to the radiation noise. Data in Fig. 6.4 were the case of observations with the hydrogen cell always turned on and the deuterium cell switched on and off every two seconds. Setting of the switching interval is discussed in detail in Appendix 6.1. The red and blue points in Fig. 6.4 represent data obtained when the voltage is applied and not applied to the filament in the deuterium

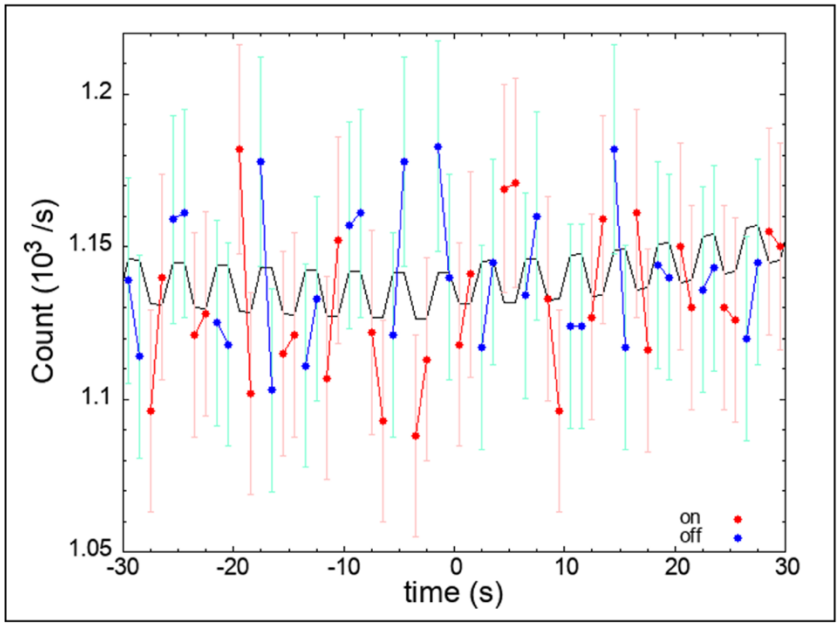

Fig. 6.4. An example of simulated data obtained by HI during the comet fly-by phase. The red and blue points represent data obtained when the voltage is applied and not applied to the filament in the deuterium cell. The black line depicts the ideal data with no errors.

cell.

Radiance of Ly-α emission of deuterium can be quantified when measured data with the deuterium cell on are subtracted from those with the deuterium cell off, and the result is divided by the deuterium cell absorption rate. When the expected difference between the number of counts when the deuterium cell is on and off is regarded as a signal and the variation associated with the shot noise is regarded as a noise, the S/N ratio for detecting deuterium can be evaluated by the following equation:

$$S/N\ ratio = \frac{n_{D-off} - n_{D-on}}{\sigma_{count}} = \frac{n_{D-off} - n_{D-on}}{\sqrt{n_{D-off}}} \quad (6.1)$$

where $n_{\mathrm{D-off}}$ and $n_{\mathrm{D-on}}$ are counts with the deuterium cell off and on, and σ_{count} is the standard deviation of the shot noise. Fig. 6.5 depicts the frequency distribution of water production rates observed in the past and the S/N ratios when integrating data for 300 seconds before and after the closest approach assuming comets with a variety of water production rates and D/H ratios. Deuterium brightness can be quantified for most comets, except the cases that the water production rate is as small as approximately 10^{27} /s. When a comet with such low activity is determined as a target, the filament temperature will be set to 1800 K, with which deuterium can be detected. Note that the detection itself can be conducted with a high S/N ratio, but that deduced deuterium column density has a relative error of 12% due to the relative error of absorption rate, 12%, as described in Subsection 5.5.3.

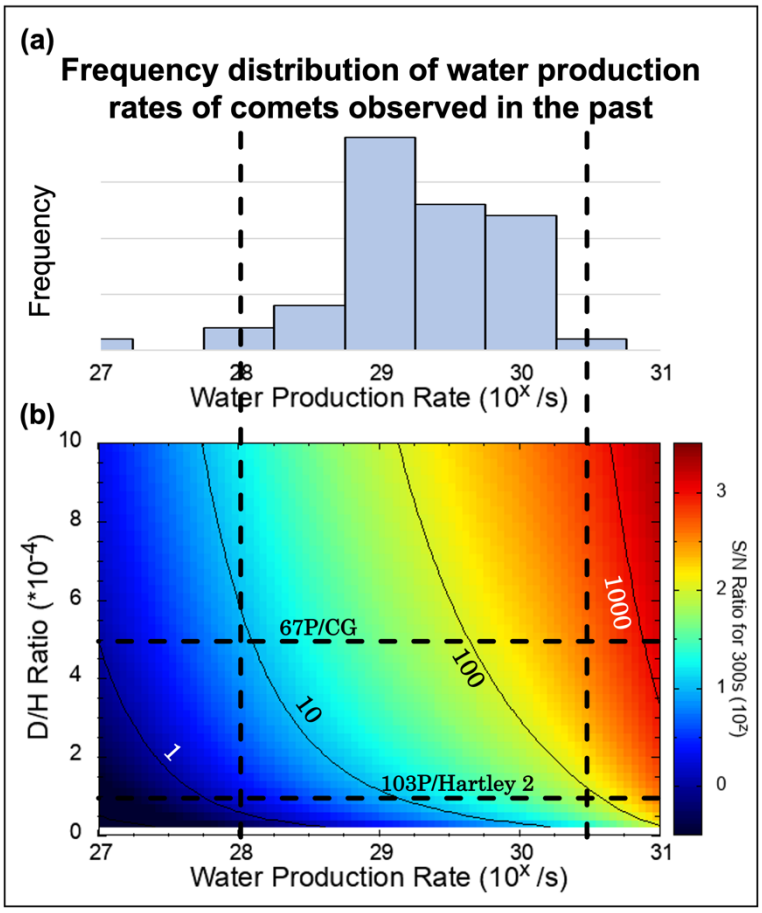

Fig. 6.5. (a) Histogram of water production rates reported in previous studies and (b) expected S/N ratio in deuterium Ly-α emission detection.
(a) is the same as Fig. 5.5(b).

6.4. **Accuracy Evaluation for Estimating D/H Ratio**

In this subsection, the accuracy of D/H ratio estimation using HI is computed. To obtain D/H ratio, it is essential to compute column density of hydrogen and deuterium.

The estimation accuracy of deuterium brightness is 12%, which corresponds to the relative error of the absorption rate of the deuterium absorption cell. In the case of the operation, wherein the hydrogen cell is always turned off during the comet fly-by phase, the estimation accuracy of hydrogen radiance depends on the calibration accuracy, which is approximately 10%.

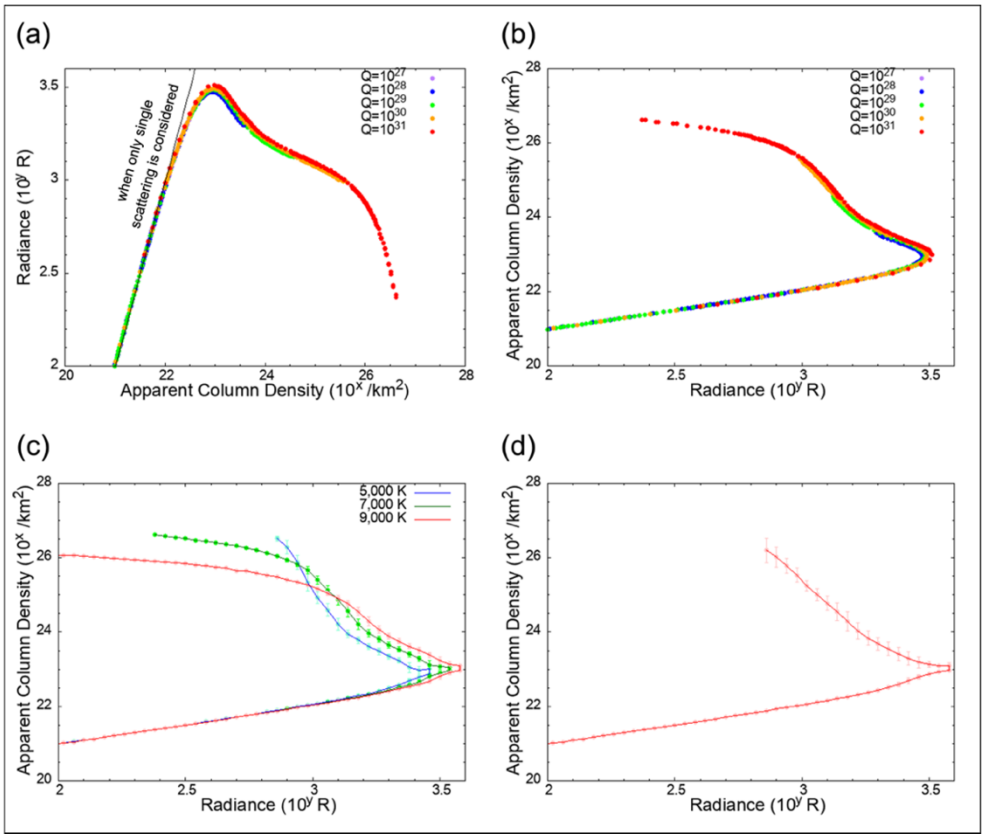

Fig. 6.6. Expected S/N ratio in deuterium Ly-α emission detection.

The accuracy of deuterium column density is 12%, the same as the relative error of brightness. Alternatively, when the water production rate exceeds approximately 10^{28} /s, Ly-α radiance of hydrogen observed during the comet fly-by phase is greatly affected by multiple scattering (Fig. 6.2). Therefore, the accuracy of converting Ly-α radiance to column density using the radiative transfer model determines the accuracy of estimation of hydrogen column density. Fig. 6.6a is the summary of the results of numerical computation of Ly-α radiance seen from HI organized as a function of column density along the line of sight. This corresponds to Fig. 4.6a in the Hisaki case. Not only the column density of hydrogen along the line of sight but that of all the hydrogen atoms on the optical path from the Sun to the observer via comet's coma affect the observed Ly-α

radiance. However, I will no longer focus on the water production rate hereafter since dependence of the correspondence between radiance and column density along the line of sight on the water production rate is small. While evaluating HI data, the Ly-α radiance is converted to hydrogen column density. In line with this process, the axes are changed to radiance on x-axis and column density on y-axis as depicted in Fig. 6.6b. Fig. 6.6c shows the results with diverse hydrogen temperatures from 5,000 K to 9,000 K. Error bars are due to variation of brightness for diverse water production rates of 10^{27}–10^{31} /s. The results at the hydrogen temperature of 7,000 ± 2,000 K, referring to Weaver et al. (2008) and Tenishev et al. (2008), are averaged as shown in Fig. 6.6d. From this figure, the relative error is approximately 40–60% in the region where multiple scattering is effective with a column density of more than 10^{22} /km^2. For example, the D/H ratio can be evaluated as $(1\pm0.5) \times 10^{-4}$ or $(4\pm2) \times 10^{-4}$. With these relative errors, it is possible to discriminate comets with D/H ratio as large as 67P/CG and those with D/H ratio as small as the Earth. Further hydrogen temperature constraints will enable to obtain more accurate D/H ratio. The following two ways of restricting hydrogen temperature are considered: (1) observationally constraining the temperature by the method described in Appendix 5.A1, (2) numerical computation using DSMC model after estimating water production rate from the Ly-α radiance distribution in the optically thin region by the method described in Chapter 3. For example, if the temperature is restricted to the 7,000 ± 1,000 K range, which is half of the range assumed in this subsection, the measurement accuracy of the D/H ratio can be reduced to 30–40%.

6.5. **Summary**

The Ly-α radiance which will be observed by HI was computed using radiative transfer model constructed in Chapter 4. It was combined with the effective area of HI obtained in Chapter 5 to create the simulated data. Using these results, the detectability of deuterium Ly-α emission was examined first. It was found that we can detect deuterium with a sufficient S/N ratio, except the case that water production rate and D/H ratio are as small as approximately 10^{27} /s and 1×10^{-4}.

Measurement of D/H ratio requires the determination of column densities of both deuterium and hydrogen. The deduced deuterium column density has a relative error of 12% due to the ambiguity of the absorption rate of the deuterium cell. Alternatively, that of hydrogen has a relative error of 60% at maximum due to the ambiguity of hydrogen temperature. Constraints of hydrogen temperature by observations during the approach phase or numerical computations utilizing DSMC model will allow us to obtain the D/H ratio with higher accuracy.

7. Conclusion

In this study, I determined the link between surface composition and SBEs by examining physical processes such as solar radiation acceleration and multiple scattering of SBEs, which possibly disturb the direct links between SBEs and surfaces.

In Chapter 2, I conducted a correlation analysis of the exosphere and surface distributions of Mg, Ca, and Na atoms on Mercury using the observational data obtained via MESSENGER. It was found in the previous study that Mg is concentrated in the lava plain, and its abundance in the exosphere above that region is increasing. In this study, distributions of Ca and Na, as well as that of Mg, were analyzed by applying physicochemical parameters. Mg atoms were strongly correlated between in their exospheric production rate and their surface abundance distributions, with a correlation coefficient of 0.70 ± 0.17, consistent result with the results of previous studies. By contrast, Ca atoms showed a weak correlation, with a correlation coefficient of 0.22 ± 0.14. This is thought to be a result of Ca having a grater solar radiation than Mg, implying that ejected atoms are soon swept away in an anti-solar direction, thereby weakening the correlation. Although there is no high longitude resolution surface distribution data, exospheric distribution showed only regions where surface temperature exceeded 550 K exhibited non-seasonal variation. This can be explained by the existence of two Na binding forms, weakly bound physisorption and strongly bound chemisorption, which have frequently been assumed in conventional models. From these results, the conditions for particle species that exhibit the exosphere-surface correlations on Mercury were thought to be, at a minimum, low solar radiation acceleration and moderate volatility. In this study, solar radiation acceleration and volatility were identified as the factors that disturb the link between the exosphere and

the surface. As both these factors are less effective on the celestial bodies further away from the Sun, the link will presumably be less disturbed on the satellites of outer planets, such as Europa and Ganymede. For exoplanets orbiting stars whose stellar types are different from the Sun, species exhibiting the exosphere–surface correlation may differ. Owing to data limitations, discussion on the exosphere-surface correlation on Mercury is currently restricted to Mg, Ca, and Na. Additional exospheric observational data from PHEBUS, MSASI, and SERENA, as well as surface observational data by MERTIS will allow more detailed discussion also on other elements such as C and S, which will lead to a more general understanding and the application of this knowledge to other celestial bodies.

In Chapter 3, I evaluated the fraction of the area active on the surface of comets using observational data from the Hisaki satellite. Water production rate is an important indicator of comet activities when inside a heliocentric distance of approximately 3 au, and most data have been provided by SOHO/SWAN observations. In this chapter, a sensitivity calibration of Hisaki using the Ly-α/Ly-β count ratio of observational data of the geocorona, which are usually used to subtract background noise, was conducted. Through the comparison of the Ly-α radiance distributions obtained from observations and those calculated by Kaneda's analytical model, water production rates of four long-period comets were evaluated. The obtained values were lower than those estimated using UV observations performed by the SOHO/SWAN and IR observations by IRTF/iSHELL by a factor of 2–20%. Constraints imposed by parameters such as velocities and photodissociation lifetimes of particles noted through observations and models must be considered. The fraction of active regions on the nucleus surfaces was estimated to be 5–26%. There are often several-fold differences in the water production

rates estimated using different instruments, primarily due to the difference in adopted parameters such as temperature, velocity, and lifetimes of particles. It is necessary to establish an observational-constraints method for these parameters, as these values are thought to be different for each comet. It is also important to construct an analytical model considering solar radiation acceleration with reference to Chamberlain model adopted in the analyses in Chapter 2.

In Chapter 4, I discussed the radiative transfer process in comae using numerical simulation to understand the cause of the Ly-α radiance distribution identified by Hisaki. From the analysis in Chapter 3, it was established that the slope of the Ly-α radiance profile becomes flatter below an altitude of approximately 5×10^4 km. This variation in inclination was attributed to multiple scattering, as the inflection point is unlikely to be generated by inter-atomic collisions. Constructed radiative transfer models were able to reproduce the Ly-α radiance profile obtained via Hisaki observations. According to calculations using this model, multiple scattering becomes effective in comae when the hydrogen column density exceeds approximately 5×10^{22} /km^2. Multiple scattering was found to cause the sunward/anti-sunward radiance asymmetry less than 3%, and the apparent increase of D/H ratio around the nuclei by a factor of more than 10. However, this is the case only for hydrogen and deuterium atoms, and the causal relationship between the D/H ratio in molecules and the active fraction pointed out by Lis et al. (2019) is still unknown. In the future, it will be necessary to investigate the fractionation effect of ice sublimation, as well as the differences in behavior of hydrogen and deuterium in comae. Comparisons of D/H ratios measured by optical observations of HI (integrated along the line of sight) and particle measurements of MANiaC (in situ measurement) will provide important data

for this discussion.

In Chapter 5, a design and performance evaluation of CI/HI were conducted to obtain new observational data of a comet. Firstly, it is determined to take two-dimensional images using HI to apply the analysis means developed in Chapters 2 and 3. Then, previous observations of Ly-α radiance in cometary comae were organized, and HI was found to require a field of view of 3.8°, a spatial resolution of 0.06°, and an effective area of 6×10^{-4} cm^2. Additionally, it was found that sensitivity around the wavelength of 130.4 nm should be reduced to 1/5 or less than that of 121.6 nm, although this constraint may be relaxed slightly. The optical system was optimized using optical design software, and the field of view, spatial distribution, and tolerance were investigated. From this, the design was confirmed to achieve a field of view of 3.8° and a spatial resolution of 0.02°. Tolerance of the positions of entrance and secondary mirrors was 100 μm. Finally, the performance of the band-pass filter, mirrors, and gas filters used for HI were experimentally evaluated, and effective area and wavelength resolution were calculated. This established that the transmittance of the band-pass filter at the wavelengths of 121.6 nm and 130.4 nm was 8.6 ± 0.5% and 2.4 ± 0.5%, respectively, and the reflectance of the mirrors was 67 ± 1% at 121.6 nm and 71 ± 1% at 130.4 nm. The effective area for the wavelength at 121.6 nm was 1×10^{-3} cm^2, and the effective area for the wavelength at 130.4 nm was about one-third of the effective area for that at 121.6 nm. These values overall satisfy the required performance.

Finally, in Chapter 6, the feasibility of measuring the D/H ratio of comets using a Hydrogen Imager was examined. The expected Ly-α radiance observed via HI was calculated using the radiative transfer model constructed in Chapter 4. Simulated

observational data were created using the effective area of the HI and the absorption rate of gas filters estimated in Chapter 5. Using these results, the feasibility of detecting deuterium and evaluating the D/H ratio via HI was discussed. It was found that deuterium could be detected with a sufficient S/N ratio unless the target comet was extremely faint and that the D/H ratio could be evaluated with relative error less than 50% using the model in Chapter 4. The largest error factor in D/H ratio calculation is the dependence of the results of radiative transfer model on hydrogen temperature. Constraint on observations by HI or calculation by models such as DSMC will enable the calculation of the D/H ratio with higher accuracy.

These studies established that the strength of the exosphere-surface correlation was determined by the volatility and the motion in the exosphere in the case of exospheres formed primarily by desorption from surface minerals, as in the case of Mercury. For comets, when activity increases, comae become optically thicker, and multiple scattering dominates the radiance distribution. Extraction of the number density distributions using a radiative transfer model is first necessary for the discussion of coma-surface correlation. To generally understand how well the exospheres reflect surface information, more observational data on additional elements in more celestial bodies are necessary. Moreover, the combination of geological insights and knowledge of the space environment and exospheric physics is necessary in order to interpret observational data and build new theories. Although geology and space physics often have different goals, collaboration that overcomes the differences in common sense and the purpose will be crucial.

Appendix

1.A1. Derivation of Chamberlain Model

In this appendix, Chamberlain model expressed by Equations (1.1)–(1.8) is deduced. It calculates the spread of the phase space density of exospheric particles based on Liouville's theorem. In the Haser model and Kaneda model, the photodissociation and photoionization lifetimes form the spatial distributions; in Chamberlain model, in contrast, loss processes are ignored and velocity distributions due to the temperature form the spatial distributions.

1.A1.1. Derivation of velocity functions at an arbitrary altitude

The velocity distribution at the exobase is defined by the following Maxwell distribution:

$$f(r_c, p_r, P_\chi) = \frac{n_c}{(2\pi m k_B T_c)^{3/2}}\, e^{-\frac{p_r^2}{2mk_BT_c}}\, e^{-\frac{P_\chi^2}{2mk_BT_c r_c^2}} \qquad (1.A1)$$

where r_c, p_r, P_χ are the distance of exobase from the celestial center, the radial component of the momentum, the angular momentum, respectively, n_c, T_c, are m the number density and temperature at the exobase, and the atomic mass, respectively. To derive the velocity distribution function at a distance of r $(> r_c)$, $\mathrm{d}\log f / \mathrm{d}r$ is calculated first.

$$\frac{d\,log\,f}{dr} = \frac{1}{f}\frac{df}{dr} \qquad (1.A2)$$

From Liouville's theorem, distribution function in phase space remains constant along dynamical trajectories as follows:

$$\frac{df}{dt} = 0$$

$$\therefore \frac{\partial f}{\partial t} + \sum_{i=1}^{3} \left(\frac{\partial f}{\partial q_i} \dot{q}_i + \frac{\partial f}{\partial p_i} \dot{p}_i \right) = 0 \tag{1.A3}$$

For spherical symmetry and a steady state, it is written as:

$$\frac{\partial f}{\partial r} \frac{dr}{dt} = -\frac{\partial f}{\partial p_r} \frac{dp_r}{dt} \tag{1.A4}$$

Using Equation $(1.A4)$, Equation $(1.A2)$ is calculated as:

$$\frac{d\, log\, f}{dr} = \frac{1}{f} \frac{df}{dr}$$

$$= -\frac{1}{f} \frac{\partial f}{\partial p_r} \frac{dp_r}{dt} \frac{1}{dr/dt} \tag{1.A5}$$

The partial differential of Equation $(1.A1)$ with respect to p_r is as follows:

$$\frac{\partial f}{\partial p_r} = -\frac{p_r}{m k_B T_c} f \tag{1.A6}$$

Using this, Equation $(1.A5)$ is calculated as:

$$\frac{d\, log\, f}{dr} = \frac{p_r}{m k_B T_c} \frac{dp_r}{dt} \frac{1}{dr/dt} \tag{1.A7}$$

The Hamiltonian in spherical coordinates is

$$\mathcal{H} = \frac{p_r^2}{2m} + \frac{P_x^2}{2mr^2} - \frac{GMm}{r} \tag{1.A8}$$

where M is the planetary mass. Equations of motion are following:

$$\dot{q}_i = \frac{\partial \mathcal{H}}{\partial p_i}$$

$$\therefore \frac{dr}{dt} = \frac{p_r}{m} \tag{1.A9}$$

$$\dot{p}_i = -\frac{\partial \mathcal{H}}{\partial q_i}$$

$$\therefore \begin{cases} \dfrac{dp_r}{dt} = \dfrac{P_x^2}{mr^3} - \dfrac{GMm}{r^2} \\ \dfrac{dP_\chi}{dt} = 0 \end{cases} \tag{1.A10}$$

Substituting Equations $(1.A9)$ and $(1.A10)$ into Equation $(1.A7)$ gives the following equation.

$$\frac{d\,log\,f}{dr} = \frac{p_r}{mk_BT_c}\left(\frac{P_x^2}{mr^3} - \frac{GMm}{r^2}\right)\frac{m}{p_r}$$

$$= -\frac{GMm}{k_BT_cr^2} + \frac{P_x^2}{mk_BT_cr^3} \qquad (1.A11)$$

Integration of this from $r = \mathrm{r_c}$ to r gives

$$\int_{r_c}^{r} dr\,\frac{\mathrm{d}\log f}{\mathrm{d}r} = \int_{r_c}^{r} dr\left(-\frac{GMm}{k_\mathrm{B}T_cr^2} + \frac{P_x^2}{mk_\mathrm{B}T_cr^3}\right)$$

$$\therefore \log f(r) - \log f(r_c) = \frac{GMm}{k_\mathrm{B}T_c}\left(\frac{1}{r} - \frac{1}{r_c}\right) - \frac{P_x^2}{mk_\mathrm{B}T_c}\left(\frac{1}{r^2} - \frac{1}{r_c^2}\right)$$

$$\therefore f(r) = f(r_c)e^{-\{\lambda(r_c)-\lambda(r)\}}\exp\left(-\frac{p_r^2}{2mk_\mathrm{B}T_c}\right)\exp\left(-\frac{P_x^2}{2mk_\mathrm{B}T_cr^2}\right)$$

$$\therefore f(r) = \frac{n_c}{(2\pi mk_BT_c)^{3/2}}e^{-\{\lambda(r_c)-\lambda(r)\}}\,exp\left(-\frac{p_r^2}{2mk_BT_c}\right)exp\left(-\frac{P_x^2}{2mk_BT_cr^2}\right) \qquad (1.A12)$$

where λ is an escape parameters at an altitude of r defined by

$$\lambda(r) = \frac{GMm}{k_BT_cr} \qquad (1.A13)$$

Hereafter, the value of each parameter at the exobase is indicated with the subscript c, such as $\lambda_c \equiv \lambda(r_c)$.

1.A1.2. Calculation of number densities

1.A1.2.1. Introduction of partition functions

Equation $(1.A12)$ is the velocity distribution function at an altitude of r. If momenta could take on all values, an integration over the whole momentum space would give the following number density

$$n_{all} = \int d^3p_r\,f(q_i, p_i)$$

$$= n_c e^{-(\lambda_c - \lambda)} \quad (1.A14)$$

In reality, the momenta are limited to what satisfy Equations $(1.A10)$. Therefore, the number density is calculated by

$$n(r) = 2\pi \int dp_r \int \frac{P_\chi}{r^2} dP_\chi f(q_i, p_i)$$

$$= \frac{2\pi n_c e^{-(\lambda_c - \lambda)}}{(2\pi m k_B T_c)^{3/2} r^2} \int dp_r \int dP_\chi \, P_\chi \, exp\left(-\frac{p_r^2}{2mk_B T_c}\right) exp\left(-\frac{P_x^2}{2mk_B T_c r^2}\right) \quad (1.A15)$$

It can be rewritten as

$$n(r) = n_{all} \zeta(r) \quad (1.A16)$$

where ζ is a partition function defined by

$$\zeta(r) = \frac{2\pi}{(2\pi m k_B T_c)^{3/2} r^2} \int dp_r \int dP_\chi \, P_\chi \, exp\left(-\frac{p_r^2}{2mk_B T_c}\right) exp\left(-\frac{P_x^2}{2mk_B T_c r^2}\right) (1.A17)$$

When

$$\nu(r) = \frac{P_x^2}{2mk_B T_c r^2} \quad (1.A18)$$

$$\xi(r) = \frac{p_r}{(2mk_B T_c)^{1/2}} \quad (1.A19)$$

are introduced, the total kinetic energy ψ and total energy h in units of $k_B T_c$ are expressed by following equations:

$$\psi(r) = \frac{mv^2}{2k_B T_c} = \xi^2(r) + \nu(r) \quad (1.A20)$$

$$h = \frac{\mathcal{H}}{k_B T_c} = \xi^2(r) + \nu(r) - \lambda(r) = \psi(r) - \lambda(r) \quad (1.A21)$$

As

$$\frac{d\nu}{dP_\chi} = \frac{P_\chi}{mk_B T_c r^2} \quad (1.A22)$$

$$\frac{d\xi}{dp_r} = \frac{1}{(2mk_B T_c)^{1/2}} \quad (1.A23)$$

are derived from Equations $(1.A18)(1.A19)$ and $(1.A19)$, the partition function of Equation $(1.A17)$ is expressed using ν and ξ as follows:

$$\zeta(\lambda) = \frac{1}{\sqrt{\pi}} \int d\nu \int d\xi \, e^{-\xi^2 - \nu} \tag{1.A24}$$

As the ranges of possible values for (ξ, ν) differ depending on the shape of orbits, the values of the partition function are calculated separately for three orbit conditions: ballistic, satellite, and escape orbits.

1.A1.2.2. Case 1: ballistic orbit

Particles in ballistic orbits satisfy the following three conditions: (1) the radial component of momenta at the exobase normalized by thermal energy ξ_c is a real number, as particles are ejected from the surface, (2) the normalized radial component of momenta ξ is symmetrical in positive and negative values due to the symmetry of orbits, and (3) the normalized total energy h is negative due to the gravitational bind to the system. As Equation $(1.A10)$ means that P_χ is constant, $\nu(r)r^2$ is also constant according to Equation $(1.A18)$. Therefore,

$$\nu(r) = \frac{r_c^2}{r^2}\nu_c$$

$$\therefore h + \lambda - \xi^2 = \frac{\lambda^2}{\lambda_c^2}(h + \lambda - \xi_c^2)$$

$$\therefore h = \frac{\lambda^2}{\lambda_c^2 - \lambda^2}\left\{\lambda_c - \xi_c^2 - \frac{\lambda_c^2}{\lambda^2}(\lambda - \xi^2)\right\}$$

$$\therefore \nu = \frac{\lambda^2}{\lambda_c^2 - \lambda^2}\left\{\lambda_c - \xi_c^2 - \frac{\lambda_c^2}{\lambda^2}(\lambda - \xi^2)\right\} - \xi^2 + \lambda$$

$$= \frac{\lambda^2}{\lambda_c^2 - \lambda^2}(\lambda_c - \lambda - \xi_c^2 + \xi^2)$$

$$\leq \frac{\lambda^2}{\lambda_c^2 - \lambda^2}(\lambda_c - \lambda + \xi^2) \equiv \nu_1 \tag{1.A25}$$

As the total energy h is negative,

$$\xi^2 + \nu - \lambda < 0$$

$$\therefore \nu < \lambda - \xi^2 \equiv \nu_2 \tag{1.A26}$$

According to Equation $(1.A18)$, ν is positive. Therefore, Equation $(1.A26)$ implies that

$$\xi^2 < \lambda \tag{1.A27}$$

Here, the following formula holds:

$$\nu_1 \gtrless \nu_2 \Leftrightarrow \frac{\lambda^2}{\lambda_c^2 - \lambda^2}(\lambda_c - \lambda + \xi^2) \gtrless \lambda - \xi^2$$

$$\Leftrightarrow \lambda_c^2 \xi^2 \gtrless \lambda_c \lambda(\lambda_c - \lambda)$$

$$\Leftrightarrow \xi^2 \gtrless \lambda\left(1 - \frac{\lambda}{\lambda_c}\right) \equiv \xi_1^2 \tag{1.A28}$$

When Equation $(1.A24)$ is calculated considering possible combinations of (ξ, ν) based on Equations $(1.A25)$–$(1.A28)$, the following equation is acquired:

$$\begin{aligned}\zeta_{bal}(\lambda) &= \frac{1}{\sqrt{\pi}}\left(\int_{-\sqrt{\lambda}}^{-\xi_1} d\xi \int_0^{\nu_2} d\nu\, e^{-\xi^2-\nu} + \int_{-\xi_1}^{\xi_1} d\xi \int_0^{\nu_1} d\nu\, e^{-\xi^2-\nu}\right. \\ &\quad \left. + \int_{\xi_1}^{\sqrt{\lambda}} d\xi \int_0^{\nu_2} d\nu\, e^{-\xi^2-\nu}\right) \\ &= \frac{2}{\sqrt{\pi}}\left(\int_0^{\xi_1} d\xi \int_0^{\nu_1} d\nu\, e^{-\xi^2-\nu} + \int_{\xi_1}^{\sqrt{\lambda}} d\xi \int_0^{\nu_2} d\nu\, e^{-\xi^2-\nu}\right) \\ &= \frac{2}{\sqrt{\pi}}\left(\int_0^{\xi_1} d\xi \int_{\xi_1^2}^{\nu_1+\xi_1^2} d\psi\, e^{-\psi} + \int_{\xi_1}^{\sqrt{\lambda}} d\xi \int_{\xi_1^2}^{\nu_2+\xi_1^2} d\psi\, e^{-\psi}\right)\end{aligned} \tag{1.A29}$$

From Equations $(1.A25)$ and $(1.A26)$, the following equations are obtained for the interval of integration:

$$\nu_1 + \xi_1^2 = \frac{\lambda^2}{\lambda_c + \lambda} + \frac{\lambda_c^2}{\lambda_c^2 - \lambda^2}\xi^2 \equiv \psi_1 + \frac{\lambda_c^2}{\lambda_c^2 - \lambda^2}\xi^2 \tag{1.A30}$$

$$\nu_2 + \xi_1^2 = \lambda \tag{1.A31}$$

The integration interval of Equation $(1.A29)$ is shown in Fig. 1.A1. As can be seen

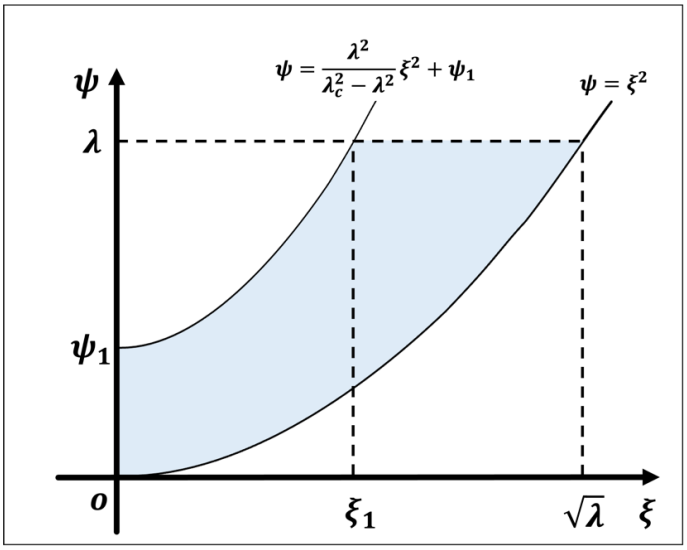

Fig. 1.A1. Integration interval in the case of ballistic orbits.

from the figure, the interval of integration can be converted as follows:

$$\zeta_{bal}(\lambda) = \frac{2}{\sqrt{\pi}}\left(\int_0^{\lambda} d\psi \int_0^{\sqrt{\xi}} d\xi\, e^{-\psi} - \int_{\psi_1}^{\lambda} d\psi \int_0^{\sqrt{\left(1-\frac{\lambda^2}{\lambda_c^2}\right)(\psi-\psi_1)}} d\xi\, e^{-\psi}\right)$$

$$= \frac{2}{\sqrt{\pi}}\left(\int_0^{\lambda} d\psi\, \psi^{\frac{1}{2}} e^{-\psi} - \int_{\psi_1}^{\lambda} d\psi\, e^{-\psi}\sqrt{\left(1-\frac{\lambda^2}{\lambda_c^2}\right)(\psi-\psi_1)}\right)$$

$$= \frac{2}{\sqrt{\pi}}\left(\int_0^{\lambda} d\psi\, \psi^{\frac{1}{2}} e^{-\psi} - \int_{\psi_1}^{\lambda} d\psi'\, e^{-\psi_1} e^{-\psi'}\sqrt{\left(1-\frac{\lambda^2}{\lambda_c^2}\right)}\psi'^{\frac{1}{2}}\right)$$

$$= \frac{2}{\sqrt{\pi}}\left\{\gamma\left(\frac{3}{2},\lambda\right) - \frac{\sqrt{\lambda_c^2-\lambda^2}}{\lambda_c} e^{-\psi_1}\gamma\left(\frac{3}{2},\lambda-\psi_1\right)\right\} \qquad (1.A32)$$

where ψ' is defined by $\psi' \equiv \psi - \psi_1$ and γ is an incomplete gamma function.

1.A1.2.3. Case 2: satellite orbit

Particles in satellite orbits are those which satisfy $h < 0$ other than in ballistic orbits. The sum of the partition functions of ballistic and satellite particles is calculated

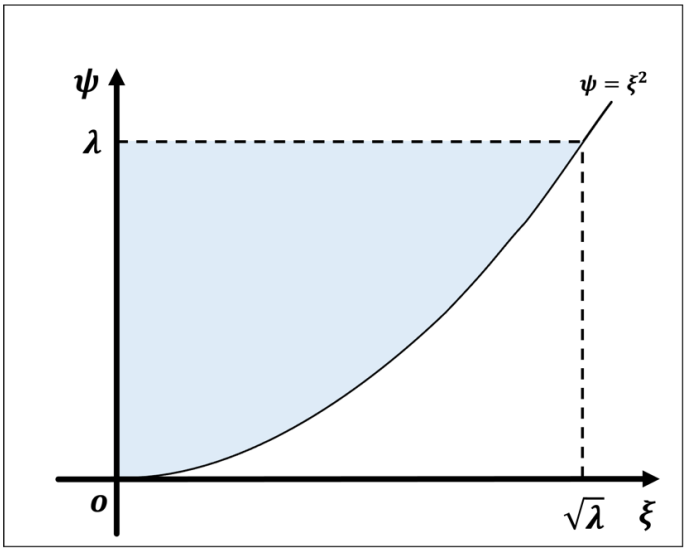

Fig. 1.A2. Integration interval in the case of satellite orbits.

as follows based on Equation $(1.A24)$:

$$\begin{aligned}\zeta_{bal}(\lambda)+\zeta_{sat}(\lambda) &= \frac{1}{\sqrt{\pi}}\int_{-\xi_1}^{\xi_1} d\xi \int_0^{\nu_2} d\nu\, e^{-\xi^2-\nu} \\ &= \frac{2}{\sqrt{\pi}}\int_0^{\sqrt{\lambda}} d\xi \int_{\xi^2}^{\lambda} d\psi\, e^{-\psi} \end{aligned} \tag{1.A33}$$

The integration interval of Equation $(1.A33)$ is shown in Fig. 1.A2. It can be converted as follows:

$$\begin{aligned}\zeta_{bal}(\lambda)+\zeta_{sat}(\lambda) &= \frac{2}{\sqrt{\pi}}\int_0^{\lambda} d\psi \int_0^{\sqrt{\psi}} d\xi\, e^{-\psi} \\ &= \frac{2}{\sqrt{\pi}}\int_0^{\lambda} d\psi\, \psi^{\frac{1}{2}} e^{-\psi} \\ &= \frac{2}{\sqrt{\pi}}\gamma\left(\frac{3}{2},\lambda\right) \end{aligned} \tag{1.A34}$$

Thus, the partition function for satellite orbits are calculated by

$$\zeta_{sat}(\lambda) = \frac{2}{\sqrt{\pi}}\frac{\sqrt{\lambda_c^2-\lambda^2}}{\lambda_c} e^{-\psi_1}\gamma\left(\frac{3}{2},\lambda-\psi_1\right) \tag{1.A35}$$

which is derived from Equations $(1.A32)$ and $(1.A34)$.

1.A1.2.4. Case 3: escape orbit

Particles in escape orbits satisfy $h > 0$ and $\xi_c > 0$ (upward gas ejection). These conditions require that

$$\nu \in \boldsymbol{R} \Rightarrow \nu > 0 \tag{1.A36}$$

$$h > 0 \Rightarrow \nu > \nu_2 \tag{1.A37}$$

Besides, Equation $(1.A18)$ means $\nu > 0$. As

$$\begin{aligned} \nu_2 &\gtrless 0 \\ \Leftrightarrow \lambda - \xi^2 &\gtrless 0 \\ \Leftrightarrow \xi &\lessgtr \sqrt{\lambda} \end{aligned} \tag{1.A38}$$

Hence,

$$\begin{aligned} \zeta_{esc}(\lambda) &= \frac{1}{\sqrt{\pi}} \int_{\xi_1}^{\sqrt{\lambda}} d\xi \int_{\nu_2}^{\nu_1} d\nu \, e^{-\xi^2-\nu} + \frac{1}{\sqrt{\pi}} \int_{\sqrt{\lambda}}^{\infty} d\xi \int_{0}^{\nu_1} d\nu \, e^{-\xi^2-\nu} \\ &= \frac{1}{\sqrt{\pi}} \int_{\xi_1}^{\sqrt{\lambda}} d\xi \int_{\nu_2+\xi^2}^{\nu_1+\xi^2} d\psi \, e^{-\psi} + \frac{1}{\sqrt{\pi}} \int_{\sqrt{\lambda}}^{\infty} d\xi \int_{\xi^2}^{\nu_1+\xi^2} d\psi \, e^{-\psi} \end{aligned} \tag{1.A39}$$

The integration interval of Equation $(1.A39)$ $(1.A33)$is shown in Fig. 1.A3. It can be converted as follows:

$$\zeta_{esc}(\lambda) = \frac{1}{\sqrt{\pi}} \int_{\lambda}^{\infty} d\psi \int_{\sqrt{\left(1-\frac{\lambda^2}{\lambda_c^2}\right)(\psi-\psi_1)}}^{\sqrt{\lambda}} d\xi \, e^{-\psi}$$

$$= \frac{1}{\sqrt{\pi}} \int_{\lambda}^{\infty} d\psi \, \psi^{\frac{1}{2}} e^{-\psi} \left\{ 1 - \sqrt{\left(1-\frac{\lambda^2}{\lambda_c^2}\right)\left(1-\frac{\psi_1}{\psi}\right)} \right\}$$

$$= \frac{1}{\sqrt{\pi}} \int_{0}^{\infty} d\psi \, \psi^{\frac{1}{2}} e^{-\psi} - \frac{1}{\sqrt{\pi}} \int_{0}^{\lambda} d\psi \, \psi^{\frac{1}{2}} e^{-\psi}$$

$$- \frac{1}{\sqrt{\pi}} \sqrt{\left(1-\frac{\lambda^2}{\lambda_c^2}\right)} \int_{\lambda}^{\infty} d\psi \, e^{-\psi} \sqrt{\psi-\psi_1}$$

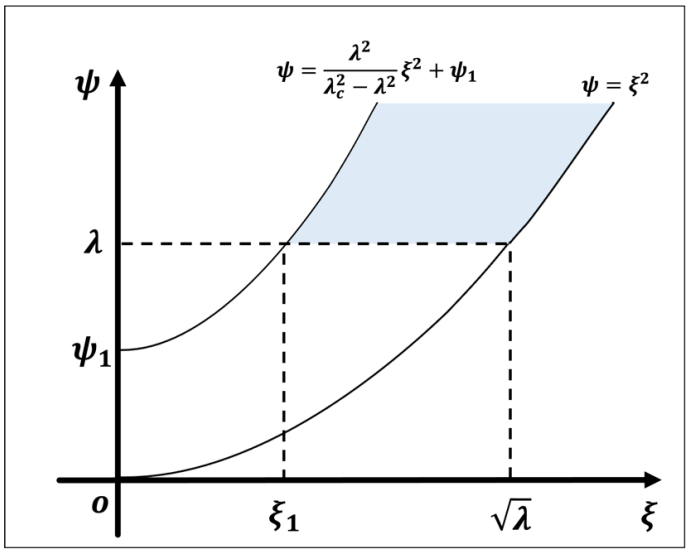

Fig. 1.A3. Integration interval in the case of escape orbits.

$$= \frac{1}{\sqrt{\pi}}\left\{\Gamma\left(\frac{3}{2}\right) - \gamma\left(\frac{3}{2},\lambda\right)\right.$$

$$\left. - \sqrt{\left(1 - \frac{\lambda^2}{\lambda_c^2}\right)}e^{-\psi_1}\left(\int_0^{\infty} d\psi'\,\psi'^{\frac{1}{2}}e^{-\psi'} - \int_0^{\lambda} d\psi'\,\psi'^{\frac{1}{2}}e^{-\psi'}\right)\right\}$$

$$= \frac{1}{\sqrt{\pi}}\left[\Gamma\left(\frac{3}{2}\right) - \gamma\left(\frac{3}{2},\lambda\right) - \sqrt{\left(1 - \frac{\lambda^2}{\lambda_c^2}\right)}e^{-\psi_1}\left\{\Gamma\left(\frac{3}{2}\right) - \gamma\left(\frac{3}{2},\lambda\right)\right\}\right] \qquad (1.A40)$$

1.A1.2.5. Calculation of number densities

In Subsections 1.A1.2.2 to 1.A1.2.5, the partition functions were calculated for three types of orbits. The number density can be written using Equations $(1.A14)$, $(1.A16)$, $(1.A32)$, $(1.A35)$, and $(1.A40)$. However, in the case of Mercury, satellites orbits are often ignored and only particles in ballistic and escape orbits are considered (e.g. Merkel et al., 2017). Besides, when satellite particles are negligible and particles in escape orbits are not dominant, the total number density is written by simple analytic

expression as follows:

$$\begin{aligned}\zeta_{tot} &= \zeta_{bal} + \zeta_{esc} \\ &\approx \zeta_{bal} + 2\zeta_{esc} \\ &= \frac{2}{\sqrt{\pi}}\left(1 - \sqrt{1 - \frac{\lambda^2}{\lambda_c^2}}e^{-\psi_1}\right)\Gamma\left(\frac{3}{2}\right) \\ &= 1 - \sqrt{1 - \frac{\lambda^2}{\lambda_c^2}}e^{-\psi_1}\end{aligned}$$

$$\therefore\ n(r) = n_c e^{-(\lambda_c - \lambda)}\left(1 - \sqrt{1 - \frac{\lambda^2}{\lambda_c^2}}e^{-\psi_1}\right) \qquad (1.A41)$$

1.A2. Derivation of Eddington's Fountain Model

In this appendix, Eddington's Fountain model expressed by Equation (1.15) is deduced. The outline of the coma is calculated considering only the free expansion and uniform acceleration.

A cylindrical coordinate system (r_{xy}, ϕ, z) is set. The z-axis is in the anti-sunward direction (Fig. 1.A4). The equation of the envelope formed by the particles ejected from the coordinate origin (center of the nucleus) in various directions with a uniform velocity v and accelerated in the positive direction of the z-axis with a constant acceleration a is calculated. When assuming that initial velocities are $\dot{r}_{xy} = v\cos\theta$ and $\dot{z} = v\sin\theta$ and initial position is $r_{xy} = z = 0$, respectively, the equation of motion for particles ejected at an angle of θ is as follows:

$$\begin{cases} \ddot{r}_{xy} = 0 \\ \ddot{z} = a \end{cases}$$

$$\therefore \begin{cases} \dot{r}_{xy} = v\cos\theta \\ \dot{z} = v\sin\theta + at \end{cases}$$

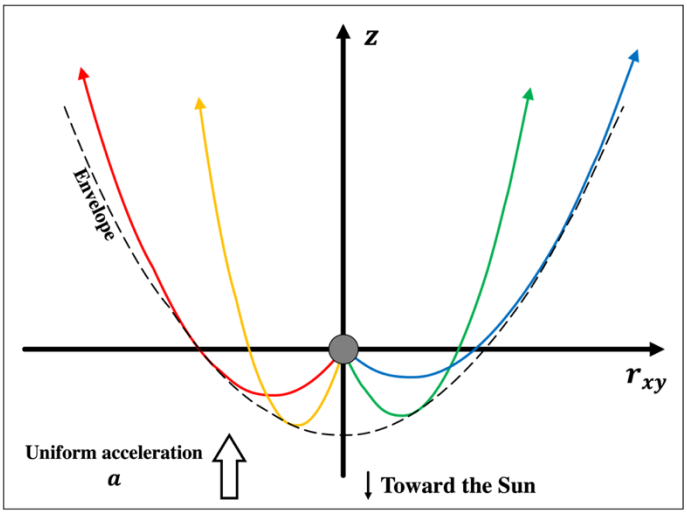

Fig. 1.A4. Orbits of particles in comae and their envelope.

$$\therefore \begin{cases} r_{xy} = vt\cos\theta \\ z = vt\sin\theta + \frac{1}{2}at^2 \end{cases} \quad (1.A42)$$

When θ is eliminated using $\sin^2\theta + \cos^2\theta = 1$, the equation is rewritten as follows:

$$r_{xy}^2 + \left(z - \frac{1}{2}at^2\right)^2 = v^2t^2$$

$$\therefore \frac{1}{4}a^2t^4 - (az + v^2)t^2 + r_{xy}^2 + z^2 = 0 \quad (1.A43)$$

Regarding this equation as a quadratic equation in t^2, the conditions under which this has solutions are expressed by the following discriminant:

$$(az + v^2)^2 - 4 \cdot \frac{1}{4}a^2t^4 \cdot \left(r_{xy}^2 + z^2\right) > 0$$

$$\therefore r_{xy}^2 < 2z\frac{v^2}{a} + \frac{v^4}{a^2} \quad (1.A44)$$

Therefore, the envelope of particles is expressed by the following paraboloid:

$$x^2 + y^2 = 2z\frac{v^2}{a} + \frac{v^4}{a^2} \quad (1.A45)$$

1.A3. Derivation of Haser Model

In this appendix, the Haser model expressed by Equation (1.16) is deduced. In this model, the steady-state number density distributions of daughter molecules are calculated for two-generation systems. In the latter part of this appendix, it is extended to the case of three-generation systems.

Let $F_p(r)$ be the number flux of parent molecules at a distance of r. The total number of parent molecules which cross a sphere of radius r per unit time is written by the following equation:

$$4\pi r^2 F_p(r) = 4\pi r_N^2 F_p(r_N) e^{-\frac{r-r_N}{\gamma_p}} \tag{1.A46}$$

where r_N is a radius of the nucleus, and γ_p is the product of velocity and lifetime of parent molecules. $F_p(r_N)$ is expressed as follows using the production rate of the parent molecules Q_p:

$$F_p(r_N) = \frac{Q_p}{4\pi r_N^2}$$

The production rate of daughter molecules is written as follows:

$$\begin{aligned} Q_d(r) &= -\frac{d}{dr}\{4\pi r^2 F_p(r)\} \\ &= 4\pi r_N^2 F_p(r_N) \frac{1}{\gamma_p} e^{-\frac{r-r_N}{\gamma_p}} \end{aligned} \tag{1.A47}$$

The flux of daughter molecules produced at an altitude of x which cross a sphere of radius r is written by the following equation:

$$\begin{aligned} f_d(x,r) &= \frac{Q_d(x)}{4\pi r^2} e^{-\frac{r-x}{\gamma_d}} \\ &= F_p(r_N) \frac{r_N^2}{r^2} \frac{1}{\gamma_p} e^{-\frac{x-r_N}{\gamma_p}} e^{-\frac{r-x}{\gamma_d}} \end{aligned} \tag{1.A48}$$

where γ_d is the product of velocity and lifetime of daughter molecules. When $f_d(x,r)$

is integrated over the generation point x, the total flux of daughter molecules at an altitude r is calculated as follows:

$$\begin{aligned} F_d(r) &= \int_{r_N}^{r} dx\, f_d(x,r) \\ &= F_p(r_N)\frac{r_N^2}{r^2}\frac{1}{\gamma_p}\int_{r_N}^{r} dx\, e^{-\frac{x-r_N}{\gamma_p}} e^{-\frac{r-x}{\gamma_d}} \\ &= F_p(r_N)\frac{r_N^2}{r^2}\frac{1}{\gamma_p} e^{\frac{r_N}{\gamma_p}-\frac{r}{\gamma_d}}\int_{r_N}^{r} dx\, e^{\frac{x}{\gamma_d}-\frac{x}{\gamma_p}} \\ &= F_p(r_N)\frac{r_N^2}{r^2}\frac{1}{\gamma_p} e^{\frac{r_N}{\gamma_p}-\frac{r}{\gamma_d}}\frac{\gamma_p\gamma_d}{\gamma_p-\gamma_d}\left(e^{\frac{r}{\gamma_d}-\frac{r}{\gamma_p}} - e^{\frac{r_N}{\gamma_d}-\frac{r_N}{\gamma_p}}\right) \\ &= F_p(r_N)\frac{r_N^2}{r^2}\frac{\gamma_d}{\gamma_p-\gamma_d}\left(e^{-\frac{r-r_N}{\gamma_p}} - e^{-\frac{r-r_N}{\gamma_d}}\right) \end{aligned} \quad (1.A49)$$

When r is sufficiently larger than r_N, the number density of daughter molecules at an altitude of r can be calculated by the following equation:

$$\begin{aligned} n_d(r) &= \frac{F_d(r)}{v_d} \\ &= \frac{F_p(r_N)}{v_d}\frac{r_N^2}{r^2}\frac{\gamma_d}{\gamma_p-\gamma_d}\left(e^{-\frac{r}{\gamma_p}} - e^{-\frac{r}{\gamma_d}}\right) \\ &= \frac{Q_p}{4\pi r^2 v_d}\frac{\gamma_d}{\gamma_p-\gamma_d}\left(e^{-\frac{r}{\gamma_p}} - e^{-\frac{r}{\gamma_d}}\right) \end{aligned} \quad (1.A50)$$

where v_d is the velocity of daughter molecules. This is equivalent to Equation (1.16).

A three-stage model (O'Dell et al., 1988) can be derived in the continuation. First, Equation (1.A49) is rewritten using β_p and β_d, which are defined by $\beta_p \equiv 1/\gamma_p$ and $\beta_d \equiv 1/\gamma_d$, respectively, as follows:

$$F_d(r) = \frac{Q_p}{4\pi r^2}\frac{\beta_p}{\beta_d-\beta_p}\left(e^{-\beta_p(r-r_N)} - e^{-\beta_d(r-r_N)}\right) \quad (1.A51)$$

The production rate of granddaughter atoms generated by the daughter molecules is written as follows:

$$Q_g(r) = -\frac{d}{dr}\{4\pi r^2 F_p(r)\} - \frac{d}{dr}\{4\pi r^2 F_d(r)\}$$

$$= \frac{Q_p}{4\pi r^2}\beta_p e^{-\beta_p(r-r_N)} + \frac{Q_p}{4\pi r^2}\frac{\beta_p}{\beta_d-\beta_p}\left(\beta_p e^{-\beta_p(r-r_N)} - \beta_d e^{-\beta_d(r-r_N)}\right)$$

$$= \frac{Q_p}{4\pi r^2}\frac{\beta_p\beta_d}{\beta_d-\beta_p}\left(e^{-\beta_p(r-r_N)} - e^{-\beta_d(r-r_N)}\right) \qquad (1.A52)$$

Unlike the case of $Q_d(r)$, the production rate of daughter molecules is fluctuated by both supply due to the dissociation of the parent molecules and loss due to the dissociation of the daughter molecules. The flux of granddaughter atoms produced at an altitude of x which cross a sphere of radius r is expressed by the following equation:

$$f_g(x,r) = Q_g(x)\, e^{-\beta_g(r-x)}$$

$$= \frac{Q_p}{4\pi r^2}\frac{\beta_p\beta_d}{\beta_d-\beta_p}\left(e^{-\beta_p(x-r_N)} - e^{-\beta_d(x-r_N)}\right) e^{-\beta_g(r-x)} \qquad (1.A53)$$

where β_g is the reciprocal number of the product of velocity and lifetime of granddaughter atoms. When $f_g(x,r)$ is integrated over the generation point x, the total flux of granddaughter atoms at an altitude of r is as follows:

$$F_g(r) = \int_{r_N}^{r} dx\, f_g(x,r)$$

$$= \frac{Q_p}{4\pi r^2}\frac{\beta_p\beta_d}{\beta_d-\beta_p}\int_{r_N}^{r} dx\, \left(e^{-\beta_p(x-r_N)} - e^{-\beta_d(x-r_N)}\right) e^{-\beta_g(r-x)}$$

$$= \frac{Q_p}{4\pi r^2}\frac{\beta_p\beta_d}{\beta_d-\beta_p}\left[\begin{array}{l}\dfrac{1}{\beta_g-\beta_p}\left\{e^{-\beta_p(r-r_N)} - e^{-\beta_g(r-r_N)}\right\} \\ \quad -\dfrac{1}{\beta_g-\beta_d}\left\{e^{-\beta_d(r-r_N)} - e^{\beta_g(r-r_N)}\right\}\end{array}\right]$$

$$= \frac{Q_p}{4\pi r^2}\left\{\begin{array}{c} -\dfrac{\beta_p\beta_d}{(\beta_p-\beta_d)(\beta_g-\beta_p)} e^{-\beta_p(r-r_N)} \\ -\dfrac{\beta_p\beta_d}{(\beta_d-\beta_g)(\beta_p-\beta_d)} e^{-\beta_d(r-r_N)} \\ -\dfrac{\beta_p\beta_d}{(\beta_g-\beta_p)(\beta_d-\beta_g)} e^{-\beta_g(r-r_N)}\end{array}\right\} \qquad (1.A54)$$

Assuming $r \gg r_N$, the number density of granddaughter atoms is as follows:

$$n_g(r) = \frac{Q_p}{4\pi r^2 v_g} \left\{ \begin{array}{c} -\frac{\beta_p \beta_d}{(\beta_p - \beta_d)(\beta_g - \beta_p)} e^{-\beta_p r} \\ -\frac{\beta_p \beta_d}{(\beta_d - \beta_g)(\beta_p - \beta_d)} e^{-\beta_d r} \\ -\frac{\beta_p \beta_d}{(\beta_g - \beta_p)(\beta_d - \beta_g)} e^{-\beta_g r} \end{array} \right\} \quad (1.A55)$$

When the hydrogen number density is deduced from the water production rate, the number densities of hydrogen generated by $H_2O \rightarrow OH + H$ (H is a daughter) and $OH \rightarrow O + H$ (H is a granddaughter) are calculated by Equations $(1.A50)$ and $(1.A55)$, respectively.

The calculated densities are demonstrated in Fig. 1.A5. $\tau_p, \tau_d,$ and τ_g are 27 hours, 23 hours, 159 days, respectively, and v_p, v_d, v_{g_1} and v_{g_2} are 0.85, 0.85, 20, and 8 km/s, respectively.

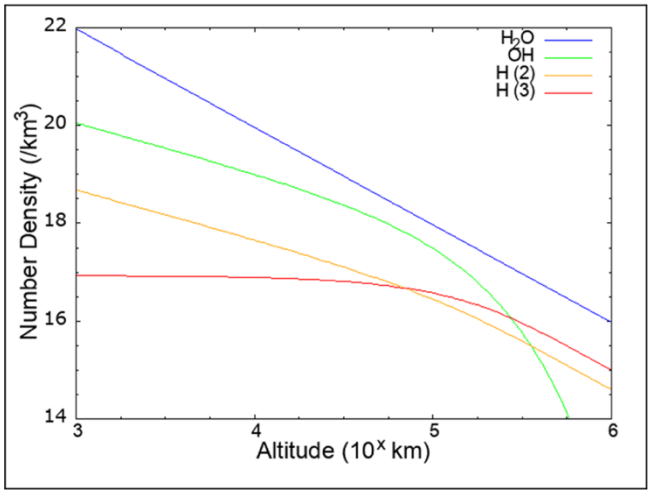

Fig. 1.A5. Number densities calculated from Haser model.

The blue and green lines represent the number densities of H_2O and OH molecules, respectively. The orange and red lines represent those of H atoms generated from H_2O and OH molecules, respectively.

1.A4. Derivation of Kaneda Model

In this appendix, the Kaneda model expressed by Equation (1.17) is deduced. Variables related to H_2O, OH, and H particles are subscripted with $p, d,$ and g (e.g., $Q_{\mathrm{p}}, v_d,$ and τ_g), respectively. When H atoms generated from H_2O and OH molecules are necessary to be distinguished, subscripts are g_1 and g_2, respectively. In this model, H_2O and OH molecules are assumed to be fixed at the origin of the coordinate, or the center of the nucleus, since they are much slower than H atoms. This means that H atoms are supplied from a point source.

First, the total number of H_2O and OH molecules is expressed as follows:

$$N_p(t) = N_d(t) = 0 \quad (t < 0) \tag{1.A56}$$

$$\frac{dN_p(t)}{dt} = Q_p - \frac{N_p(t)}{\tau_p} \quad (t > 0) \tag{1.A57}$$

$$\frac{dN_d(t)}{dt} = \frac{N_p(t)}{\tau_p} - \frac{N_d(t)}{\tau_d} \quad (t > 0) \tag{1.A58}$$

where N, Q_p, τ and t are the total number of particles, water production rate from the nucleus, lifetimes against photodissociation, and the elapsed time since the beginning of water ejection, respectively. Solving Equations $(1.A57)$ and $(1.A58)$ gives:

$$N_p(t) = Q_p \left(1 - e^{-\frac{t}{\tau_p}}\right) \tau_p \tag{1.A59}$$

$$N_d(t) = \frac{Q_p \tau_d}{\tau_p - \tau_d} \left\{ \left(\tau_p - \tau_d\right) - \tau_p e^{-\frac{t}{\tau_p}} + \tau_d e^{-\frac{t}{\tau_d}} \right\} \tag{1.A60}$$

The number of hydrogen atoms generated by photodissociation of H_2O and OH is calculated by the following equation.

$$Q_{g_1}(t) = \frac{N_p(t)}{\tau_p}$$

$$= \begin{cases} 0 & (t < 0) \\ Q_p \left(1 - e^{-\frac{t}{\tau_p}}\right) & (t > 0) \end{cases} \quad (1.A61)$$

$$Q_{g_2}(t) = \frac{N_p(t)}{\tau_p}$$

$$= \begin{cases} 0 & (t < 0) \\ \frac{Q_p}{\tau_p - \tau_d} \left\{ (\tau_p - \tau_d) - \tau_p e^{-\frac{t}{\tau_p}} + \tau_d e^{-\frac{t}{\tau_d}} \right\} & (t > 0) \end{cases} \quad (1.A62)$$

Kanada model also deduces the number of hydrogen atoms supplied after the water ejection stops, although it is omitted in this appendix.

Considering time to reach an altitude r and the fraction of atoms lost due to photoionization during the flight, the hydrogen number density at an altitude r is calculated by the following equation.

$$n_g(t, r) = \frac{Q_{g_1}\left(t - \frac{r}{v_{g_1}}\right)}{4\pi r^2 v_{g_1}} e^{-\frac{r}{\tau_g v_{g_1}}} + \frac{Q_{g_2}\left(t - \frac{r}{v_{g_2}}\right)}{4\pi r^2 v_{g_2}} e^{-\frac{r}{\tau_g v_{g_2}}} \quad (1.A63)$$

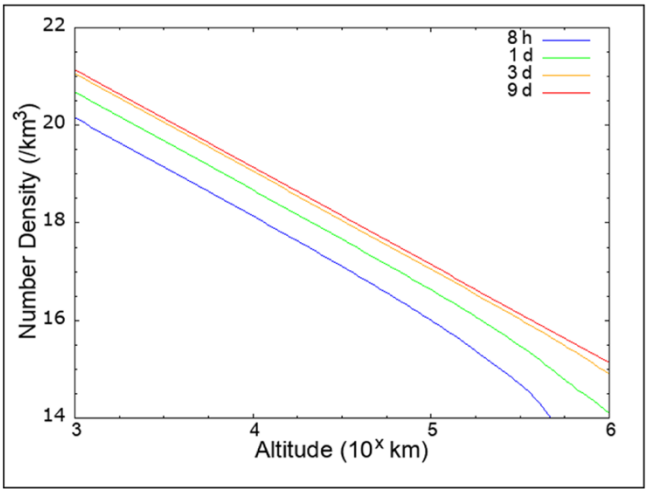

Fig. 1.A6. Number densities calculated from Kaneda model.

The blue, green, orange, and red lines represent the results with t = 8 h, 1 d, 3 d, and 9 d, respectively.

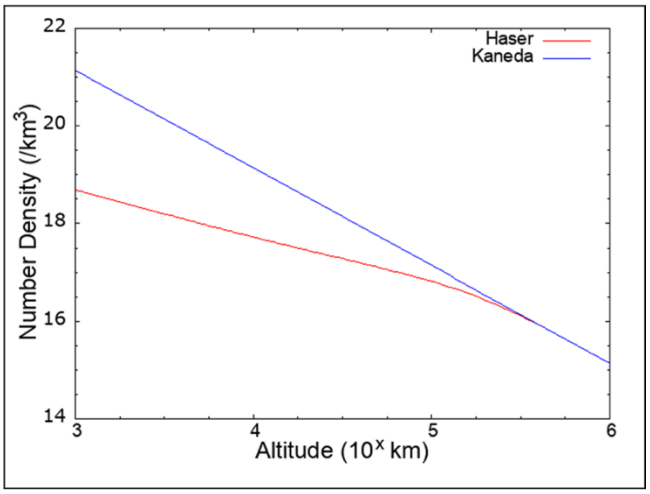

Fig. 1.A7. Comparison of number densities calculated from Haser and Kaneda models. The red and blue lines represent the results of Haser and Kaneda models, respectively.

$Q_{g_1}\left(t-\frac{r}{v_{g_1}}\right)$ and $Q_{g_2}\left(t-\frac{r}{v_{g_2}}\right)$ are calculated by Equations $(1.A61)$ and $(1.A62)$. The calculated densities are demonstrated in Fig. 1.A6. $\tau_p, \tau_d,$ and τ_g are 27 hours, 23 hours, 159 days, respectively, and v_{g_1} and v_{g_2} are 20 and 8 km/s, respectively.

The comparison between the results of Haser model and Kaneda model with $t = 9$ d is shown in Fig. 1.A7. Additionally, comparison of the column densities calculated from Haser and Kaneda models and obtained by Hisaki observations is shown in Fig. 1.A8. When v_p and v_d are assumed 0.3 km/s, Haser model can reproduce the bend observed at the altitude of 5×10^4 km by Hisaki (the red line in Fig. 1.A8b). However, these velocities are too slow to be realistic. Additionally, the bend appeared in Haser model is not seen in the results of the numerical simulations such as Fig. 4.2 in this dissertation and Tenishev et al. (2008). The bend appeared in Haser model attributes to the assumption that all particles are moving outward. The outward motion of the parent molecules (H_2O and OH) decreases hydrogen sources in the vicinity of the nuclei,

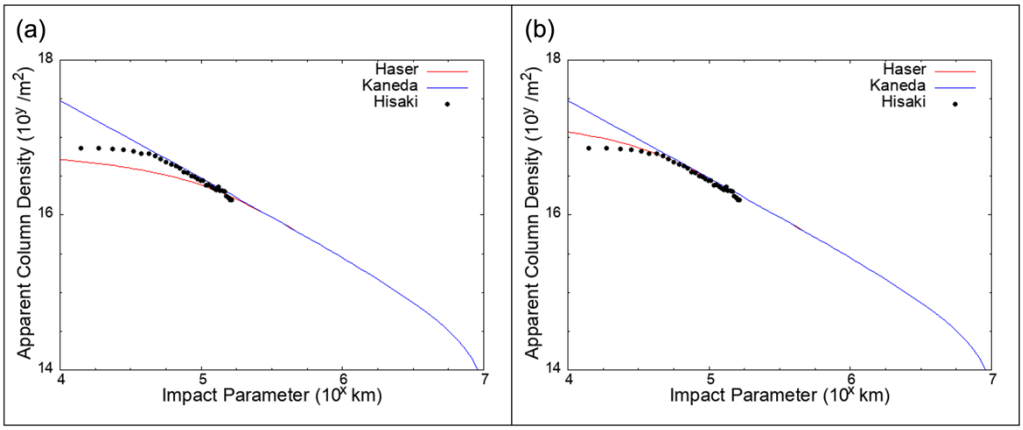

Fig. 1.A8. Comparison of the column densities calculated from Haser and Kaneda models and obtained by Hisaki observations.

The red lines in (a) and (b) are calculated by Haser model with $v_p = v_d =$ 0.85 km/s and $=$ 0.3 km/s, respectively. The blue lines and black dots are deduced from Kaneda model and Hisaki observations.

resulting in the flatter slope of hydrogen density at altitudes below the scale length of the parent molecule.

3.A1. Influence of Swings-Greenstein Effect on G-factor

Swings effect is a change of g-factor due to the relative velocity between the Sun and comets (Swings, 1941). Due to the Doppler shift, hydrogen's received solar flux varies, resulting in the change of g-factor. Greenstein effect is a change of g-factor due to the relative velocity between each atom and comets and the Sun (Greenstein, 1958). Fig. 3.A1 shows an example of the relation between solar spectra and velocity distribution of hydrogen atoms in comet comae, when bulk velocity relative to the Sun and hydrogen temperature are set to be -30 km/s and 5×10^3 K. Velocity of hydrogen atoms is converted to corresponding wavelength of Ly-α emission line shifted by Doppler effect. If radial velocity against the Sun is 0 km/s, hydrogen's received solar photon is 6×10^{12} /cm^2/s/nm. On the other hand, when radial velocity is 30 km/s, received solar photon reaches as large as 7×10^{12} /cm^2/s/nm. Solar spectra is the same as Fig. 3.5 (from Kowalaska-Leszczynska et al., 2020).

Fig. 3.A2 shows dependence of g-factor on radial velocity of hydrogen atoms relative to the Sun and hydrogen temperature. It can be seen that radial velocity varies g-factor by 20% at most. On the other hand, hydrogen temperature changes it only by less than 1.5% even when temperature varies from 0 K to 104 K. Therefore, Swings effect was considered and Greenstein effect was ignored in Chapter 3 as noted in Subsection 3.3.1.

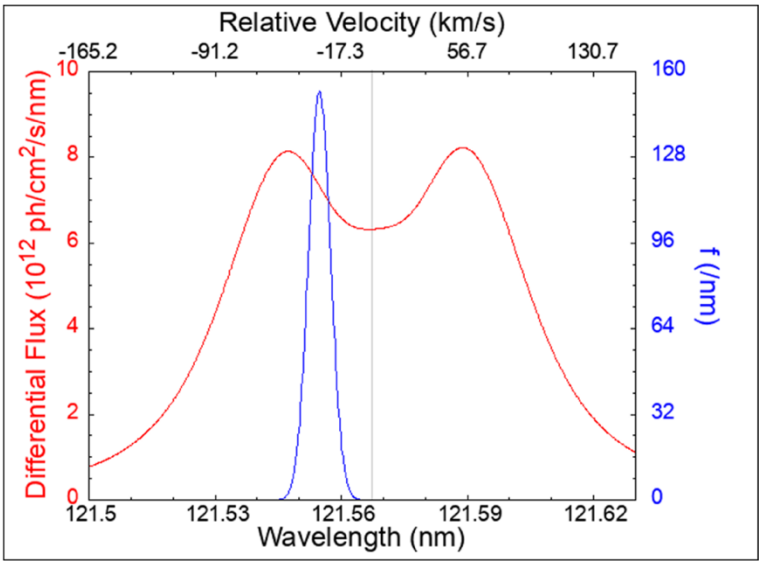

Fig. 3.A1. An example of relationship between solar spectra and velocity distribution of hydrogen in comae.

Velocity of hydrogen atoms is converted to corresponding wavelength of Ly-α emission line shifted by Doppler effect.

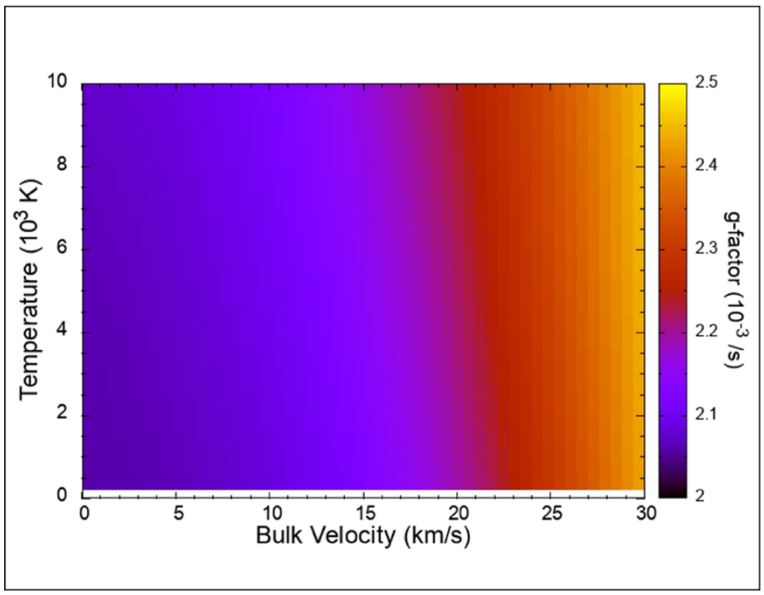

Fig. 3.A2. Dependence of g-factor on radial velocity against the Sun and hydrogen temperature in comae.

4.A1. Dependence of Calculated Lyman Alpha Radiance on Hydrogen Temperature

In Section 4.3, the results when hydrogen temperature was assumed to be 5,000 K and scattering times was considered up to 3 times were shown. In this section, the dependence of the calculated results on hydrogen temperature are shown.

Fig. 4.A1 shows the results of calculated Ly-α radiance distribution with various hydrogen temperatures. As hydrogen temperature increases, optical thickness around the line center decreases, and multiple scattering becomes less effective. When hydrogen temperature is set to be between 5,000K to 7,500K, the calculated Ly-α profile suitably reproduces the observational data of the Hisaki satellite best. This is equivalent to the temperature obtained from observations with high wavelength resolution by Weaver et al. (2008) and calculated temperature at altitudes between 10^4 km to 10^5 km by Tenishev et al. (2008).

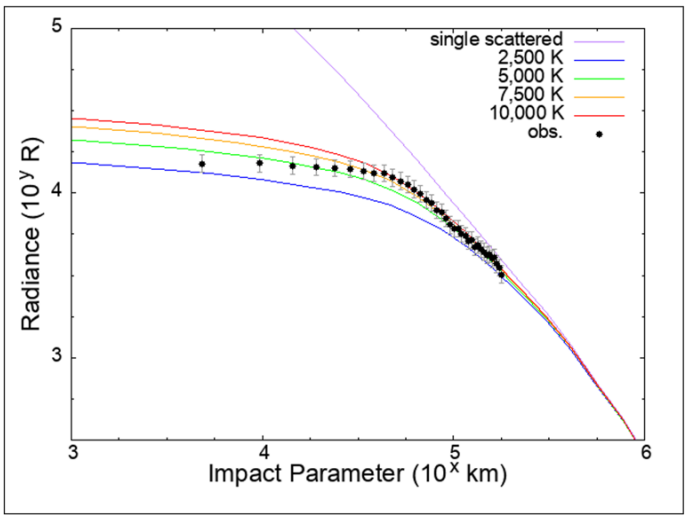

Fig. 4.A1. Dependence of calculated Ly-α profile on hydrogen temperature.

4.A2. Dependence of Calculated Lyman Alpha Radiance on the Considered Number of Scattering

In this section, the dependence of the calculation results in Section 4.3 on the considered number of scattering times is examined.

Fig. 4.A2 shows the results of the calculated Ly-α radiance profile with the various numbers of scattering. As the number of considered scattering times increases, radiance should also rise because the possibility that rays scattered in a direction different from the Sun travels back to the Sun again after several scattering increases. However, the difference in radiance due to the number of scattering times is within 2%, as shown in Fig. 4.A2. Rays that have experienced scattering several times were considered to become darker by the oscillator strength, resulting in minimal increase of radiance with a higher number of viewed scattering times.

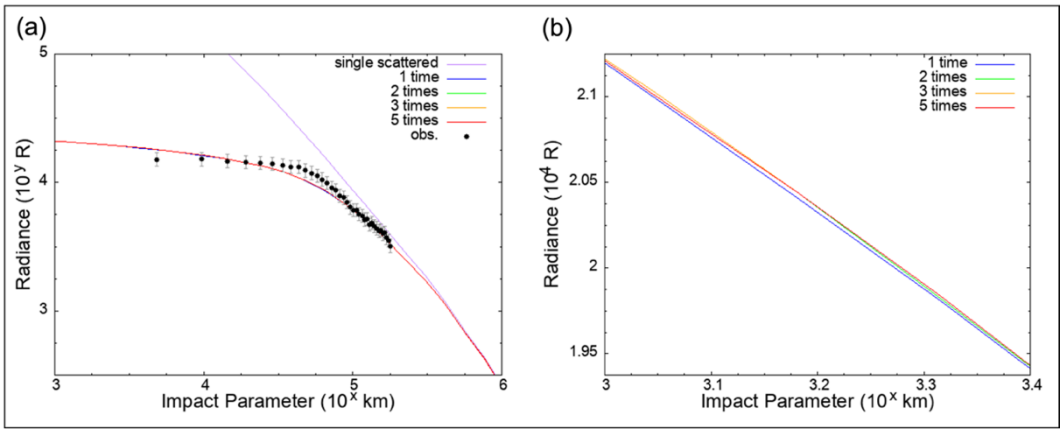

Fig. 4.A2. Dependence of calculated Ly-α radiance profile on the number of considered scattering times.

(a) and (b) are the same graph and the only scales are different. (b) is an enlarged part of (a).

5.A1. Measurement of Hydrogen Temperature in Comae of Comets Using a Hydrogen Absorption Cell

As describe briefly in Subsection 5.1.3, hydrogen temperature in comets' comae can be measured using absorption cells. Fig. 5.A1a shows the variation of absorption rate as a function of the temperature of the filament when observing cometary hydrogen at various temperatures. It can be seen that the slope is steep when the filament temperature is less than 1600 K, while it becomes moderate over the temperature of 1700 K. This corresponds to the saturation of absorption at the filament temperature of 1600 K mentioned in Subsection 5.5.2. The results of calculation of the slope of absorption rate below 1600 K, a_1, and that above 1700 K, a_2 using least square method are shown in Fig. 5.A1b. Although absolute absorption rate cannot be estimated from observational data, hydrogen temperature in the coma can be estimated from the slope of absorption rate when the filament's temperature is changed. For example, if the observational data have relative errors of 10% or 5% and measurement is repeated five times, the errors of estimated hydrogen temperature from the slope below the filament temperature of 1600 K are as shown in Table 5.A1.

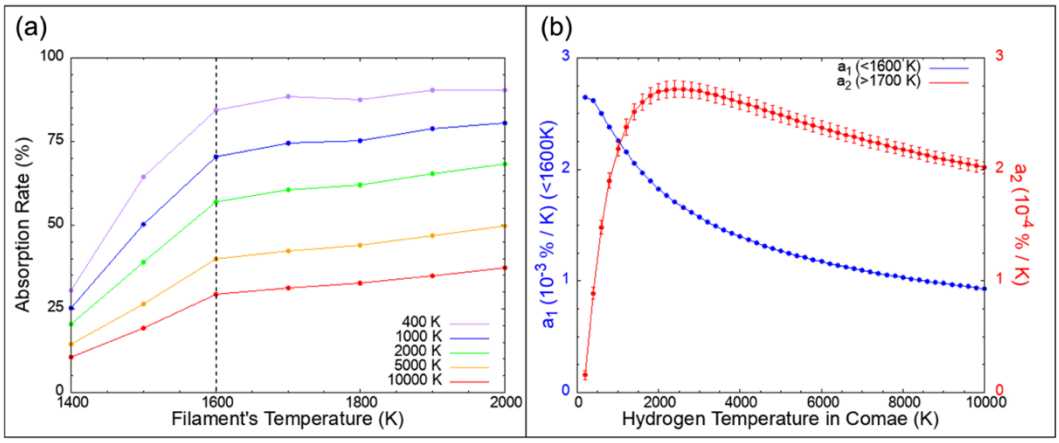

Fig. 5.A1. (a) Dependence of absorption rate on filament's temperature and hydrogen temperature in comae. (b) Dependence of inclination of the graph(a) on hydrogen temperature in comae.

Relative error of the data obtained by HI	Accuracy of the estimation of hydrogen temperature (when measured five times)		
	T_H = 5,000 K	T_H = 7,000 K	T_H = 10,000 K
5%	800 K	1,100 K	1,600 K
10%	1,500 K	2,000 K	2,700 K

Table 5.A1. Accuracy of the estimation of hydrogen temperature in the coma.

T_H denotes true hydrogen temperature in the coma.

6.A1. Time until Absorption Rate of Absorption Cells Reaches Steady State

During the comet fly-by phase, the voltage applied to the filament of the deuterium cell is repeatedly switched on and off for short periods (several seconds). In this section, to determine the allowable frequency of switching, the time necessary for the absorption rate to reach a steady state is evaluated. After the voltage is applied to the filament, absorption rate becomes steady through the following three steps: (1) the filament temperature becomes steady, (2) hydrogen molecules dissociate into hydrogen atoms, and (3) dissociated atoms diffuse into the cell. The velocity of hydrogen atoms in the cell is an order of a few kilometers per second and the size of cell is an order of 10 mm. Therefore, diffusion occurs in milliseconds, and the interior of the cell can be considered sufficiently mixed. In this appendix, the time until the filament's temperature becomes stable, which is regarded as a rate-determining step, is calculated.

Filament's temperature T_f at a certain time t can be calculated from the following equation:

$$mC\frac{dT}{dt} = \frac{V^2}{R(T)} - A\epsilon\sigma T_f^4 - hA\left(T_f - T_0\right)$$

where $m, C,$ and A are mass, heat capacity, and surface area of the filament, respectively. The filament used in this case has a density of 19.3 g/cm^3, a length of 35.6 mm, and a diameter of 24.4 μm. The first term on the right side represents the energy supplied by power consumption. V is voltage applied to the filament, and R is resistance of the filament. The second term represents energy loss due to blackbody radiation, where ϵ and σ are emissivity (set to 0.3) and the Stefan Boltzmann constant. The third term represents Newton's empirical law of cooling. Newton's constant (set to 0.05) and initial temperature (set to 300 K) are represented by h and

T_0, respectively. Calculated temperature is shown in Fig. 6.A1a as a function of elapsed time after voltage is applied. The filament temperature reaches a steady state within 0.3 seconds.

Next, the time required for the heated filament to be cooled is evaluated. A filament temperature can be calculated from the following formula, deleting the first term on the right side of the previous equation:

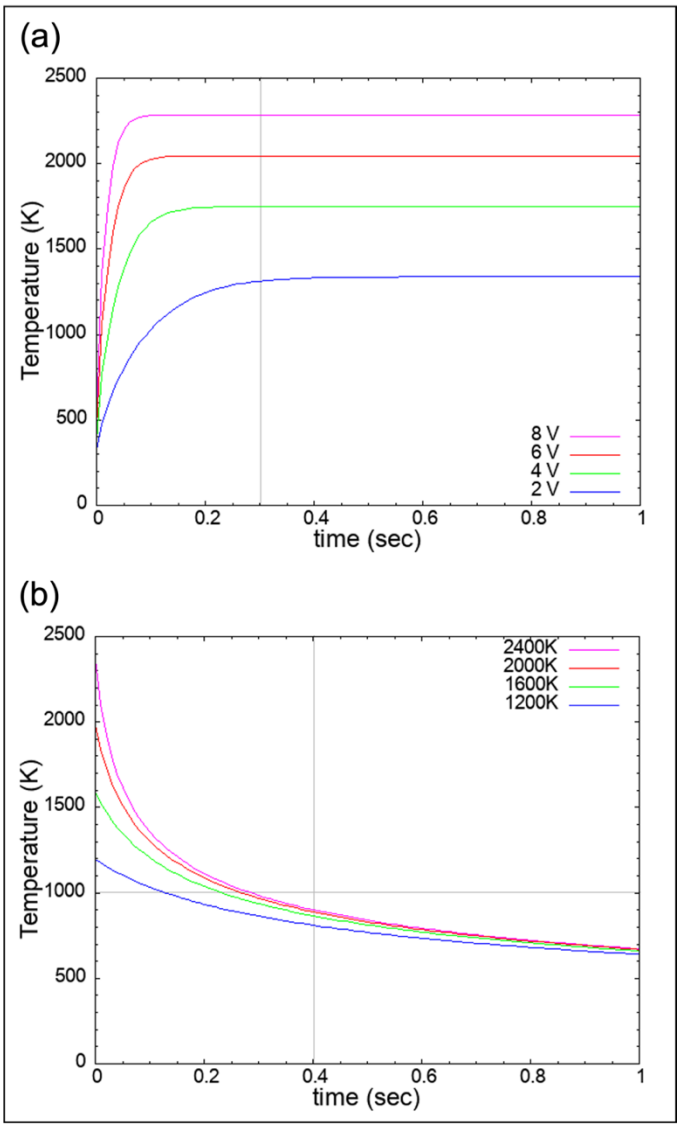

Fig. 6.A1. Time necessary for (a) heating and (b) cooling of the filament in the absorption cell.

$$mC\frac{dT}{dt} = -A\epsilon\sigma T_f^4 - hA\left(T_f - T_0\right)$$

Fig. 6.A1b shows calculated temperature. It takes approximately 3 seconds for the heated filament to cool down to 500 K. However, temperature drops below 1,000 K and absorption becomes negligible 0.4 seconds after the voltage is no longer applied.

Data sampling is planned to be performed every second during comet fly-by phase. However, numerical calculations conducted in this section revealed that it takes 0.3 seconds and 0.4 seconds for heating and cooling, respectively, neither of which are sufficiently shorter than 1 second. Therefore, switching of voltage is preferred to be performed not every second but every 2 seconds. In the future, we will conduct experiments to verify this calculation at experimental facilities such as UVSOR.

References

A'Hearn, M. F., et al., 1995. The Ensemble of Comets: Results from Narrowband Photometry of 85 Comets, 1976–1992. *Icarus*. **118**, 223-270. doi: 10.1006/icar.1995.1190.

A'Hearn, M. F., et al., 2011. EPOXI at Comet Hartley 2. *Science*. **332**, 6036, 1396-1400. doi: 10.1126/science.1204054.

Altwegg, K., et al., 2015. 67P/Churyumov-Gerasimenko, a Jupiter family comet with a high D/H ratio. *Science*. **347**, 6220. doi: 10.1126/science.1261952.

Balsiger, H., et al., 1995. D/H and $^{18}O/^{16}O$ ratio in the hydronium ion and in neutral water from in situ ion measurements in comet Halley. *J. Geophys. Res. Space Phys.* **100**, A4, 5827-5834. doi: 10.1029/94JA02936.

Balsiger, H., et al., 2015. Detection of argon in the coma of comet 67P/Churyumov-Gerasimenko. *Sci. Adv.* **1**, 8. doi: 10.1126/sciadv.1500377.

Barclay, T., et al., 2013. A sub-Mercury-sized exoplanet. *Nature*. **494**, 452-454. doi: 10.1038/nature11914.

Baumgardner, J., et al., 2008. Imaging the sources and full extent of the sodium tail of the planet Mercury. *Geophys. Res. Lett.* **35**, L3201. doi: 10.1029/2007GL032337.

Belton, M. J. S., 2010. Cometary activity, active areas, and a mechanism for collimated outflows on 1P, 9P, 19P, and 81P. *Icarus*. **210**, 881-897. doi: 10.1016/j.icarus.2010.07.007.

Bertaux, J. L., et al., 1978. Lyman-alpha Observations of Venera-9 and 10 I. The Non-thermal Hydrogen Population in the Exosphere of Venus. *Planet. Space Sci.* **26**, 817-831. doi: 10.1016/0032-0633(78)90105-8.

Bertaux, J. L., et al., 1995. SWAN: a study of solar wind anisotropies on SOHO with

Lyman alpha sky mapping. *Solar Phys*. **162**, 403-439. doi: 10.1007/978-94-009-0191-9_11.

Bida, T. A., et al., 2000. Discovery of calcium in Mercury's atmosphere. *Nature*. **404**, 159-161. doi: 10.1038/35004521.

Bieler, A., et al., 2015a. Comparison of 3D kinetic and hydrodynamic models to ROSINA-COPS measurements of the neutral coma of 67P/Churyumov-Gerasimenko. *Astron. Astrophys*. **583**, A7. doi: 10.1051/0004-6361/201526178.

Bieler, A., et al., 2015b. Abundant molecular oxygen in the coma of comet 67P/Churyumov–Gerasimenko. *Nature*. **526**, 678-683. doi: 10.1038/nature15707.

Bishop, J., 1991. Analytic exosphere models for geocoronal applications. *Planet. Space Sci*. **39**, 6, 885-893. doi: 10.1016/0032-0633(91)90093-P.

Biver, N., et al., 2006. Radio wavelength molecular observations of comets C/1999 T1 (McNaught-Hartley), C/2001 A2 (LINEAR), C/2000 WM1 (LINEAR) and 153P/Ikeya-Zhang. *Astron. Astrophys*. **499**, 3, 1255-1270. doi: 10.1051/0004-6361:20053849.

Bockelée-Morvan, D., et al., 1998. Deuterated Water in Comet C/1996 B2 (Hyakutake) and Its Implications for the Origin of Comets. *Icarus*. **133**, 147-162. doi: 10.1006/icar.1998.5916.

Bockelée-Morvan, D., et al., 2004. The Composition of Cometary Volatiles. In: Festou, m. C., et al. (eds.), *Comets II*. Univ. of Arizona Press, Tucson.

Bockelée-Morvan, D., et al., 2012. Herschel measurements of the D/H and 16O/18O ratios in water in the Oort-cloud comet C/2009 P1 (Garradd). *Astron. Astrophys*. **544**, L15. doi: 10.1051/0004-6361/201219744.

Brandt, J. C., Chamberlain, J. W., 1959. Interplanetary Gas. I. Hydrogen Radiation in

the Night Sky. *Astrophys. J.* **130**, 670.

Britt, D. T., et al., 2004. The morphology and surface processes of Comet 19/P Borrelly. *Icarus*. **167**, 1, 45-53. doi: 10.1016/j.icarus.2003.09.004.

Broadfoot A. L., et al., 1974. Mercury's atmosphere from Mariner 10: preliminary result. *Science*. **185**, 166-169. doi: 10.1126/science.185.4146.166.

Burger, M. H., et al., 2010. Monte Carlo modeling of sodium in Mercury's exosphere during the first two MESSENGER flybys. *Icarus*. **209**, 1, 63-74. doi: 10.1016/j.icarus.2010.05.007.

Burger, M. H., et al., 2014. Seasonal variations in Mercury's dayside calcium exosphere. *Icarus*. **238**, 51-58. doi: 10.1016/j.icarus.2014.04.049.

Cassidy, T. A., et al., 2015. Mercury's seasonal sodium exosphere: MESSENGER orbital observations. *Icarus*. **248**, 547-559. doi: 10.1016/j.icarus.2014.10.037.

Cassidy, T. A., et al., 2016. A cold-pole enhancement in Mercury's sodium exosphere. *Geophys. Res. Lett.* **43**, 11,121-11,128. doi: 10.1016/j.icarus.2014.10.037.

Ceccarelli, C., et al., 2014. Deuterium Fractionation: the Ariadne's Thread from the Pre-collapse Phase to Meteorites and Comets today. In: Beuther, H., et al. (eds.), *Protostars and Planets VI*. Univ. of Arizona Press, Tucson. doi: 10.48550/arXiv.1403.7143.

Chamberlain, J. W., 1963. Planetary coronae and atmospheric evaporation. *Planet. Space Sci*. **11**, 911-960. doi: 10.1016/0032-0633(63)90122-3.

Chyba, C. F., 1987. The Cometary Contribution to the Oceans of Primitive Earth. *Nature*. **330**, 632-635. doi: 10.1038/330632a0.

Cipriani, F., et al., 2009. Exospheric signatures of alkali abundances in Europa's regolith. *Geophys. Res. Lett.* **36**, 12. doi: 10.1029/2009GL038636.

Cochran, A. L., et al., 2015. The Composition of Comets. *Space Sci. Rev.* **197**, 9-46. doi: 10.1007/s11214-015-0183-6.

Colaprete, A., et al., 2016. How surface composition and meteoroid impacts mediate sodium and potassium in the lunar exosphere. *Science*. **351**, 6270, 249-252. doi: 10.1126/science.aad2380.

Combi, M. R., 1996. Time-Dependent Gas Kinetics in Tenuous Planetary Atmospheres: The Cometary Coma. *Icarus*. **123**, 207-226. doi: 10.1006/icar.1996.0150.

Combi, M. R., et al., 2004. Gas dynamics and kinetics in the cometary coma: theory and observations. In: Festou, M. C., et al., (eds.), *Comets II*. University of Arizona Press, Tucson.

Combi, M. R., et al., 2018. Water production activity of nine long-period comets from SOHO/SWAN observations of hydrogen Lyman-alpha: 2013–2016. *Icarus*. **300**, 33-46. doi: 10.1016/j.icarus.2017.08.035.

Combi, M. R., et al., 2019. A survey of water production in 61 comets from SOHO/SWAN observations of hydrogen Lyman-alpha: Twenty-one years 1996–2016. *Icarus*. **317**, 610-620. doi: 10.1016/j.icarus.2018.08.031.

Combi, M. R., et al., 2020. The surface distributions of the production of the major volatile species, T H2O, CO2, CO and O2, from the nucleus of comet 67P/Churyumov-Gerasimenko throughout the Rosetta Mission as measured by the ROSINA double focusing mass spectrometer. *Icarus*. **335**, 113421. doi: 10.1016/j.icarus.2019.113421.

Combi, M. R., et al., 2021. Water production rates from SOHO/SWAN observations of six comets: 2017–2020. *Icarus*. **365**, 114509. doi: 10.1016/j.icarus.2021.114509.

Cowan, J. J., A'Hearn, M, F. 1979. Vaporization of Comet Nuclei: Light Curves and Life Times. *Moon Planet*. **21**, 155-171. doi: 10.1007/BF00897085.

Cremonese, G., et al., 1997. Neutral Sodium from Comet Hale-Bopp: a Third Type of Tail. *Astrophys. J.* **490**, L199-L202. doi: 10.1086/311040.

Curdt, et al., 2001. The SUMER Spectral Atlas of Solar-Disk Features. *Astron. Astrophys.* **375**, 591-613. doi: 10.1051/0004-6361:20010364.

Davidsson, B. J. R., 2008. Comet Knudsen Layers. *Space Sci. Rev.* **138**, 207-223. doi: 10.1007/s11214-008-9305-8.

Davis, J. K., et al., 1997. The Detection of Water Ice in Comet Hale-Bopp. *Icarus*. **127**, 238-245. doi: 10.1006/icar.1996.5673.

Eberhardt et al., 1995. The D/H and 18O/16O ratios in water from comet P/Halley. *Astron. Astrophys.* **302**, 301-316.

Eddington, A. S., et al., 1910. The Envelopes of Comet Morehouse (1908 c). *Mon. Not. R. Astron. Soc.* **70**, 5, 442–458. doi: 10.1093/mnras/70.5.442.

Eichhorn, G., 1978. Heating and vaporization during hypervelocity particle impact. *Planet. Space Sci.* **26**, 463-467. doi: 10.1016/0032-0633(78)90067-3.

Feldman, P. D., et al., 2015. Measurements of the near-nucleus coma of comet 67P/Churyumov-Gerasimenko with the Alice far-ultraviolet spectrograph on Rosetta. *Astron. Astrophys.* **573**, A8. doi: 10.1051/0004-6361/201525925.

Festou, M. C., 1981. The Density Distribution of Neutral Compounds in Cometary Atmospheres. *Astron. Astrophys.* **95**, 69-79.

Fougere, N., et al. (2016). Three-dimensional direct simulation Monte-Carlo modeling of the coma of comet 67P/Churyumov-Gerasimenko observed by the VIRTIS and ROSINA instruments on board Rosetta. *Astron. Astrophys.* **588**, A134. doi:

10.1051/0004-6361/201527889.

Fulle, M., et al., 2007. Discovery of the atomic iron tail of comet McNaught using the heliospheric imager on STEREO. *Astrophys. J.* **661**, 1, L94-96. doi: 10.1086/518719.

Gamborino, D., et al., 2019. Mercury's subsolar sodium exosphere: an ab initio calculation to interpret MASCS/UVVS observations from MESSENGER. *Ann. Geophys.* **37**, 455-470. doi: 10.5194/angeo-37-455-2019.

Gasc, S., et al., 2017. Change of outgassing pattern of 67P/Churyumov–Gerasimenko during the March 2016 equinox as seen by ROSINA. *Mon. Not. R. Astron. Soc.* **469**, S108-S117. doi: 10.1093/mnras/stx1412.

Goldstein, B. E., et al., 1981. Mercury: magnetospheric processes and the atmospheric supply and loss rates. *J. Geophys. Res.* **86**, 5485-5499. doi: 10.1029/JA086iA07p05485.

Gulkis, S., et al., 2015. Subsurface properties and early activity of comet 67P/Churyumov-Gerasimenko. *Science*. 347, 6220. doi: 10.1126/science.aaa0709.

Guzik, P., et al., 2020. Initial characterization of interstellar comet 2I/Borisov. *Nat. Astron.* **4**, 53–57. doi: 10.1038/s41550-019-0931-8.

Hadraoui, K., et al., 2019. Distributed glycine in comet 67P/Churyumov-Gerasimenko. *Astron. & Astrophys.* **630**, A32. doi: 10.1051/0004-6361/201935018.

Hansen, K. C., et al., 2016. Evolution of water production of 67P/Churyumov–Gerasimenko: an empirical model and a multi-instrument study. *Mon. Not. R. Astron. Soc.* **462**, S491-S506. doi: 10.1093/mnras/stw2413.

Harada, Y., et al., 2022. BepiColombo Mio Observations of Low-Energy Ions During the First Mercury Flyby: Initial Results. *Geophys. Res. Lett.* **49**, 17. doi:

10.1029/2022GL100279.

Hartogh, P., et al., 2011. Ocean-like water in the Jupiter-family comet 103P/Hartley 2. *Nature*. **478**, 218-220. doi: 10.1038/nature10519.

Haser, L., 1957. Distribution d'intensité dans la tête d'une comète. *Bulletin de la Class des Sciences*. **43**, 740-750.

Hässig, M., et al., 2015. Time variability and heterogeneity in the coma of 67P/Churyumov-Gerasimenko. *Science*. **347**, 6220. doi: 10.1126/science.aaa0276.

Hässig, M., et al., 2017. Isotopic composition of CO2 in the coma of 67P/Churyumov-Gerasimenko measured with ROSINA/DFMS. *Astron. Astrophys*. 605, A50. doi: 10.1051/0004-6361/201630140.

Hiesinger, H., et al., 2020. Studying the Composition and Mineralogy of the Hermean Surface with the Mercury Radiometer and Thermal Infrared Spectrometer (MERTIS) for the BepiColombo Mission: An Update. *Space Sci. Rev.* **216**, 110. doi: 10.1007/s11214-020-00732-4.

Hoang, M., et al., 2017. The heterogeneous coma of comet 67P/Churyumov-Gerasimenko as seen by ROSINA: H_2O, CO_2, and CO from September 2014 to February 2016. *Astron. Astrophys*. **600**, A77. doi: 10.1051/0004-6361/201629900.

Huebner, W. F., et al., 1992. Solar photo rates for planetary atmospheres and atmospheric pollutants. *Astrophys. Space Sci*. **195**, 1-294. doi: 10.1007/978-94-017-3023-5_1.

Hunten, D. M., et al., 1988. The Mercury atmosphere. In: Vilas, F., et al. (eds.), *Mercury*. Univ. of Arizona Press, Tucson. 562–612.

Hunten, D. M., Sprague, A.L., 1997. Origin and character of the lunar an Mercurian atmospheres. *Adv. Space Res*. **19**, 1551-1560. doi: 10.1016/S0273-1177(97)00368-

2.

Hunten, D. M., Sprague, A.L., 2002. Diurnal variation of sodium and potassium at Mercury. *Meteo. Planet. Sci.* **37**, 1191–1195. doi.org: 10.1111/j.1945-5100.2002.tb00888.x.

Hutsemekers, D., et al., 2008. The 16OH/18OH and OD/OH isotope ratios in comet C/2002 T7 (LINEAR). *Astron. & Astrophys.* **490**, 3, L31-34. doi: 10.1051/0004-6361:200810833.

Johansson, F. L., et al., 2017. Rosetta photoelectron emission and solar ultraviolet flux at comet 67P. *Mon. Not. R. Astron. Soc.* **469**, S626-S635. doi: 10.1093/mnras/stx2369.

Johnson, R. E., et al., 2002. Energy Distributions for Desorption of Sodium and Potassium from Ice: The Na/K Ratio at Europa. *Icarus*. **156**, 136-142. doi:10.1006/icar.2001.6763.

Jones, G. H., et al., 2000. Identification of comet Hyakutake's extremely long ion tail from magnetic field signatures. *Nature*. **404**, 574-576. doi: 10.1038/35007011.

Jorda, L., et al., 2016. The global shape, density and rotation of Comet 67P/Churyumov-Gerasimenko from preperihelion Rosetta/OSIRIS observations. *Icarus*. **277**, 257-278. doi: 10.1016/j.icarus.2016.05.002.

Kadono, T., et al., 2007. The Thickness and Formation Age of the Surface Layer on Comet 9P/Tempel 1. *Astrophys. J.* **661**, L89-L92. doi: 10.1086/518418.

Kaneda, E., et al., 1986. Observation of comet Halley by the ultraviolet imager of Suisei. *Nature*. **321**, 297-299. doi: 10.1038/321297a0.

Keller, H. U., et al., 1986. First Halley Multicolour Camera imaging results from Giotto. *Nature*. **321**, 320-326. doi: 10.1038/321320a0.

Killen, R. M., et al., 2004. Source rates and ion recycling rates for Na and K in Mercury's atmosphere. *Icarus*. **171**, 1–19. doi: 10.1016/j.icarus.2004.04.007.

Killen, R. M., et al., 2009. Expected emission from Mercury's exospheric species, and their ultraviolet–visibile signitures. *Astrophys. J. Suppl*. **182**, 667. doi: 10.1088/0067-0049/182/2/667.

Killen, R. M., Hahn, J. M., 2015. Impact vaporization as a possible source of Mercury's calcium exosphere. *Icarus*. **250**, 230-237. doi: 10.1016/j.icarus.2014.11.035.

Kimura, T., et al., 2019. Development of ground pipeline system for high-level scientific data products of the Hisaki satellite mission and its application to planetary space weather. *J. Space Weather Space Clim*. **9**, A8. doi: 10.1051/swsc/2019005.

Kowalaska-Leszczynska, I. et al., 2018. Evolution of the Solar Lyα Line Profile during the Solar Cycle. *Astrophys. J. Suppl*. **852**, 115. doi: 10.3847/1538-4357/aa9f2a.

Kowalaska-Leszczynska, I. et al., 2020. Update of the Solar Lyα Profile Line Model. *Astrophys. J. Suppl*. **247**, 62. doi: 10.3847/1538-4365/ab7b77.

Kuwabara, M., et al., 2018a. Evaluation of the Hydrogen Absorption Cell Imager for Planetary Explorations. UVSOR activity report.

Kuwabara, M., et al., 2018b. Evaluation of hydrogen absorption cells for observations of the planetary coronas. *Rev Sci. Inst*. **89**, 023111. doi: 10.1063/1.5007812.

Leblanc, F., Johnson, R.E., 2003. Mercury's sodium exosphere. *Icarus*. **164**, 261- 281. doi: 10.1016/S0019-1035(03)00147-7.

Leblanc, F., Johnson, R. E., 2010. Mercury exosphere I. Global circulation model of

its sodium component. *Icarus*. **209**, 280-300. doi: 10.1016/j.icarus.2010.04.020.

Lellouch, E., et al., 2022. Size and albedo of the largest detected Oort-cloud object: Comet C/2014 UN271 (Bernardinelli-Bernstein). *Astron. & Astrophys*. **659**, L1. doi: 10.1051/0004-6361/202243090.

Lide, D. R., 1994. CRC Handbook of Chemistry and Physics, 75th ed. Chemical Rubber Company.

Lis, D. C., et al., 2013. A Herschel Study of D/H in Water in the Jupiter-family Comet 45P/Honda–Mrkos–Pajdušáková and Prospects for D/H Measurements with CCAT. *Astrophys. J. Lett*. **774**, L3. doi: 10.1088/2041-8205/774/1/L3.

Lis, D. C., et al., 2019. Terrestrial deuterium-to-hydrogen ratio in water in hyperactive comets. *Astron. Astrophys*. **625**, L5. doi: 10.1051/0004-6361/201935554.

Luspay-Kuti, A., et al., 2015. Composition-dependent outgassing of comet 67P/Churyumov-Gerasimenko from ROSINA/DFMS Implications for nucleus heterogeneity? *Astron. Astrophys*. **583**, A4. doi: 10.1051/0004-6361/201526205.

Mangano, V., et al., 2015. THEMIS Na exosphere observations of Mercury and their correlation with in-situ magnetic field measurements by MESSENGER. *Planet. Space Sci*. **115**, 102-109. doi: 10.1016/j.pss.2015.04.001.

Marschall, R., et al., 2020. Cometary Comae-Surface Links The Physics of Gas and Dust from the Surface to a Spacecraft, Space Sci. Rev. **216**, 130. doi: 10.1007/s11214-020-00744-0.

Massetti, S., et al., 2017. Short-term observations of double-peaked Na emission from Mercury's exosphere. *Geophys. Res. Lett*. **44**, 2970-2977. doi: 10.1002/2017GL073090.

McBride, N., et al., 1997. The inner dust coma of Comet 26P/Grigg-Skjellerup:

multiple jets and nucleus fragments? *Mon. Not. R. Astron. Soc.* **289**, 535-553. doi: 10.1093/mnras/289.3.535.

McClintock, W. E., Lankton, M. R., 2007. The Mercury Atmospheric and Surface Composition Spectrometer for the MESSENGER mission. *Space Sci. Rev.* **131**, 481-521. doi: 10.1007/s11214-007-9264-5.

McClintock, W. E., et al., 2009. MESSENGER Observations of Mercury's Exosphere: Detection of Magnesium and Distribution of Constituents. *Science*. **324**, 610. doi: 10.1126/science.1172525.

Meech, K., et al., 2017. A brief visit from a red and extremely elongated interstellar asteroid. *Nature*. **552**, 378–381. doi: 10.1038/nature25020.

Meier, R., et al., 1998. A Determination of the HDO/H2O Ratio in Comet C/1995 O1 (Hale-Bopp). *Science*. **279**, 5352, 842-844. doi: 10.1126/science.279.5352.842.

Merkel, A. W., et al., 2017. Seasonal variations of Mercury's magnesium dayside exosphere from MESSENGER observations. *Icarus*. **281**, 46-54. doi: 10.1016/j.icarus.2016.08.032.

Merkel, A. W., et al., 2018. Evidence connecting Mercury's magnesium exosphere to its magnesium-rich surface terrane. *Geophys. Res. Lett.* **45**, 6790–6797. doi: 10.1029/2018GL078407.

Milillo, A., et al., 2020. Investigating Mercury's Environment with the Two-Spacecraft BepiColombo Mission. *Space Sci. Rev.* **216**, 93. doi: 10.1007/s11214-020-00712-8.

Morrissey, L., et al., 2022. Solar Wind Ion Sputtering of Sodium from Silicates Using Molecular Dynamics Calculations of Surface Binding Energies. *Astrophys. J. Lett.* **925**, L6. doi: 10.3847/2041-8213/ac42d8.

Mura, A., et al., 2009. The sodium exosphere of Mercury: Comparison between observations during Mercury's transit and model results. *Icarus*. **200**, 1, 1-11. doi: 10.1016/j.icarus.2008.11.014.

Murakami, G., et al., 2016. Ultraviolet detector with CMOS-coupled microchannel plates for future space missions. *Proc. SPIE*. **9905**, 99053G. doi: 10.1117/12.2232183.

Murakami, G., et al., 2020. Mio—First Comprehensive Exploration of Mercury's Space Environment: Mission Overview. *Space Sci. Rev.* **216**, 113. doi: 10.1007/s11214-020-00733-3.

Ness, N. F., et al., 1974. Magnetic field observations near Venus: preliminary results from Mariner 10. *Science*. **183**, 1301-1306. doi: 10.1126/science.183.4131.1301.

Nittler, L. R., et al., 2020. Global major-element maps of Mercury from four years of MESSENGER X-Ray Spectrometer observations. *Icarus*. **345**, 15. doi: 10.1016/j.icarus.2020.113716.

Noonan, J. W., et al., 2018. Ultraviolet Observations of Coronal Mass Ejection Impact on Comet 67P/Churyumov– Gerasimenko by Rosetta Alice. *Astron. J.* **156**, 16. doi: 10.3847/1538-3881/aac432.

O'Dell, C. R., et al., 1988. C_2 in Comet Halley-Evidence for its being third generation and resolution of the vibrational population discrepancy. *Astrophys. J.* **334**, 476-488.

Oliveira, N., et al., 2011. High-resolution broad-bandwidth Fourier-transform absorption spectroscopy in the VUV range down to 40 nm. *Nat. Photo.* **5**, 149-153. doi: 10.1038/nphoton.2010.314.

Ootsubo, T., et al., 2012. Akari Near-infrared Spectroscopic Survey for CO_2 in 18

Comets. *Astrophys. J.* **752**, 15. doi: 10.1088/0004-637X/752/1/15.

Orsini, S., et al., 2021. SERENA: Particle Instrument Suite for Determining the Sun-Mercury Interaction from BepiColombo. *Space Sci. Rev.* **217**, 11. doi: 10.1007/s11214-020-00787-3.

Paradowski, M. L. 2020. A new method of determining brightness and size of cometary nuclei. *Mon. Not. R. Astron. Soc.* **492**, 4175-4188. doi: 10.1093/mnras/stz3597.

Patashnick, H., et al., 1974. Energy source for comet outbursts. *Nature*. **250**, 313-314. doi: 10.1038/250313a0.

Peplowski, P. N., et al., 2014. Enhanced sodium abundance in Mercury's north polar region revealed by the MESSENGER Gamma-Ray Spectrometer. *Icarus*. **228**, 86-95. doi: 10.1016/j.icarus.2013.09.007.

Potter, A. E., Morgan, T. H., 1985. Discovery of sodium in the atmosphere of Mercury. *Science*. **299**, 651-653. doi: 10.1126/science.229.4714.651.

Potter, A. E., Morgan, T. H., 1986. Potassium in the atmosphere of Mercury. *Icarus*. **67**, 336-340. doi: 10.1016/0019-1035(86)90113-2.

Potter, A. E., et al., 1999. Rapid changes in the sodium exosphere of Mercury. *Planet. Space Sci.* **47**, 1441-1448. doi: 10.1016/S0032-0633(99)00070-7.

Powell, K. G., et al., 1999. A Solution-Adaptive Upwind Scheme for Ideal Magnetohydrodynamics. *J. Comp. Phys.* **154**, 2, 284-309. doi: 10.1006/jcph.1999.6299.

Quémerais. E., et al., 2020. PHEBUS on Bepi-Colombo: Post-launch Update and Instrument Performance. *Space Sci. Rev.* **216**, 67. doi: 10.1007/s11214-020-00695-6.

Redwing, E., et al. 2022. NaCl and KCl in Io's Atmosphere. *Planet. Sci. J.* **3**, 238. doi: 10.3847/PSJ/ac9784.

Richter, K., et al., 2000. Multiple Scattering of Hydrogen Lyα Radiation in the Coma of Comet Hyakutake (C/1996 B2). *Astrophys. J.* **531**, 599-611. doi: 10.1086/308433.

Rosborough, S. A., et al., 2019. High-Resolution Potassium Observations of the Lunar Exosphere. *Geophys. Res. Lett.* **46**, 6964-6971. doi: 10.1029/2019GL083022.

Rubin, M., et al., 2015. Molecular nitrogen in comet 67P/Churyumov-Gerasimenko indicates a low formation temperature. *Science*. **348**, 6231. doi: 10.1126/science.aaa6100.

Rubin, M., et al., 2020. On the Origin and Evolution of the Material in 67P/Churyumov-Gerasimenko. *Space Sci Rev.* **216**, 102. doi: 10.1007/s11214-020-00718-2.

Russo, N. D., et al., 2016. Emerging trends and a comet taxonomy based on the volatile chemistry measured in thirty comets with high-resolution infrared spectroscopy between 1997 and 2013. *Icarus*. **278**, 301-332. doi: 10.1016/j.icarus.2016.05.039.

Saki, M., et al., 2021. Chemical Composition of Outbursting Comet C/2015 ER61 (PanSTARRS). *Astron. J.* **162**, 145. doi: 10.3847/1538-3881/abfcbd.

Sandford, S. A., et al., 2021. The Stardust sample return mission. In: *Sample Return Missions The Last Frontier of Solar System Exploration*. Longobardo, A. (eds.), doi: 10.1016/B978-0-12-818330-4.00004-5.

Sarantos, M., Tsavachidis, S., 2020. The Boundary of Alkali Surface Boundary Exospheres of Mercury and the Moon. *Geophys. Res. Lett.* **47**, e2020GL088930.

doi: 10.1029/2020GL088930.

Saur, J., et al. (2015). The search for a subsurface ocean in Ganymede with Hubble Space Telescope observations of its auroral ovals. *J. Geophys. Res. Space Phys.* **120**, 1715–1737. doi:10.1002/2014JA020778.

Scleicher, H., et al., 2004. Detection of neutral sodium above Mercury during the transit on 2003 May 7. *Astron. Astrophys.* **425**, 1119-1124. doi: 10.1051/0004-6361:20040477.

Schroeder I, I. R. H. G., et al., 2018. $^{16}O/^{18}O$ ratio in water in the coma of comet 67P/Churyumov-Gerasimenko measured with the Rosetta/ROSINA double-focusing mass spectrometer. *Astron. Astrophys.* doi: 10.1051/0004-6361/201833806.

Sekanina, Z., 2017. Major Outburst and Splitting of Ling-period Comet C/2015 ER_{61} (PAN-STARRS). arXiv. 1712.03197.

Shemansky D. E., Broadfoot A. L., 1977. Interaction of the surfaces of the Moon and Mercury with their exospheric atmospheres. *Rev. Geophys. Space Phys.* **15**, 491-499. doi: 10.1029/RG015i004p00491.

Shinnaka, Y., et al., 2020. High-resolution Optical Spectroscopic Observations of Comet 21P/Giacobini–Zinner in Its 2018 Apparition. *Astron. J.* **159**, 203. doi: 10.3847/1538-3881/ab7d34.

Slavin, J. A., et al., 1986. The Structure of a Cometary Type I Tail: Ground-based And Ice Observations of P/Giacobini-Zinner. *Geophys. Res. Lett.* **13**, 11, 1085-1088. doi: 10.1029/GL013i011p01085.

Smyth, W. H., Marconi, M. L., 1995. Theoretical overview and modeling of the sodium and potassium atmospheres of Mercury. *Astrophys. J.* **441**, 839-864.

Snodgrass, C., Jones, G. H., 2019. The European Space Agency's Comet Interceptor lies in wait. *Nat. Comm.* **10**, 5418. doi: 10.1038/s41467-019-13470-1.

Snodgrass, C., et al., 2022. Past and Future Comet Missions. In: *Comets III*. University of Arizona Press, Tucson.

Sprague, A. L., et al., 1997. Distribution and abundance of sodium in Mercury's atmosphere, 1985-1988. *Icarus*. **129**, 506-527. doi: 10.1006/icar.1997.5784.

Squires, R. E., Beard, D. B., 1961. Physical and Orbital Behavior of Comets. *Astrophys. J.* **133**, 657.

Sunshine, J. M., et al., 2007. The distribution of water ice in the interior of Comet Tempel 1. *Icarus*. **191**, 73-83. doi: 10.1016/j.icarus.2007.04.037.

Suzuki, Y., et al., 2020. Seasonal Variability of Mercury's Sodium Exosphere Deduced From MESSENGER Data and Numerical Simulation. *J. Geophys. Res. Planets*. **125**, e2020JE006472. doi: 10.1029/2020JE006472.

Taguchi, M., et al., 2000. Ultraviolet imaging spectrometer (UVS) experiment on board the NOZOMI spacecraft: Instrumentation and initial results. *Earth Planet. Space*. **52**, 49-60. doi: 10.1186/BF03351613.

Tenishev, V., et al., 2008. A Global Kinetic Model for Cometary Comae: The Evolution of the Coma of the Rosetta Target Comet Churyumov- Gerasimenko throughout the Mission. *Astrophys. J.* **685**, 659-677. doi: 10.1086/590376.

Teolis, B. D., Waite, J. H., 2016. Dione and Rhea seasonal exospheres revealed by Cassini CAPS and INMS. *Icarus*. **272**, 277-289. doi: 10.1016/j.icarus.2016.02.031.

Teolis, B. D., et al., 2017. Plume and surface feature structure and compositional effects on Europa's global exosphere: Preliminary Europa mission predictions. *Icarus*. **284**, 18-29. doi: 10.1016/j.icarus.2016.10.027.

Tsuchiya, F., et al., 2011. Plan for observing magnetospheres of outer planets by using the EUV spectrograph onboard the SPRINT-A/EXCEED mission. *Adv. Geosci.* **25**, 57. doi: 10.1142/9789814355377_0005.

Veverka, J., et al., 2013. Return to Comet Tempel 1: Overview of Stardust-NExT results. *Icarus*. **222**, 424-435. doi: 10.1016/j.icarus.2012.03.034.

Vidal-Madjar, A., Bertaux, J. L., 1972. A Calculated Hydrogen Distribution in the Exosphere. *Planet. Space Sci.* **20**, 8, 1147-1162. doi: 10.1016/0032-0633(72)90004-9.

Villanueva, G. L., et al., 2009. A Sensitive Search for Deuterated Water in Comet 8P/Tuttle. *Astrophys. J.* **690**, L5. doi: 10.1088/0004-637X/690/1/L5.

Washburn, E. W., 1928. Vapor pressure of sulphuric acid and water mixtures. In: *International critical tables*. **V**, 138.

Weaver, H. A., et al., 2008. Atomic Deuterium Emission and the D/H Ratio in Comets. *Asteroids, Comets, Meteors 2008*. **1405**, 8216.

Weider, S. Z., et al., 2015. Evidence for geochemical terranes on Mercury: global mapping of major elements with MESSENGER's X-Ray Spectrometer. Earth *Planet. Sci. Lett.* **416**, 109-120. doi: 10.1016/j.epsl.2015.01.023.

Whipple, F. L., Stefanik, R. P., 1966. On the physics and splitting of cometary nuclei. *Mem. R. Soc. Liege*. **12**, 33-52.

Wiens, R. C., et al., 1997. Sputtering products of sodium sulfate: implications for Io's surface and for sodium-bearing molecules in the Io torus. *Icarus*. **128**, 386-397. doi: 10.1006/icar.1997.5758.

Yakshinskiy, B. V., Madey, T. E., 1999. Photon-stimulated desorption as a substantial source of sodium in the lunar atmosphere. *Nature*. **400**, 642– 644. doi:

10.1038/23204.

Yamamoto, T., 1985. Formation History and Environment of Cometary Nuclei. In: *Ices in the Solar System*. Klinger, J., et al. (eds.), doi: 10.1007/978-94-009-5418-2_14.

Yamazaki, A., et al., 2014. Field-of-View Guiding Camera on the HISAKI (SPRINT-A) Satellite. *Space Sci. Rev.* **184**, 259-274. doi: 10.1007/s11214-014-0106-y.

Yoshikawa, I., et al., 2010. The Mercury sodium atmospheric spectral imager for the MMO spacecraft of Bepi-Colombo. *Planet. Space Sci.* **58**, 224-237. doi: 10.1016/j.pss.2008.07.008.

Yoshikawa, I., et al., 2014. Extreme Ultraviolet Radiation Measurement for Planetary Atmospheres/Magnetospheres from the Earth-Orbiting Spacecraft (Extreme Ultraviolet Spectroscope for Exospheric Dynamics: EXCEED). *Space Sci. Rev.* **184**, 237-258. doi: 10.1007/s11214-014-0077-z.

Yoshioka. K., et al., 2013. The extreme ultraviolet spectroscope for planetary science, EXCEED. *Planet. Space Sci.* **85**, 250-260. doi: 10.1016/j.pss.2013.06.021.

Acknowledgements

I would like to express my sincere thanks to my supervisor, **Dr. Kazuo Yoshioka**. If I wrote all my gratitude to him, it would be as long as this dissertation. I was able to conduct my study for more than five years due to his careful and enthusiastic guidance. I am happy to be involved in interesting missions such as Hisaki, BepiColombo, EQUULEUS, Comet Interceptor, and LAPYUTA.

I would like to express special thanks to co-workers, **Dr. Go Murakami**, **Dr. Ichiro Yoshikawa**, **Dr. Kei Masunaga**, **Dr. Hideyo Kawakita**, **Dr. Yoshiharu Shinnaka**, **Dr. Tomoki Kimura**, **Dr. Fuminori Tsuchiya**, and **Dr. Atsushi Yamazaki**. Dr. Murakami and Dr. Yoshikawa provided me with valuable advices especially on Mercury, and with the opportunity to be involved with BepiColombo. Dr. Masunaga, Dr. Kawakita, and Dr. Shinnaka gave careful guidance especially on my comet research. Dr. Kimura, Dr. Tsuchiya, and Dr. Yamazaki advised me on the treatment of Hisaki data.

I express my deep gratitude to **Dr. Makoto Taguchi** and **Dr. Masaki Kuwabara**. They kindly instructed me mainly on experiments evaluating the performance of the Hydrogen Imager.

I also appreciate the kind help of **Dr. Seiji Sugita**. He has given me a lot of advice on research and life planning since my undergraduate days. He understands me very well and I believe he gave me special advice that no one else could.

I am grateful to **Dr. Takeshi Imamura**, **Dr. Shogo Tachibana**, **Dr. Aki Takigawa**, **Dr. Satoshi Kasahara**, **Dr. Tomokatsu Morota**, **Dr. Shohei Aoki**, and **Dr. Yuichiro Cho** for providing constructive ideas mainly at the weekly seminar.

Discussion with **Dr. Ryu Funase** and **Dr. Shingo Kameda**, mainly on the Comet Interceptor mission, has been enlightening.

I express my sincere thanks to **Mr. Shota Chiba** and **Ms. Kaori Hirata**. They have been also involved in BepiColombo and have supported me both in my research and personal life. Mr. Chiba was an enthusiastic questioner on my studies, and a valuable chatting buddy in our graduate student room. Ms. Hirata has conducted studies closest to mine, and her extracurricular activities are also similar. Exchange of opinions with her was very fruitful for me.

Thanks to my laboratory members, **Mr. Riku Katsuse**, **Mr. Shuhei Yonemoto**, **Mr. Hiroamsa Akadama**, **Ms. Kanae Nomura**, **Mr. Tatsuki Kosugi**, **Mr. Yuto Sasaki**, **Mr. Ashita Yamazaki**, **Mr. Kazushi Goda**, **Ms. Saniya Sanada**, and **Mr. Tatsuki Matsumoto**, as well as all the **research group members**. Especially, Mr. Yonemoto and Ms. Nomura laid the cornerstone of my studies. I had meaningful discussions with Mr. Sasaki about comets.

I thank **Mr. Makoto Nadamoto**, **Mr. Naofumi Takaki**, and **Mr. Tadahiro Kimura**. They are my best friends, who I could talk to about anything without hesitation, and they have been my greatest mental supporters. They also helped me with research tools.

I also thank **Dr. Natsumi Noda**. She has provided opportunities for outreach activities and given me comprehensive advice on my dissertation. She always brightened my way as an upperclassman.

I want to express my greatest appreciation to **my family**. This work could not be accomplished without their sincere support for many years.

Finally, I am grateful for public and private support of so many people, although I am sorry that I could not write everyone's name here.

The original data of MESSENGER/MASCS used in Chapter 2 are archived in

NASA PDS Geosciences Node (https://pds-geosciences.wustl.edu/missions/messenger/mascs.htm).

The Hisaki data sets used in Chapters 3 and 4 are archived in the ISAS/JAXA Dara Archives and Transmission System (DARTS; https://hisaki.darts.isas.jaxa.jp/) . The Hisaki imaging spectral data used in this paper was retrieved from the raw telemetry data by processing in the pipeline system of Kimura et al. (2019).

This work has been supported by Grants-in-Aid for the Japan Society for the Promotion of Science (JSPS) Research Fellowship for Young Scientists, and the Grant Number is 22J15382.